HYDROGEN & DEUTERIUM DETECTION IN ZR-2.5%NB BY LASER INDUCED BREAKDOWN SPECTROSCOPY

HYDROGEN & DEUTERIUM DETECTION IN ZR-2.5%NB BY LASER INDUCED BREAKDOWN SPECTROSCOPY

By MITCHELL D. KURNELL, B.ENG.SOCIETY

A Thesis
Submitted to the School of Graduate Studies
In Partial Fulfilment of the Requirement for the Degree of
Master of Applied Science

McMaster University

MASTER OF APPLIED SCIENCE (2020) MCMASTER UNIVERSITY

(Engineering Physics) Hamilton, Ontario, Canada

TITLE: Hydrogen & Deuterium Detection in Zr-2.5%Nb by Laser Induced Breakdown Spectroscopy

AUTHOR: Mitchell Dennis Kurnell, B.Eng.Society (McMaster University)

SUPERVISORS: Dr. D.R. Novog & Dr. J.S. Preston

NUMBER OF PAGES: 124

Acknowledgements

Firstly, I would like to thank my supervisors, Dr. Novog and Dr. Preston for their guidance and support during this project. This project would not have been successful without their expertise and I am thankful for their belief in me.

Bill Shaw, Shawn Lowe, and all of your colleagues, thank you for your great suggestions and the help throughout this project. Your insights definitely helped with the success of this work.

To Dr. Steven Rehse and your team, thank you for allowing me to visit your labs and for your help running experiments. Your insights and expertise in LIBS was an immense help to me and definitely helped me conduct better research.

I would also like to thank Dr. Novog's and Dr. Preston's research groups. Your support and suggestions were very helpful throughout this journey. In particular, I would like to thank Garik, Chris, Phil, Stephen, and Mike; the conversations we had not only helped my better understand my work, they also opened avenues of exploration to further my knowledge.

I also would like to acknowledge my friends who helped to keep me sane during this time. Thank you for taking my mind off of work for necessary breaks.

Thank you to Samantha for your constant belief in me and for supporting me through this. Your presence calmed me when research was stressful and heightened the excitement of my successes.

Finally, I would not have been able to make it to this point without the unending support of my parents, David and Patricia, and my brother Jason. I am forever thankful for everything you have done and continue to do for me.

List of Acronyms

Ar Argon

CANDU CANada Deuterium Uranium

CCD charge-coupled device

Cd Cadmium

CF-LIBS Calibration Free Laser Induced Breakdown Spectroscopy

CMOS Complementary Metal-Oxide-Semiconductor

CNSC Canadian Nuclear Safety Commission

CWEST Circumferential Wet Scrape Tool

D Deuterium

D-α Deuterium Alpha

DHC Delayed Hydride Cracking

D_2O Heavy Water

DPSSL Diode-Pumped Solid State Laser

DP-LIBS Double Pulsed Laser Induced Breakdown Spectroscopy

ESA European Space Agency

FWHM Full Width at Half Maximum

H Hydrogen

H-α Hydrogen Alpha

He Helium

H_{eff} Effective Hydrogen Concentration

HeNe Helium Neon

HVEMS Hot Vacuum Extraction Mass Spectrometry

ICCD Intensified Charge Coupled Device

ITER International Thermonuclear Experimental Reactor

JET Joint European Torus

LAMIS Laser Ablation Molecular Isotopic Spectroscopy

LIBS Laser Induced Breakdown Spectroscopy

LIPS Laser Induce Plasma Spectroscopy

LOCA Loss of Coolant Accident

LOD Limit of Detection

LSS Laser Spark Spectroscopy

LTE Local Thermodynamic Equilibrium

Nb Niobium

NIST National Institute of Standards and Technology

OMA Optical Multichannel Analyzer

SEM Scanning Electron Microscope

SNR Signal to Noise Ratio

T Tritium

TSS Terminal Solid Solubility

TDMS Thermal Desorption Mass Spectrometry

TDS Thermal Desorption Spectrometry

TEPCO Tokyo Electric Power Company

Zr Zirconium

ZrH Zirconium Hydride

ZrD Zirconium Deuteride

ZrO_2 Zirconium Oxide

Zr-2.5%Nb Zirconium-2.5% Niobium

Contents

List of Tables

List of Figures

Abstract

The detection of trace amounts of H and D present in Zr-2.5%Nb in the form of ZrH and ZrD, respectively, by LIBS was explored. The intended use case for this experimentation was CANada Deuterium Uranium (CANDU) nuclear reactor pressure tube inspections where hydride buildup can lessen the mechanical strength of these components. As these tubes carry coolant and house the fuel bundles, their integrity is paramount. A LIBS inspection method is of interest in the nuclear industry due to the operational flexibility it would introduce and its ability to reduce the cost, time, and radiation dose associated with inspection campaigns of pressure tubes in CANDU nuclear reactors.

Using LIBS, simultaneous detection of H and D was achieved in a low-pressure air environment using a microjoule, picosecond pulsed laser and emission being captured by a high-resolution spectrometer. The emission lines of the two species were blended, however, two peaks can be seen. Experiments using a milijoule, nanosecond pulsed laser in a LIBS setup were also conducted at atmospheric pressures. These experiments failed to show D emission, however.

In addition to detecting emission from H and D, a Monte Carlo algorithm was developed for estimating the error associated with a LIBS inspection of a pressure tube segment. ZrH and ZrD form heterogeneous structures in the bulk of the Zr-2.5%Nb pressure tube material, meaning that a single measurement would not be indicative of the entire tube. Using metallographs of artificially hydrided pressure tube samples, the error within a given confidence interval was found as a function of number of measurement sites and ablation diameter.

Furthermore, the impacts to Zr-2.5%Nb based on intense laser-matter interactions was investigated by optical microscopy and interferometry, allowing for 3-dimensional reconstructions of ablation craters. The morphology of millijoule, nanosecond pulsed laser-matter interaction and microjoule, picosecond pulsed laser-matter interaction were the subjects of this investigation. The salient difference between the two interactions is the evidence of substantial melting and subsequent re-deposition of material in the case of nanosecond interactions, whereas picosecond ablation yielded little melting.

These results support the further development of a LIBS-based inspection method for determining the concentration of H and D in Zr-2.5%Nb. It was found that a vacuum environment allows for the simultaneous detection of H and D emission. Further experimentation should explore using low-pressure buffer gas environments as a method to further distinguish emission between the two species.

1 INTRODUCTION

1.1 Background

The design of nuclear power plants require significant considerations in the materials used for different components. Concern must be taken to ensure the mechanical viability of a material to perform its structural function, radiation interaction properties must be considered such that the material's presence does not influence the necessary reactions, and its interaction with the coolant flow must be examined. Considering these factors, Zr alloys are used in nuclear power plants due to their corrosion resistance in water and low neutron radiation cross section [1, 2]. In CANDU reactors Zr-2.5%Nb is used to make the reactor's pressure tubes. These are the tubes which hold the nuclear fuel bundles and carry coolant through the fuel channels. It is essential to ensure that these safety-critical components remain strong enough to support the weight of the fuel and the high pressure coolant over their lifetime and will not succumb to any mode of failure.

In 1983 one of the pressure tubes in the Pickering A reactor cracked leading to a Loss of Coolant Accident (LOCA) [3]; a very serious event in a nuclear power plant. As the name implies, these accidents are scenarios where a break in the heat transport system results in some of the coolant fluid escaping the loop. Signifi-

cant coolant losses can result in damage to the reactor core, however, the accident at Pickering was halted before significant damage was done [3]. The accident occurred when garter springs, which serve to separate the pressure tubes and the surrounding calandria tubes, moved out of position. Calandria tubes surround the pressure tubes, with a gas gap between the two and the moderator fluid outside of the calandria tubes.[1] The dislocated garter springs allowed the pressure tubes to sag and come into contact with the calandria tubes creating a large temperature gradient due to the temperature difference between the moderator and coolant. This temperature gradient led to favourable diffusion conditions for H. As the sag resulted in a relatively small contact area a localized high concentration of hydrides formed which eventually led to the pressure tube failure.

When the pressure tube was removed, it was found that a crack had propagated approximately 2 m along length of the pressure tube. One of the reasons behind the extensive length of the crack was the presence of zirconium hydrides, ZrH and ZrD [3].[2] A high concentration of hydrides can lead to crack propagation by a process called Delayed Hydride Cracking (DHC) [5]. DHC begins when a microstructural stress concentration creates a region of higher chemical potential for hydrogen, encouraging the precipitation of hydrides. The reduction in ductility of the alloy caused by the presence of the hydrides can then allow the crack tip to

[1] Please refer to Chapter 4, Section 8 of [4] for a description of the calandria/pressure tube relationship and Figure 19 for a graphical representation of the calandria tube and pressure tube.

[2] For simplicity, both of these compounds will be referred to as ZrH or hydrides unless it is necessary to differentiate between the two.

propagate. Coupled with the heating and cooling cycles experienced by pressure tubes during power cycling of reactors, hydride concentrations can further increase, eventually leading to a large crack developing [5, 6].

As a result of these investigations, operating utilities began conducting regular inspections of the hydride content in pressure tubes, which is reported as the Effective Hydrogen Concentration (H_{eff}). It is known that hydrides form in pressure tubes because during operation of the reactor radiolysis of coolant results in free H and D ions, depending on the coolant used, in the solution which can diffuse into the pressure tubes. Since both H and D ions can be present, operating utilities using CANDU reactors must take care when measuring the H_{eff} as CANDU reactors use Heavy Water (D_2O) as their coolant. Therefore, the H_{eff} must include not only the H concentration, but also the D concentration as both elements will react with Zr to form hydride compounds.

To date, most successful inspection tools have been based on the same principle and are collectively referred to as "scrape" methods. The most recent iteration of scrape tools in use in Canada is the Circumferential Wet Scrape Tool (CWEST) developed by Kinectrics. Scrape methods use long tool heads with cutters to cut and retrieve small samples, or scrapes, from the inside of the pressure tubes which are later sent for analysis using either Hot Vacuum Extraction Mass Spectrometry (HVEMS) or Thermal Desorption Mass Spectrometry (TDMS). These samples are small, relative

to the size of the pressure tube, but are large enough to constitute a representative measurement of a significant section of the pressure tube. Additionally, careful consideration is given to the depth and length of the scrapes to ensure that the structural integrity of the pressure tubes will be maintained. Therefore, by taking many scrapes along a single pressure tube, operators can obtain an accurate picture of the average concentration of H and D in the entire pressure tube. Given the importance of the hydride issue, there is strong incentive for continuous improvement in the inspection methods and for faster and more detailed results.

Hot Vacuum Extraction Mass Spectrometry (HVEMS) and Thermal Desorption Mass Spectrometry (TDMS) are similar testing methods used to analyze the samples retrieved by scrape methods. A sample is inserted to a test chamber, the sample is slowly heated to a point where any H or D present in the sample are given sufficient energy to escape the lattice, and the resultant gas is measured using mass spectrometry. Mass spectrometry methods for measuring H_{eff} provide high accuracy measurements with 5% error at 95% confidence [7]. However, the large and complex equipment needed inhibit the ability of such a system to be used in situ. Furthermore, many nuclear operators do not have the necessary mass spectroscopy equipment on site and are required to contract other firms for these measurements. Thus, operating utilities are required to ship samples off site for analysis, resulting in long analysis times, high worker dose, and high costs associated with shipping and handling radioactive material.

To address the above concerns, efforts have been in place to develop in situ testing methods for measuring the H_{eff}. The most prominent effort to date utilized the Terminal Solid Solubility (TSS) of hydrogen isotopes in pressure tubes [8]. TSS measurements work by determining the TSS temperature in a section of the pressure tube. The temperature of the section is determined by using eddy currents to measure the material resistivity between two points [8]. There exists a well-defined relationship between the TSS temperature and the hydrogen concentration, as such knowing this temperature allows for determination of the concentration. However, after performing 20 inspections in CANDU reactors, the tool was pulled from service due to data quality issues [9].

A desire still exists within the nuclear industry to develop an inspection tool which can make H_{eff} measurements faster and at a lower cost. Such a tool would need to match the accuracy and reliability of the currently accepted scrape methods, but ideally make in situ measurements. Such an inspection method would have multiple benefits: 1) information on H_{eff} concentrations would be available immediately, allowing for real-time updating of the inspection scope and operational flexibility, 2) reduced worker dose, 3) more measurements could be conducted during an outage campaign (or alternatively a shorter campaign if the H_{eff} measurement was on the critical path), and 4) a possibility of reducing inspection costs with a potentially lower risk of inspection-induced flaws or pressure tube damage. A tool able to provide these benefits would be of tremendous benefit to nuclear operators.

Outside of nuclear fission reactors, interest in the discrimination of H and D concentrations in materials has also become of interest to members of the fusion community. The operation of fusion reactors creates H, D, and Tritium (T), whose presence in the plasma-facing materials is of concern [10]. To monitor the concentration of these contaminants in the plasma-facing materials, researchers at International Thermonuclear Experimental Reactor (ITER) and Joint European Torus (JET) are investigating LIBS as the technique they will use to remotely monitor H and D concentrations in situ. Further discussion of these applications is provided in Chapter 2: Literature Review.

Using these developments as a base, it seems plausible that LIBS may be developed into a compatible tool for making measurements of the H_{eff} in CANDU reactors.

1.2 Purpose

The purpose of this thesis is to investigate the plausibility of using LIBS as a method for in situ inspection of the effective hydrogen concentration, H_{eff}, in pressure tubes for use in CANDU reactors. The research focused on the ability to distinguish between H and D in artificially hydrided Zr-2.5$\%$Nb samples. An inspection technique such as LIBS would enable H_{eff} measurements to be made in situ and allow for immediate analysis by inspection personnel. Interest in the rapid deployment of an on-site tool for measuring hydrogen content in nuclear materials, even if in an ex situ format initially, has been expressed by operating utilities. As previously

mentioned, the benefits of a LIBS inspection tool include: 1) information on H_{eff} concentrations would be available immediately, allowing for real-time updating of the inspection scope, 2) reduced worker dose, 3) more measurements could be conducted during an outage campaign (or alternatively a shorter campaign if the H_{eff} measurement was on the critical path), and 4) a possibility of reducing inspection costs with a potentially lower risk of inspection-induced flaws or pressure tube damage.

LIBS is a minimally destructive technique when compared with existing scrape methods. While the flaws introduce by scrape methods have been well characterized and determined to introduce an acceptable flaw profile, it would be favourable to reduce the amount of material removed from the pressure tube structure while conducting inspections. Future work would need to be conducted on the flaws introduced by LIBS measurements to ensure they fall within acceptable parameters. An individual scrape has a macroscopic profile, removing approximately 190 mm^3 of material for each scrape. However, an individual LIBS measurement can remove as little material as 60 μm^3 meaning that measurement areas can be more precise. Additionally, a LIBS measurement would either not introduce a heat affected zone or a minimal zone depending on the laser pulse duration used. This alleviates potential concerns around local changes to the microstructure and phase of the material.

Since a LIBS inspection tool would provide real-time measurements, this also in-

creases operational flexibility for inspection workers. As previously stated, current inspection methods require samples to be sent off-site, resulting in several weeks to months of processing in order to receive results and by the time such results are available, the inspection outage would be finished. Any re-inspections or new inspections require significant changes to future outages or, at worst, an unplanned outage. An example scenario may have workers performing inspections and obtain anomalous or unanticipated results. Due to the ease of operation of a LIBS inspection tool and its real-time status, workers may be able to increase or decrease their inspection scope.

In summation, the aim of this thesis is to determine if it is possible to distinguish characteristic signals from H and D. Successful distinction would give credence to the proposal of using LIBS as a fuel channel inspection tool. Additionally, the need for a vacuum environment, and the effect of different backing gases on the LIBS spectrum is considered in this work.

1.3 LIBS Theory

1.3.1 Laser-Matter Interactions

LIBS works by using a short-pulsed laser to deposit a large amount of energy into the electronic system of a material in a very short period of time in a very small area. If the incident fluence, measured in J/cm^2, exceeds the material's threshold ablation

fluence, a small portion of the material will be directly converted into a plasma (i.e. a vapourization transition with little to melting). The ablation threshold can be calculated theoretically based on material properties as seen in Equation 1.1 [11].

$$F_{th}(\lambda) = \frac{H_{vap}}{\alpha(\lambda)\ A(\lambda)} \tag{1.1}$$

Where $F_{th}(\lambda)$ is the ablation threshold at a specific wavelength (J cm^{-2}), H_{vap} is the heat of vaporization of the target material, $\alpha(\lambda)$ is the absorption coefficient of the target material at the wavelength of the incident laser, and $A(\lambda)$ is the absorptance of the target material at the wavelength of the incident laser.

The removed material is super-heated during the process, up to temperatures as high as 40,000 K [12], causing the material to transition to a plasma state. A plasma created by LIBS is composed of the target material and the surrounding atmospheric gases which interact with the liberated material. To create the plasma, a high-powered laser simply needs to be focused onto the target such that the incident fluence exceeds the threshold fluence of the target. Depending on the pulse duration of the laser, the ablation mechanism will be different. Figure 1.1 shows a simplified example of how a typical picosecond LIBS event occurs. The salient difference between picosecond LIBS and nanosecond LIBS can be seen when comparing Figure 1.1 and Figure 1.2 where interaction occurs between the LIBS plasma and the laser in the case of nanosecond LIBS which alters the plasma dynamics.

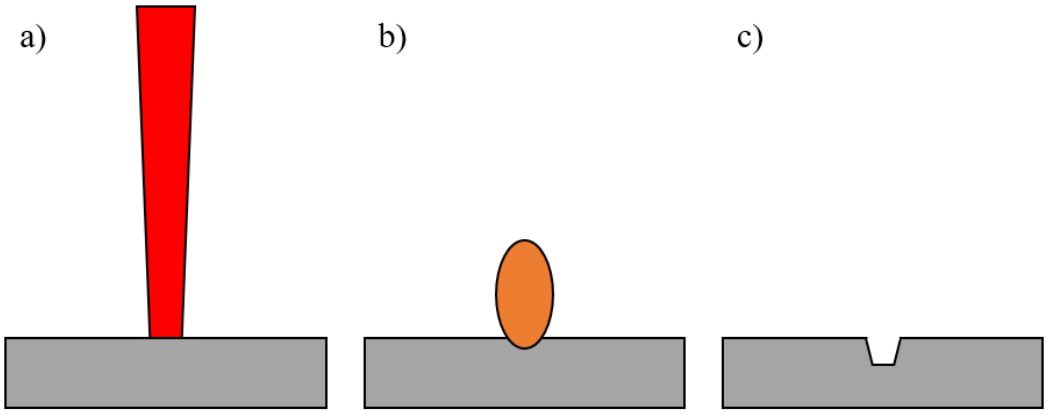

Figure 1.1: In picosecond ablation, the plasma is formed after the laser pulse. a) Laser pulse focused on or slightly below the sample's surface. b) Plasma is formed at the surface of the sample. c) Resultant crater on the sample.

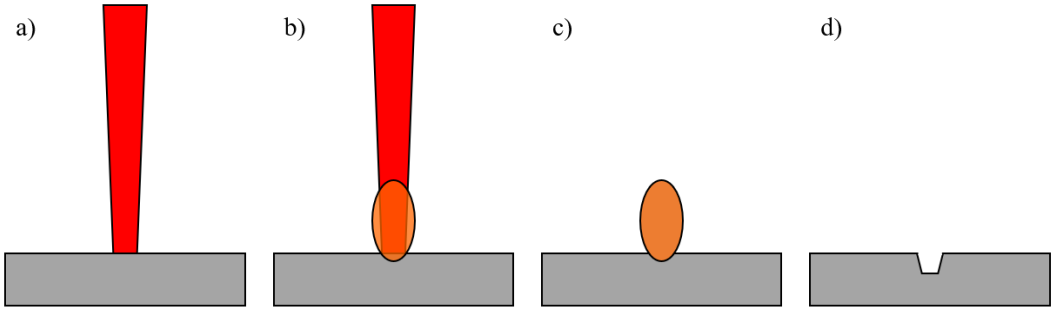

Figure 1.2: In nanosecond ablation, the plasma is formed during the laser pulse. a) Laser pulse focused on or slightly below the sample's surface. b) Plasma is formed at the surface of the sample while the laser pulse is still incident. c) Laser pulse ends and plasma emission continues. d) Resultant crater on the sample.

The plasma is short-lived, however, as the ejected material creates a local high pressure environment, driving material away and cooling the plasma through collisions [13, 14]. The plasma also loses energy through radiation. This loss occurs as the plasma begins to cool and electrons have a low enough energy to become bound to the constituent atoms in the plasma. At this point the plasma still is hot

enough to excite the newly bound electrons to higher states, which eventually relax to either the ground state or a lower energy state, releasing a photon. This photon results in some energy being lost from the plasma and helps to further cool it. Some LIBS applications, such as Double Pulsed Laser Induced Breakdown Spectroscopy (DP-LIBS), will use additional laser pulses to re-excite the plasma and increase the emission intensity. This technique can be used to increase the sensitivity of LIBS measurements [14, 15].

The photon emission from the plasma is the main aspect of interest for spectroscopists, as the emission is dictated by the composition of the material under investigation. The wavelengths contained within the emission profile will only come from either the target material or the surrounding atmosphere. Plasma emission from LIBS plasmas is defined by Equation 1.2 and Equation 1.3 [16].

$$I_{mn} = \frac{h\nu_{mn}}{4\pi} A_{mn} N_m \tag{1.2}$$

$$N_m = \frac{N}{Q(T)} g_m e^{-\epsilon_m / kT} \tag{1.3}$$

Where I_{mn} is the emissivity of a transition, N_m is the density of atoms or ions in the upper level m, A_{mn} is the Einstein transition probability from state m to n, N is the total number density, $Q(T)$ is the atomic partition function, and g_m and ϵ_m are the statistical weight and the energy of the energy level m, respectively.

1.3.2 Spectrometers

The plasma emission created during an ablation event can be captured using optical fibres and directed into a spectrometer to precisely determine the wavelengths of light being emitted. A spectrometer consists of several components: 1) the entrance slit where light is directed into the spectrometer, 2) a collimating lens/mirror, 3) a diffraction grating which splits the light into its constituent components and, 4) the detector array which digitizes the input light.

The entrance slit is the first element of a spectrometer. This component determines how much light enters the spectrometer and plays a part in determining the resolution of the spectrometer. The width of the entrance slit determines the size of the image which will be transmitted throughout the system and when properly aligned the input slit will be imaged onto the detector array. Care should be taken in selecting an entrance slit width to balance the light throughput and the resolution of the system.

After passing through the entrance slit, the light is collimated and directed towards the diffraction grating. This can be accomplished either by using a collimating mirror or a combination of a mirror and a collimating lens.

The diffraction grating takes the incoming light from the collimating system and splits it into its constituent wavelength components. The main aspects of the diffrac-

tion grating are the groove density, and the blaze angle. Firstly, the groove density is a measure of how many ruled lines are inscribed onto the surface of the grating and is measured in grooves/mm. The groove density determines the wavelength range covered by the spectrometer and also plays a role in determining the resolution of the spectrometer. with the range being inversely proportional to the groove density and the resolution being directly proportional to the groove density. The wavelength range is defined by Equation 1.4 and the minimum resolvable wavelength difference is defined by Equation 1.5.

$$\lambda_{max} - \lambda_{min} = L_D \, \frac{10^6 \, d \cos\beta}{m \, F} \tag{1.4}$$

$$\frac{\Delta\lambda}{\lambda} = \frac{1}{m \, N} \tag{1.5}$$

For Equation 1.4, λ_{max} and λ_{max} are the maximum and minimum wavelengths that can be observed, respectively, L_D is the detector length, d is the groove period (the inverse of the groove density), β is the diffraction angle, m is the diffraction order, and F is the focal length of the focusing element. For Equation 1.5, λ is the wavelength of interest, $\Delta\lambda$ is the minimum resolvable difference between wavelengths, m is the diffraction order, and N is the number of grooves.

The other important aspect is the blaze angle of the diffraction grating, measured in nanometers (nm). The groove angle largely determines the efficiency of the grating at various wavelengths. The main consideration in choosing a blaze angle is to

ensure that the diffraction grating has a high efficiency either at the wavelength of interest or at a weakly emitting part of the spectrum. Depending on the application of interest, optimizing for a weakly emitting part of the spectrum of interest can help to highlight features which may be otherwise suppressed. Having some a priori knowledge of the application of interest assists with these design considerations.

Many spectrometers will include multiple diffraction gratings to allow for modularity in their operation. The user is then able to select the best grating to ensure that they maximize light throughput at the required resolution.

After light is reflected off the diffraction grating, it is then focused onto the detector. The detector array can be a charge-coupled device (CCD), Complementary Metal-Oxide-Semiconductor (CMOS), or Intensified Charge Coupled Device (ICCD) camera, each with their own benefits and drawbacks. The important aspects of a camera used in a LIBS application are: 1) gate delay and delay accuracy (i.e. response time to a trigger), 2) gate width and level of control over the gate width and, 3) sensitivity. These factors are important as the camera should only collect light during the gated period. Capturing light too early may result in the laser pulse saturating the sensor or continuum emission dominating the signal. Capturing light too late means that the plasma may have cooled too much and the emission has become weak, resulting in a poor Signal to Noise Ratio (SNR). Additionally, waiting too long in the plasma lifetime may result in the escape of lighter elements from the

plasma.

For high resolution systems, ICCD cameras are often used. These cameras can have small pixels and also allow for very precise gating of the camera. As LIBS measurements require very accurate gate delays and gate widths, being able to turn on and off the camera very precisely is important. Additionally, ICCD cameras can be very quickly shuttered, on the order of a few nanoseconds, since they are electronically shuttered. ICCD cameras use an accelerating voltage to move electrons generated by incident photons to the detector array. By shutting off this accelerating voltage, the camera's collection stops. This is much quicker than cameras that require a mechanical shutter and allows for a much more accurate setting of the gate delay and gate width.

1.3.3 Plasma Emission

The light analyzed by the spectrometer during a LIBS measurement is based on atomic emission. Every atom has characteristic wavelengths they emit which are defined by electronic transitions. As electrons relax from excited states, they have a chance to emit light at the wavelength defined by the energy difference between the excited state and the ground state. Since every atom has a different structure, these transitions are unique to each atom; even the slight differences in structure between atomic isotopes result in slightly different transition energies. The unique transi-

tions arising from the differences in atomic structure allow for the determination of atomic species based on plasma emission. Equation 1.6 indicates the wavelength that will be observed based on atomic energy levels for the hydrogen atom.

$$\frac{1}{\lambda} = R\left(\frac{1}{n_i^2} - \frac{1}{n_j^2}\right) \tag{1.6}$$

Where λ is the wavelength of the released photon, R is the Rydberg constant, and n_i and n_j are the principal quantum numbers of lower and upper energy levels, respectively.

Organizations, such as NIST, have compilations of data concerning the emission wavelengths of atoms gathered by various researchers. Having access to this database allows for comparison of the peak emission wavelengths to known peaks. This allows for identification of the emitting species.

Despite elements having well-defined spectra and compilations of emission wavelengths, characterization of elemental species using LIBS is a non-trivial task. In heavier materials, like Zr, the high number of electrons and energy levels results in complicated spectra with potentially hundreds of emission lines. Also, having multiple stable isotopes results in even more persistent emission lines. Emission lines also sometimes overlap with the emissions of other elements or may blend with other lines if their wavelengths are very close because emission profiles have some associated width.

Unlike heavy heavy elements, light elements, especially H, have very well-defined emission spectra due to the significant spacing of energy levels. Having very few electrons means that the separation between energy levels is quite distinct. However, lighter elements are also more affected by emission line broadening mechanisms [14]. The broadness of spectral lines, of both light and heavy elements, is affected by the measurement environment and plasma interactions [14]. Since the plasma contains ionized atoms and free electrons, electric and magnetic fields arise which cause some line broadening by mechanisms such as the Stark Broadening and the Zeeman effect. These mechanisms broaden emission lines by shifting energy levels of atoms due to the presence of electric fields and magnetic fields, respectively. Additionally, Doppler broadening occurs due to the random motion of the plasma. Certain atoms move away from the collection optics while emitting, resulting in a slightly longer emission wavelength than expect while the opposite case also occurs. Furthermore, while measuring in an atmospheric pressure or higher pressure environment, the effects of collisions between species and the increased density of the plasma will lead to broader emission lines.

As can be seen in Equation 1.7, for Doppler broadening, lighter elements will have their emission lines broadened more than heavier elements in the same plasma conditions. Components within a plasma equilibrate to a thermal distribution after a few collisions. As a result, it is typically assumed that the plasma is in Local Thermodynamic Equilibrium (LTE). This allows for a temperature based analysis of the

plasma [14]. As such, Equation 1.7 becomes a simple relationship based on the temperature of the plasma. Furthermore, this relationship highlights that in a given spectral measurement, it would be expected that lighter elements, such as H, would have the broadest emission profiles.

$$\Delta\lambda_D = 7.2 \times 10^{-7}(T/M)^{1/2}\lambda_o \tag{1.7}$$

Where $\Delta\lambda_D$ is the Full Width at Half Maximum (FWHM) of the emission profile due to Doppler effects, T is the temperature of the plasma, M is the atomic mass of the emitting element, and λ_o is the central emission wavelength of the element.

As shown above, these effects, unfortunately for the work conducted in this thesis, are more pronounced in lighter elements. Using Equation 1.7 as an example, the FWHM of the emission line of Zr at 655.05 nm would be approximately 10 times narrower than the FWHM of H at 656.283 nm. This implies that serious consideration must be given to the measurement environment in an attempt to reduce line broadening as much as possible. This consideration is even more important for attempting to distinguish between the H isotopes as they will be strongly effected by broadening.

All of these effects make it difficult to analyze the results of LIBS. Thus to ease the difficulty of accurately identifying elements, a priori knowledge of the expected sample composition is recommended. Even with a priori knowledge, however,

there are sometimes unexpected contaminant species present. Some programs exist which can estimate which species are present in a given spectra, such as Lasertechnik Berlin's Sophi software, which can make the job of elemental identification easier.

In many scientific and industrial LIBS applications, calibration of emission intensities is done with a calibrated standard (i.e. a separate LIBS measurement is conducted on a sample of known composition and the relative emission intensities is used to calibrate the unknown sample under investigation). Progress is being made in the field of calibration-free LIBS where estimations of the emission parameters are made based on the characteristics of the plasma [17]. These characteristics can include the electron density and plasma temperature. From these values, one can create a fitting function which will attempt to replicate the captured data by summing various Lorentzian profiles. While LIBS plasmas emit Voigt profiles (a convolution of a Gaussian and Lorentzian) the dominant profile is Lorentzian and thus is used in most fitting algorithms. The equations of a Gaussian and a Lorentzian are shown below in Equation 1.8 and Equation 1.9, respectively.

$$I_G(\nu) = \frac{2\sqrt{\ln 2}}{\sqrt{\pi}\Delta\nu_G} \exp\left(-\left(\frac{2\sqrt{\ln 2}}{\Delta\nu_G}\left(\nu - \nu_o\right)\right)^2\right) \tag{1.8}$$

$$I_L(\nu) = \frac{1}{\pi}\frac{\Delta\nu_L/2}{(\nu - \nu_o)^2 + (\Delta\nu_L/2)^2} \tag{1.9}$$

Where $I_G(\nu)$ and $I_L(\nu)$ are the Gaussian and Lorentzian lineshapes, respectively,

$\Delta\nu_G$ and $\Delta\nu_L$ are the FWHM of the lineshapes, and ν_o is the central wavelength of interest.

Determining the plasma characteristics is often based on the lineshape of H-α since it has the most prominent changes in relation to changes in electron density and plasma temperature. The significant changes seen in the lineshape of H-α happen due to H being the lightest element.

Unfortunately, this light mass and prominent broadening result in distinction of the isotopes being difficult in a simple atmospheric LIBS setup. Although the isotopes have emission lines which are quite far apart, in some conditions this separation can be covered by the wide emission profiles of the isotopes. To combat this issue, certain groups have attempted to use various environments and techniques in order to better separate the emission lines. Different backing gases [18, 19], various measurement chamber pressures [20], and Calibration Free Laser Induced Breakdown Spectroscopy (CF-LIBS) methods [21, 22] have all been investigated for measuring distinct emission from H and D at their Balmer-alpha lines, H-α and D-α. Varying degrees of success have been obtained by these methods, however, it appears that there has only been success in measuring large concentrations of the two species only on the surface of materials. These advances are discussed in greater detail in the following section, Chapter 2: Literature Review.

1.4 Zirconium Hydride

The formation of ZrH is dictated by Zr interacting with H, and in the case of heavy water, ZrD will be formed with D. When H/D are present in quantities above the solubility limit for H/D in Zr at a given temperature. The solubility limit of H in Zr varies drastically from around 50% atomic at temperatures greater than 500^{o}C and dropping to 10^{-4}% atomic at room temperatures [23]. The excess H present in the Zr matrix results in the formation of ZrH precipitates, which can have different crystal structures based on the temperature of the material and concentration of H. These different conditions can result in the following compounds: ZrH, $ZrH_{1.6}$, ZrH_2. The resulting structures are seen as platelettes, as shown in Figure 1.3, which tend to extend throughout the entirety of the hydrided portion of the material; in the case of a CANDU reactor, this would encompass the entirely of the pressure tubes which have coolant flowing. These platelettes are thin in the radial direction while expanding outwards in the transverse and circumferential directions in the main body of the pressure tubes.

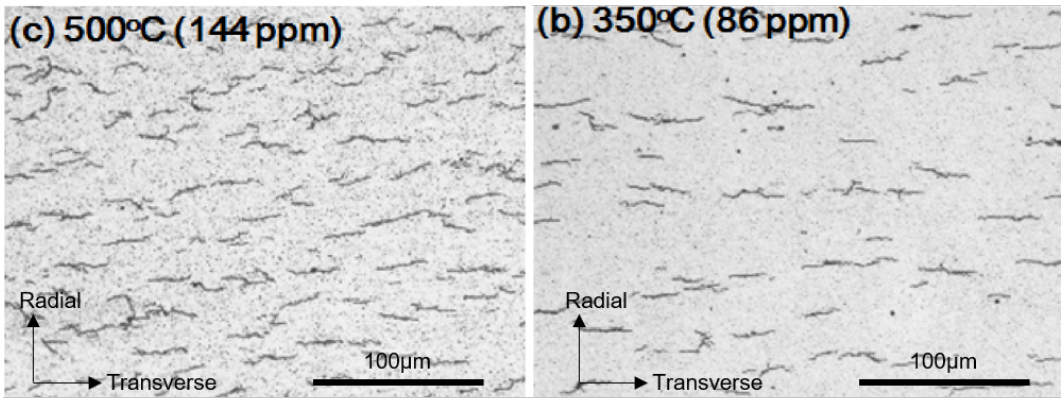

Figure 1.3: Micrographs of hydrided Zr-2.5%Nb. In this image, the darker inclusions in the bulk of the material are ZrH platelettes. Note the preferential direction of the hydrides in the transverse direction. Figure adapted from [24].

The presence of ZrH results in the reduction of the ductility of the host material, leading to a decreased fracture toughness, tensile ductility, and impact strength [25, 26, 27]. These factors imply that ZrH results in a weaker, or "embrittled" material. It is well accepted within the community that the dominating factor for hydrogen embrittlement of Zr alloys is ZrH/ZrD precipitates [5, 6]. As mentioned in Section 1.1, the formation of ZrH was one of the dominating factors in the 2 m crack which formed along one of the pressure tubes in the Pickering A CANDU reactor.

As nuclear reactors are shifted from a shut-down state to full-power, or vice versa, many of the reactor's components undergo substantial temperature changes. Pressure tubes are not exempt from this change, meaning that the solubility of H in the pressure tubes is also significantly changing. Shut-down procedures would therefore see the formation of ZrH precipitates as, for CANDU reactors, the reactor

is cooled from operational temperatures, approximately 300°C, to approximately 70°C, the ambient temperature of the calandria [4].

These concerns around the presence of ZrH in pressure tubes has led to many studies into the effects of these hydrides in Zr alloys, such as [5, 6, 23]. Additionally, the known degradation of the mechanical properties has resulted in regular inspections into the H_{eff} in reactors. These inspections follow the processes discussed in Section 1.1. Enhancing the understanding of the temporal H_{eff} evolution and the distribution of hydrides in pressure tubes would be of benefit to nuclear operators, and can be aided by LIBS.

2 LITERATURE REVIEW

LIBS has been studied since the development of pulsed laser, as scientists realized the potential for intense laser-matter interactions. The first studies of LIBS were conducted in the 1960's under the names of LIBS, Laser Induce Plasma Spectroscopy (LIPS), and Laser Spark Spectroscopy (LSS) when scientists were able to use the first pulsed lasers to generate plasmas on the surface of materials [14]. As studies of the plasmas began, scientists and spectroscopists recognized the potential of studying this plasma as a proxy of the material itself. It was quickly realized that the plasma must consist of the same material as the target itself.

LIBS is primarily used as a material identification tool and some of the uses of LIBS have included archaeological investigations [28], explosives detection [29], bacterial identification [30], and planetary geology [31]. The various applications of LIBS require different equipment and experimental parameters, however, the main components remain fairly constant. The most commonly used LIBS setup employs a short-pulsed laser focused onto a material to create a high fluence spot. This high fluence exceeds the threshold ablation fluence of the material and creates a plasma.

Detection of hydrogen isotopes, namely H, D, and T, has become an area of interest for LIBS research recently and is being primarily driven by the nuclear energy field. A by-product of some nuclear fusion reactions is tritium, a radioactive isotope whose presence must be accurately monitored. In traditional fission reactors, water or heavy water is used as a coolant, while conditions may be right to create T as well. This means that there is likely H, D, and T, or some combination, of these elements embedded in components of interest for inspection. Therefore, if LIBS were to be used for inspections, it would need the ability to distinguish between these closely emitting species to be of significant use in the nuclear industry.

As discussed in Section 1.1, the desire to measure H and D concentrations in CANDU reactors is not driven by the desire to monitor T concentrations. Rather, the presence of H and D in metals can lead to embrittlement of the metal as their abundance is orders of magnitude larger than that of T. As the concentrations of these elements exceeds the solubility limit of the metal, Zr-2.5%Nb in the case of CANDU reactors, hydrides begin to form. These hydrides weaken the material and can lead to accident scenarios if left unnoticed.

Tokyo Electric Power Company (TEPCO) is currently supporting efforts which aim to measure the concentration of H and D in Zircaloy-4, a common alloy in the nuclear industry, using standard LIBS techniques and, recently, more exotic LIBS techniques. The group has successfully been able to discriminate emission from H

and D by using a low-pressure He environment in which the ablation and plasma generation occurs. Previous experiments have suggested that due to the mass of argon, its presence should cause the plasma to remain more confined, thus leading to a hotter plasma, leading to a higher emission intensity from the plasma [15, 32]. Conversely, helium, being a lighter gas, would allow the plasma to expand more, creating a less dense plasma. This lower density contributes to a lower degree of line broadening within the plasma; a key factor when attempting to distinguish isotopes [33].

The TEPCO funded group has shown results of clear peak separation in a He environment with a D concentration of 180 ppm [19] and have extrapolated a detection limit of 10 ppm [20]. However, this lower detection limit has not been presented experimentally in their work at this time. For an inspection tool to be of use in a CANDU reactor, a detection limit around 5 ppm would be ideal as this is the typical manufacturer specification for the H concentration. However, before an inspection tool could be approved for use in a reactor, the detection limit would have to be proven experimentally on known standard samples. Furthermore, the precision and accuracy at low concentrations would have to be known before implementation.

The experimental setup being used by this group typically employs a fairly standard LIBS setup concerning the equipment. Their laser specifications are typically 10 ns, 100 mJ lasers operating at 1064 nm and 10 Hz. They sometimes use DP-LIBS to

enhance signal emission. In this setup, they have used a 54 mJ nanosecond laser as the main ablation laser and a picosecond Nd:YAG laser with 2 mJ pulse energy acting to re-excite the plasma [20].

Their detectors include a seemingly custom built Atago Optical Multichannel Analyzer (OMA) [19] and a high resolution McPherson spectrometer coupled to an Andor iStar ICCD [20]. With both of these detector setups, the group has been able to successfully distinguish the H-α and D-α emission lines. These measurements were most successful when made in He environments.

Research into H isotope detection is also being conducted by organizations working on the materials science of JET and ITER [21, 22, 34, 35, 36, 37]. Fusion reactions generate D and T as by-products which can become embedded in the walls of their fusion chambers [10]. To perform in situ monitoring of the concentrations of these isotopes, LIBS instruments are being developed. These groups have also made significant progress in using CF-LIBS to use plasma parameters, such as the plasma temperature and the electron density, to estimate the emission parameters of the various species expected in the plasmas [21, 35]. These emission parameters allow them to perform a fitting algorithm using either Lorentzian or Voigt profiles to fit the data and provide an estimation of the concentration of each of the species in the spectrum. This method requires a priori knowledge of the expected constituent elements, however, eliminates the need for calibration samples to be used in concert

with every measurement [21, 35].

There still exists a need within the community to measure metallic samples with heterogeneous H structures and concentrations throughout the bulk of the sample. Such a device would prove to be of use in CANDU reactors and similar reactors as it would provide an ability to understand the health of critical reactor components without the need for expensive and time-consuming techniques. The research presented in this thesis was conducted in pursuit of this goal with a specific focus on detecting emission from H and D in Zr-2.5%Nb.

3 EXPERIMENTAL METHODS

During the course of this experimentation, two different laser systems were used to see the differences between plasmas and ablation craters created by high-powered nanosecond lasers and high-powered picosecond lasers. Additionally, a variety of spectrometers were tested throughout experimentation to determine the necessary specifications for a LIBS system intended for simultaneous detection of H and D. A DP-LIBS system was not available for testing, however, it is included in future recommendations as a method to improve the SNR.

3.1 Nanosecond Laser Setup

A research visit to Dr. Steven Rehse's LIBS laboratory at the University of Windsor was conducted to utilize a nanosecond laser based LIBS system. This system used a pulsed Nd:YAG laser with an attenuated pulse energy of 100 mJ, a pulse duration of 10 ns, and was operated at a repetition rate of 10 Hz (ec. Plasma emission was captured by a 500 μm core multimode optical fibre feeding into a Lasertechnik Berlin (LTB) Aryelle Échelle spectrometer with a spectral range of 200 - 800 nm and a 22 pm spectral resolution. Control over the laser was conducted by an LTB LIBS Control Box which offers control over the laser and spectrometer through

LTB's Sophi software.

Samples were placed on a three-axis stage allowing for the lens to sample distance to be modulated as the beam travelled perpendicular to the optical table at the end of its path. This mobility ensured that the focal point of the laser could be placed slightly under the surface of the sample. Determination of the interrogation site location was accomplished by used of two low-powered, red Helium Neon (HeNe) lasers and a camera system. The height of the stage was adjusted until the two HeNe spots were overlaid; at which point the location of the interrogation site would be known and the sample was known to be at the ideal height for plasma generation. It is worth noting that the depth of focus was large enough to allow for multiple ablations to be performed without the need to change the sample height every pulse.

The measurement environment for this experimental setup was a sealed plexiglass chamber with the ability to flow different buffer gases into the chamber. The flow of gas into the chamber caused a slightly pressurized environment, driving atmospheric gases out of the chamber. Figure 3.1 shows a schematic of the measurement chamber used during the nanosecond LIBS experiments.

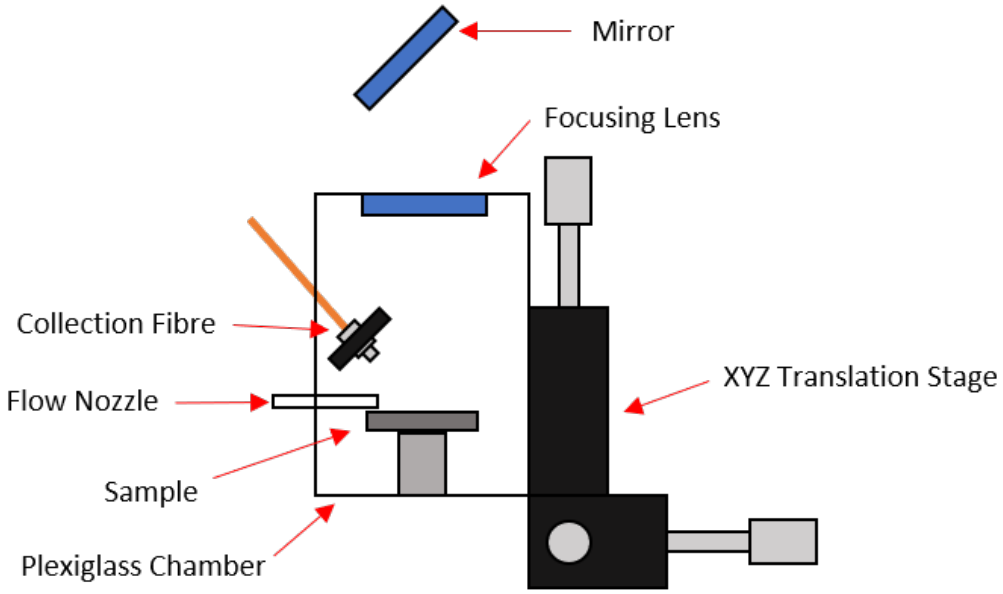

Figure 3.1: Schematic diagram of the measurement chamber that was used in the nanosecond LIBS experiment. Not shown is the inlet gas selection system. A series of valves connected to various gas bottles allowed for selection of the flow rate and gas.

During these experiments, tests were performed in atmospheric air, argon, and helium environments to observe the effects of different buffer gases during measurement. As discussed in Chapter 2: Literature Review, these different measurement environments would likely lead to different emission profiles. The intention of testing with these buffer gases was to see if D-α emission could be enhanced.

Similar to the picosecond LIBS setup, discussed in the following section, the rest of the nanosecond setup was fairly simple. The main difference between the setups was that the nanosecond setup included an exchangeable neutral density filter which could be placed in the beam path before the first mirror to decrease the laser's

intensity. Figure 3.2 shows a schematic diagram of the nanosecond laser setup used during this experimentation.

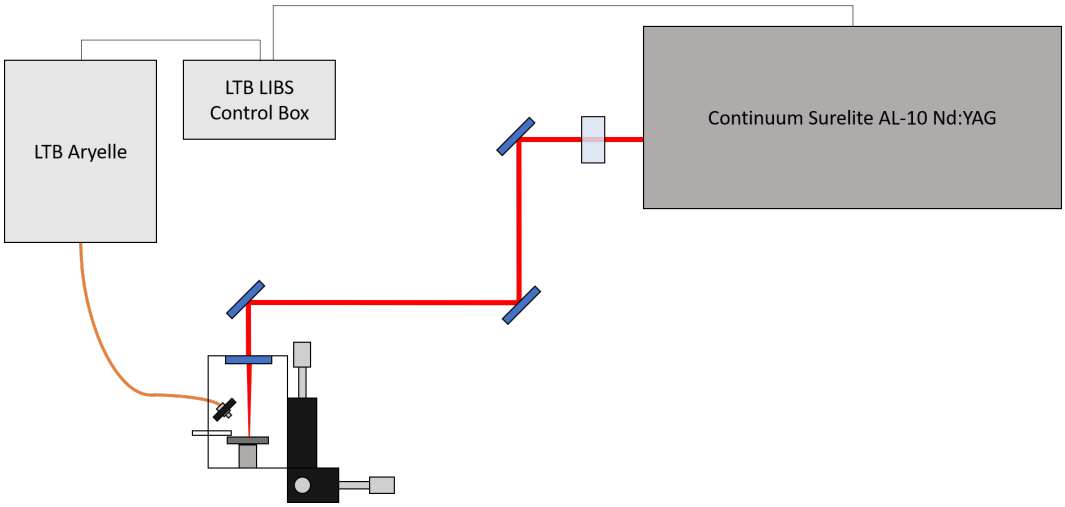

Figure 3.2: Schematic diagram of the nanosecond LIBS setup.

3.2 Picosecond LIBS Setup

3.2.1 Laser

The laser used in this system was a Passat Compiler355 Diode-Pumped Solid State Laser (DPSSL), which is a 3 output Nd:YAG laser with simultaneous outputs of 355 nm, 512 nm, and 1064 nm laser light. For this experiment, only the 1064 nm output was used. At 1064 nm, the laser had a pulse duration of 8 ps and a pulse energy of 160 µJ; the repetition rate was internally controlled and user-selectable from 1 - 200 Hz in 1 Hz increments or could be externally controlled by use of a pulse generator with the same range available.

The laser was directed to the sample by use of three metallic mirrors mounted to Thorlabs kinematic mounts, allowing for a high degree of control over the beam path. The laser was passed through a 100 mm focal length best-form lens with an anti-reflective coating for 1050 - 1700 nm (Thorlabs LBF254-100-C). The sample was mounted to a miniature three-axis stage (Thorlabs DT12XYZ) with 1/2" travel in each direction allowing for the sample to be manipulated over a wide range of positions.

The focal spot of the laser was initially focused to be slightly below the target material's surface. To determine the best focal distance, the sample was moved closer or further from the focusing lens until the most intense plasma was achieved as measured on the spectrometer in use.

3.2.2 Spectrometer

Due to budgetary and time constraints, it was not possible to procure a dedicated spectrometer for this experimentation. Therefore, a series of spectrometers were rented. This unfortunately meant that time was limited with each of the units, however, acceptable results were still obtained. This arrangement, however, had the benefit of allowing for an exploration of what features would be necessary for further phases of this project.

Three spectrometers were tested with this setup. Firstly, a Princeton Instruments

FERGIE spectrometer was installed in the experimental setup. The FERGIE had a diffraction grating with 1800 lines/mm installed, giving the system a maximum resolution of 0.168 nm at 656.283 nm, which is the H-α emission line, with a 25 μm slit installed. While this resolution was not sufficient to distinguish H and D emission, it allowed for the LIBS setup to be designed while procurement of a higher resolution spectrometer was ongoing. The FERGIE also boasted a decently sensitive integrated CCD array, giving an acceptable SNR during LIBS measurements. Figure 3.3 shows a schematic diagram of the picosecond laser setup with the Princeton Instruments FERGIE which was used during this experimentation.

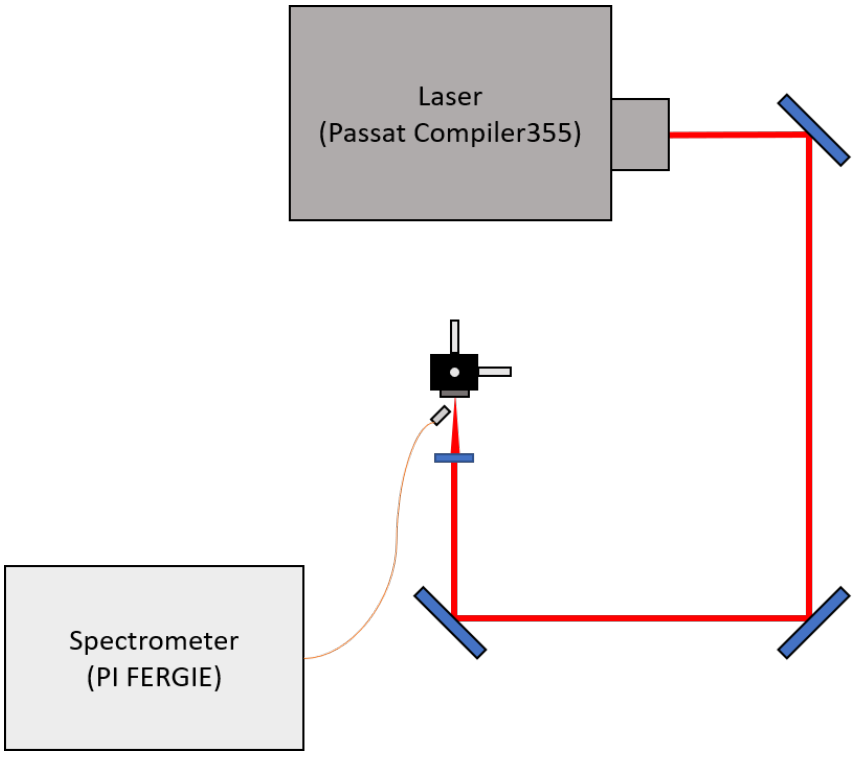

Figure 3.3: Schematic diagram of the LIBS experiment using the Princeton Instruments FERGIE spectrometer.

The Princeton Instruments FERGIE also lacked the ability to be properly operated as a LIBS spectrometer without significant modification. It was found over the course of experimentation that the internal CCD detector continues to collect light over the course of its readout period, not just during the gated period. The readout period was approximately 6.8 ms on average based on the settings being used. This meant that the gate width that was set in the software was essentially inconsequential as any gate width of interest for LIBS would be dominated by this long readout period. Light collection over this extended period also generated results with poor SNR characteristics.

To make the Princeton Instruments FERGIE LIBS compatible, part of the CCD would have to be physically blocked such that the unit's spectra kinetics mode could be used. The spectra kinetics mode captures light on a user defined number of rows before pushing that charge to the next set of rows on the CCD. However, during this shifting, the CCD continues to collect light if not physically obstructed. As the unit was a rental, modification to this extent was not allowed.

To attempt to distinguish H-α and D-α emission, a LightMachinery HyperFine spectrometer was employed as the second spectrometer in this experimental setup. The HyperFine boasts a 10 pm resolution over a 10 nm window; specifications well within the need to distinguish the 183 pm difference between H-α and D-α. The resolution performance of the device was confirmed with calibration sources and

by the use of a HeNe laser emitting at 632.8 nm. With these sources, the measured FWHM of the lines were well within expected values. It was confirmed that the unit should be able to easily measure distinct lines of H-α and D-α, assuming that the lines were not broadened to an extent where they significantly overlapped.

Despite the high resolution of the LightMachinery HyperFine spectrometer, the light throughput was limited and a LIBS measurement was not possible. Using gate widths which would be applicable to spectroscopic measurements, no signal was recorded by the instrument. The manufacturer provided both onsite and online assistance, but was unable to resolve the light throughput issue. Various optical setups were attempted, including butt-coupling the plasma emission into the optical fibre and observing the plasma through a one to one imager setup. This inability to measure a plasma was seen both with the smaller plasma of the picosecond laser described in Section 3.2.1 and also with an 80 mJ, 10 ns, 1064 nm Nd:YAG laser generating a substantial plasma. Using the HyperFine spectrometer, plasma emission could only be captured by firing the laser at 200 Hz and setting the gate width to at least 5 seconds. With this setup, plasma emission could be seen, however, the intensity was low, with a SNR of approximately 1.5 which was unacceptable for this application. Furthermore, this type of measurement would not constitute a LIBS measurement.

Finally, a Princeton Instruments 328 mm, f/4.6 Schmidt-Czerny-Turner (SCT) spec-

trometer (Isoplane SCT 320) connected to a Princeton Instruments PIMAX ICCD (25 μm pixels) was implemented into the experimental setup. This spectrometer was chosen due to its known performance as a LIBS spectrometer [38, 39, 40]. A high-resolution, high-throughput spectrometer, such as the Isoplane SCT 320 would have been selected earlier in the project, however, such a unit was unavailable for rental until very late in the testing phase and was only available for a limited time. The spectrometer was setup with a 1800 groves/mm and 500 nm blaze angle diffraction grating, and a 10 μm entrance slit width, leading to a resolution of 39.1 pm at 656.283 nm. Additionally, the use of an ICCD allowed for extremely fast gate closing, with the PIMAX boasting a rise time of < 1 ns [41]. For these experiments, the internal delay generator of the PIMAX camera was used to allow for easier modulation of the gate delay and gate width.

This final experimental setup also employed a vacuum chamber to reduce the linewidths of the species of interest. The incident laser was focused through a window with low absorbtivity in the near-infrared to ensure that maximum energy was delivered to the target. Collection of the plasma emission was achieved by a butt-coupled fibre placed inside of the vacuum chamber and out-coupled through a 600 μm Thorlabs fibre optic feedthrough (Thorlabs VC2L6S). This setup ensured that the maximum light collection from the plasma was achieved with minimal loss through the connections. To ensure maximum light collection, all fibres in this setup used the same core diameters and numerical apertures. Figure 3.4 shows a schematic diagram of

this experimental setup and Figure 3.5 shows a picture of the experimental setup.

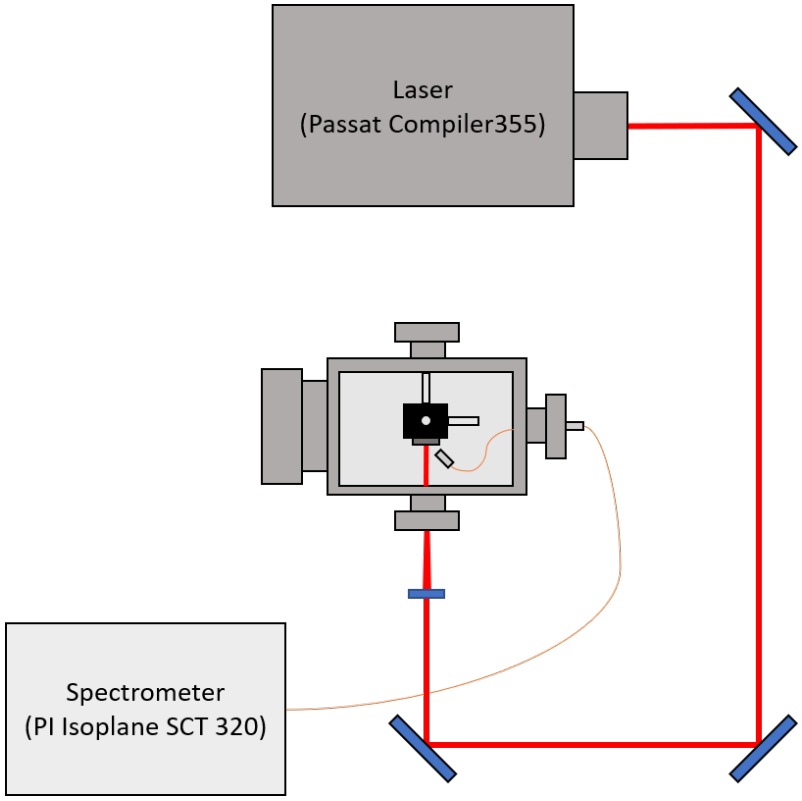

Figure 3.4: Schematic diagram of the LIBS experiment using the Princeton Instruments Isoplane SCT 320 spectrometer and vacuum chamber.

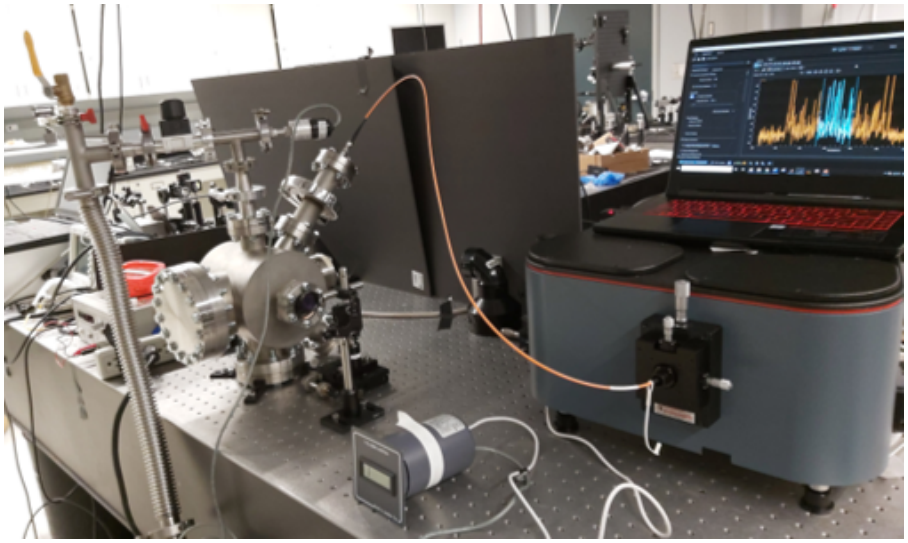

Figure 3.5: Picture of the LIBS experiment using the Princeton Instruments Isoplane SCT 320 spectrometer and vacuum chamber.

To determine the required gate delay time, the gate width was set to 100 ns (this was found to be the minimum gate width which still allowed a decent SNR and observable signal) and the gate delay was stepped in 10 ns increments. This method allowed for an accurate determination of when the plasma first ignited, and thus allowed the experimental gate delay baseline to be determined. This period before plasma ignition accounted for the propagation delay of the signal from the PIMAX ICCD to the laser, the firing time for the laser to receive the input signal and release a laser pulse, and the travel time of the light from the laser to the sample. Knowing this parameter, the gate delay was modulated from 500 ns to 10 µs to determine the ideal delay for observing D-α emission. Additionally, the intensifier gain was held constant at 50$\times$ to allow for consistent comparison between the spectra.

By this procedure, the best detection parameters were found to be a gate delay and gate width of 500 ns. With these parameters, both H-α and D-α signals could be seen.

3.3 Vacuum Chamber

It was known that the linewidths of LIBS emission lines can be decreased by using a vacuum environment of air [42]. The reduced pressure environment results in a cooler plasma, meaning that the broadening mechanisms are suppressed. Additional enhancement can also be achieved by using a low-pressure buffer gas [20, 33], however, that phenomenon was not explored in this work due to time and cost constraints.

The vacuum was formed by an oil-diffusion pump since only rough vacuum environments were needed. The pump was capable of pumping the chamber pressure down to $<$ 150 mTorr, however, higher pressures were used during experimentation. To avoid the back flow of oil into the vacuum chamber, an isolation valve was installed between the chamber and the pump with a bleed valve installed to allow the pump to have atmospheric pressure held when shut off. Failure to reopen the bleed valve would have resulted in the vacuum environment pulling oil from the pump and contaminating the equipment.

Figure 3.6 shows a schematic diagram of the vacuum chamber used in these experiments and Figure 3.7 shows a picture of the vacuum chamber setup. All of the main

chamber fittings were of the CF variety and used copper gaskets, with the exception of the large access port. This port was constructed with a rubber gasket, allowing for the port to be opened many times before needing to replace the gasket. Furthermore, an adapter connecting the CF flange to a KF flange was used for connecting the chamber to the rest of the vacuum system, including the isolation valve and pressure gauge.

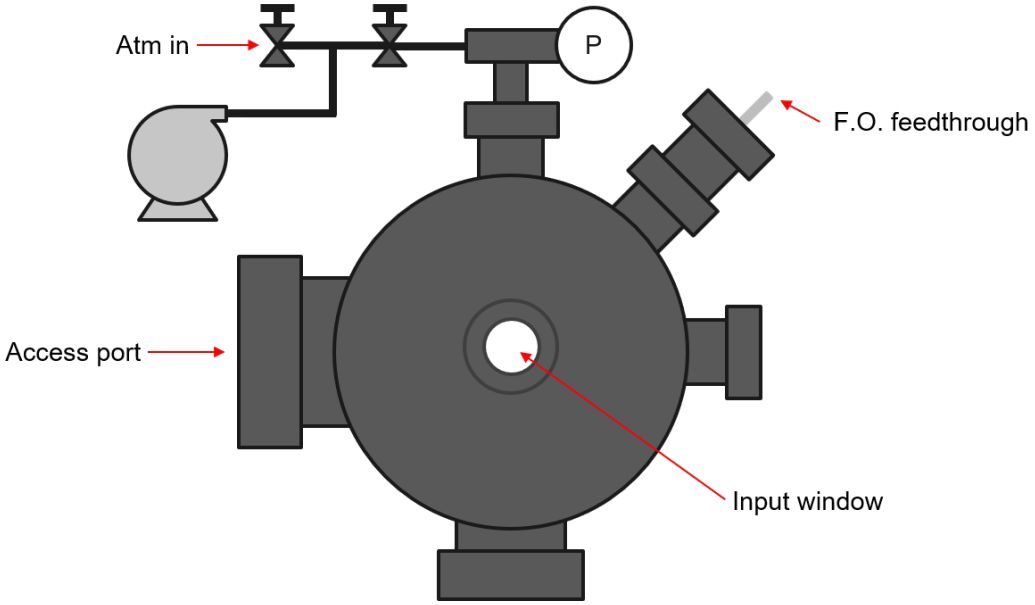

Figure 3.6: Schematic diagram of the vacuum chamber used during experimentation.

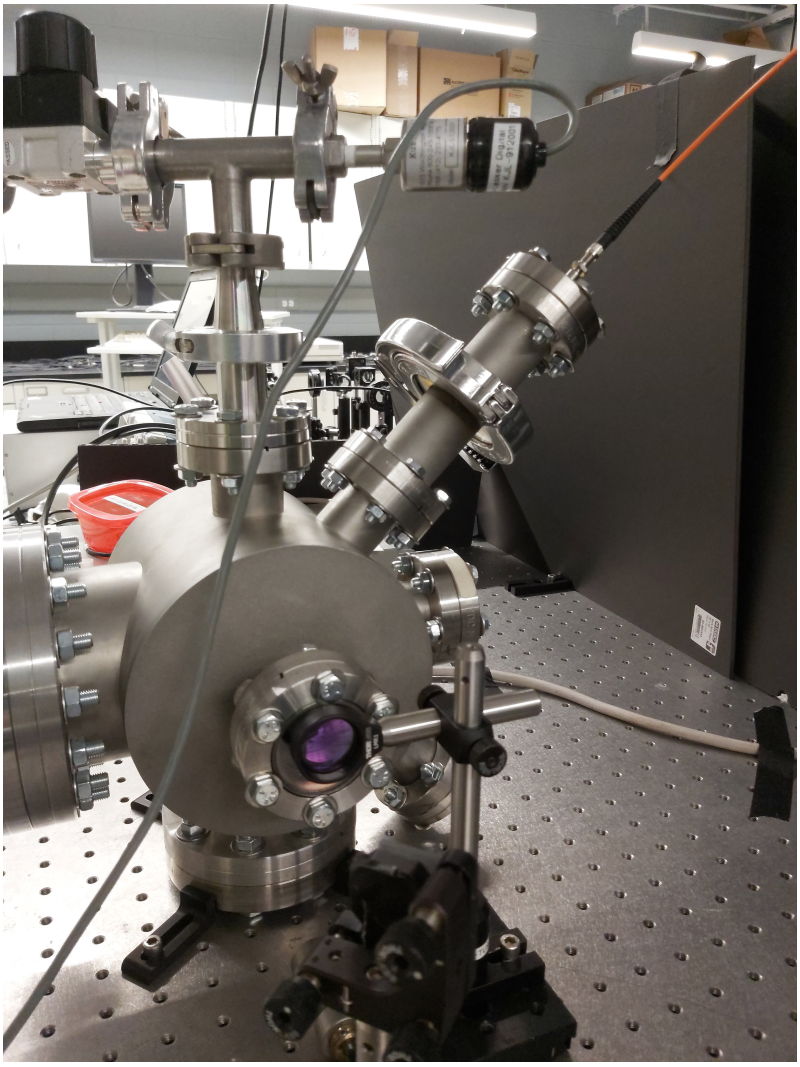

Figure 3.7: Picture of the vacuum chamber installed in the picosecond LIBS experiment.

An ideal vacuum chamber for this experiment would include a load-lock system whereby the chamber would not be exposed to the surrounding atmospheric environment when samples were exchanged. The vacuum chamber used in this experiment did not have this feature due to schedule and cost restrictions. In an effort to mitigate the effects of atmospheric contaminants in the vacuum chamber, a

minimum of a 5 minute pump out was performed on the chamber after each time the chamber was exposed to atmosphere. Following the pump down, the chamber would be isolated and the pressure change closely monitored. If the leak rate exceeded 1 mTorr/s, the pump down routine would be performed again. This leak rate is attributed to out-gassing of atmospheric contaminants from the chamber walls.

While experiments were running, the chamber isolation valve would be slightly opened with the pump running to maintain the chamber pressure at the desired value. The isolation valve typically needed to only be very slightly open as the amount of material ablated was quite small. Additionally, due to the pump-down routine, the leak rate of the chamber was very low, < 1 mTorr/s.

3.4 Sample Preparation

The pressure tube samples used throughout this work were made of Zr-2.5$\%$Nb, an alloy of zirconium used throughout the nuclear industry due to its strength and transparency to neutrons. These samples were provided by a third party and were prepared to varying average hydride concentrations through an electrolysis process. The samples were emerged in a bath containing sulfuric acid and water, or heavy water for deuteriding samples, for five days to build up a hydride/deuteride layer on the outer surfaces of the sample. The samples were then annealed for seven days at various temperatures in order to achieve the target concentrations, calculated based

on 3.1 from [43].

$$TSSD = 8.08 \times 10^4 \exp(\frac{-34500}{RT}) \times [H](\ ppm) \tag{3.1}$$

Where $TSSD$ is the terminal solid solubility of dissolution, R is the ideal gas constant, T is the annealing temperature, and $[H]$ is the effective hydrogen concentration in ppm.

Prior to the hydriding/deuteriding process, it is known that nuclear grade Zr-2.5$\%$Nb contains between 5 - 10 ppm [H] from manufacturing of the alloy. Additionally, due to impurities in the solutions used in the electrolysis process, the H concentration increases in the samples.

The samples produced by this method had their impurity concentrations confirmed by HVEMS. These mass spectrometry measurements were made at three locations along each sample, with the tested portions being removed from the host sample by mechanical punching. This approach ensured that the samples were not excessively heated and allowed for samples to be taken from the middle of the hosts without cutting up the samples more than necessary. Further polishing of the samples was conducted to remove the built-up hydride layer left by the electrolysis process.

The HVEMS system measured the H and D concentration by heating the sample to 1100°C using RF induction coils to break the bonds of the ZrH/ZrD molecule and cause the H and D to escape the matrix in the gas phase. Sample heating is

conducted in a vacuum environment to lower the chance of incorrect measurements due to collecting of atmospheric gases. The gas released by heating the sample is extracted into a collection chamber by a turbomolecular pump. Gas stored in this chamber is leaked into the mass spectrometer which has the capability to distinguish between various isotopes.

Independent confirmation of the presence of both H and D in the Zr-2.5%Nb samples was conducted at a mass spectrometry facility, specifically Thermal Desorption Spectrometry (TDS), at the University of Toronto. During these tests, the chamber pressure is reduced to approximately 10-8 Torr, then the temperature was increased slowly to limit the instantaneous release of either gas, which was transferred to a measurement chamber by a turbomolecular pump. In this measurement chamber, a mass spectrometer capable of isotopic distinction measured the elements captured. To differentiate between H and D emission, their signals were measured by HD and D_2. These measurements are shown in Figure 3.8 and Figure 3.9.

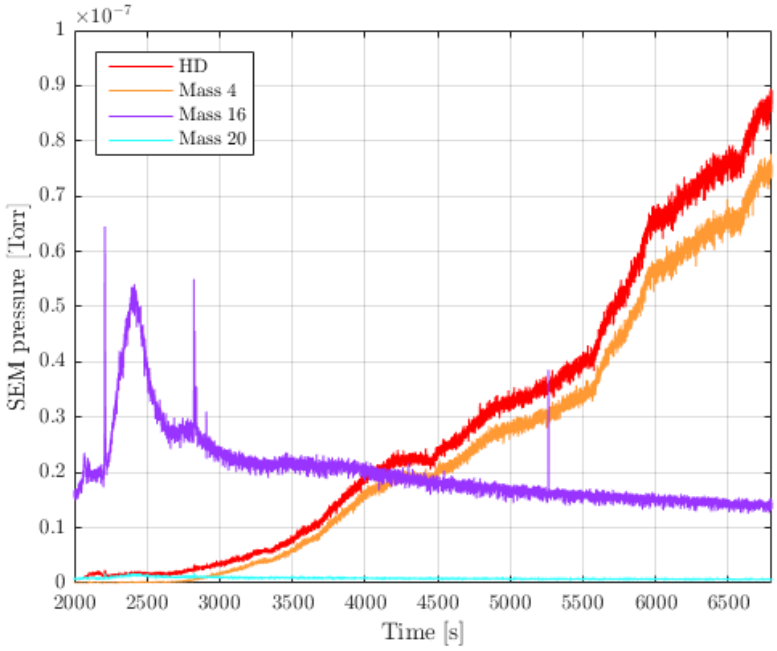

Figure 3.8: Mass spectrometry data showing the presence of hydrogen and deuterium within the same Zr-2.5%Nb sample. In this figure, the red line (HD) indicates the release of a gas with an atomic mass of 3, which is present as HD gas, the orange line (Mass 4) indicates the presence of D2 gas, the purple line (Mass 16) indicates the presence of O2 gas, which is escaping from the oxide layer on the sample, and the teal line (Mass 20) indicates the combined presence of CD4 and D2O (The Hiden QMS system lacks the resolution to distinguish between those species). Note the system was undergoing

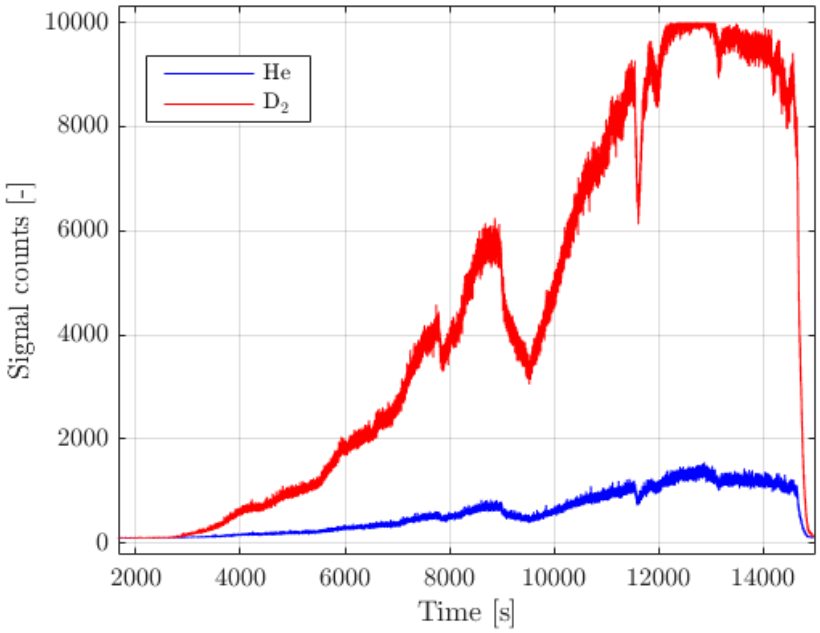

Figure 3.9: Mass spectrometry data showing the presence of deuterium gas within a Zr-2.5%Nb sample. This measurement was taken concurrently with the measurement shown in Figure 3.8.

Unfortunately, a quantitative measurement of the H and D concentrations was not possible due to the system limitations. The system was designed to handle thin film samples, whereas the sample tested was a rectangular prism with dimensions of approximately 6 mm $\times$ 6mm $\times$ 4 mm. It should be noted that the sample was slowly cut from a pressure tube ring section on a band saw to limit the amount of heat generated. During testing the amount of H and D released from the sample saturated the detector, however, it did measure the presence of both gases.

4 RESULTS AND ANALYSIS

4.1 Material Effects

Laser ablation is a process which removes material from a target material by intense laser-material interactions. The phenomena governing the specific interaction between the laser and the material are dependent on the interaction time scale. The subsequent sections will discuss the specific ablation mechanisms for nanosecond and picosecond interactions and will show the differences in the material impacts between the two pulse duration regimes. For reference, the pulse duration of a laser is considered to be the temporal FWHM of a Gaussian pulse shape.

Chichkov et. al. published a collection of theoretical models and qualitative explanations of the mechanisms behind femtosecond, picosecond, and nanosecond ablation of solids [44]. The primary difference between the three regimes is the relation between the pulse duration, τ_p, the electron cooling time, τ_e, and the lattice cooling time, τ_l. The electron cooling time and lattice cooling time can be defined as follows in Equations 4.1 and 4.2, respectively, from [44].

$$\tau_e = \frac{C_e}{\gamma} \tag{4.1}$$

$$\tau_l = \frac{C_l}{\gamma} \tag{4.2}$$

Where C_e is the heat capacity of the electronic system, C_l is the heat capacity of the lattice system, and γ is the electron-lattice coupling parameter. This electron-lattice coupling parameter describes the energy transfer between the two systems of a given atom [45]. Typically, the electron cooling time is on the order of 0.01 - 1 ps [45, 46], whereas the lattice cooling time is on the order of picoseconds [47].

4.1.1 Nanosecond Ablation

Laser-matter interactions at the nanosecond timescale are quite different from those experienced during shorter pulses. This is the regime where the laser pulse duration is significantly longer than the lattice cooling time, $\tau_p >> \tau_l$ [44]. Thermal effects are the dominating ablation mechanism during nanosecond pulses as the lattice begins to transfer energy while the pulse is still interacting with the sample. This results in a different characteristic crater shape when compared to picosecond ablation.

Firstly, evidence of melting can be seen in craters formed by nanosecond lasers. Particularly this is seen in the corona which surrounds the ablation crater and the splattering of material around the crater. See Figure 4.1 for an image of a nanosecond ablation crater. As will also be shown for picosecond ablation, a discolouration effect can be seen surrounding the ablation crater.

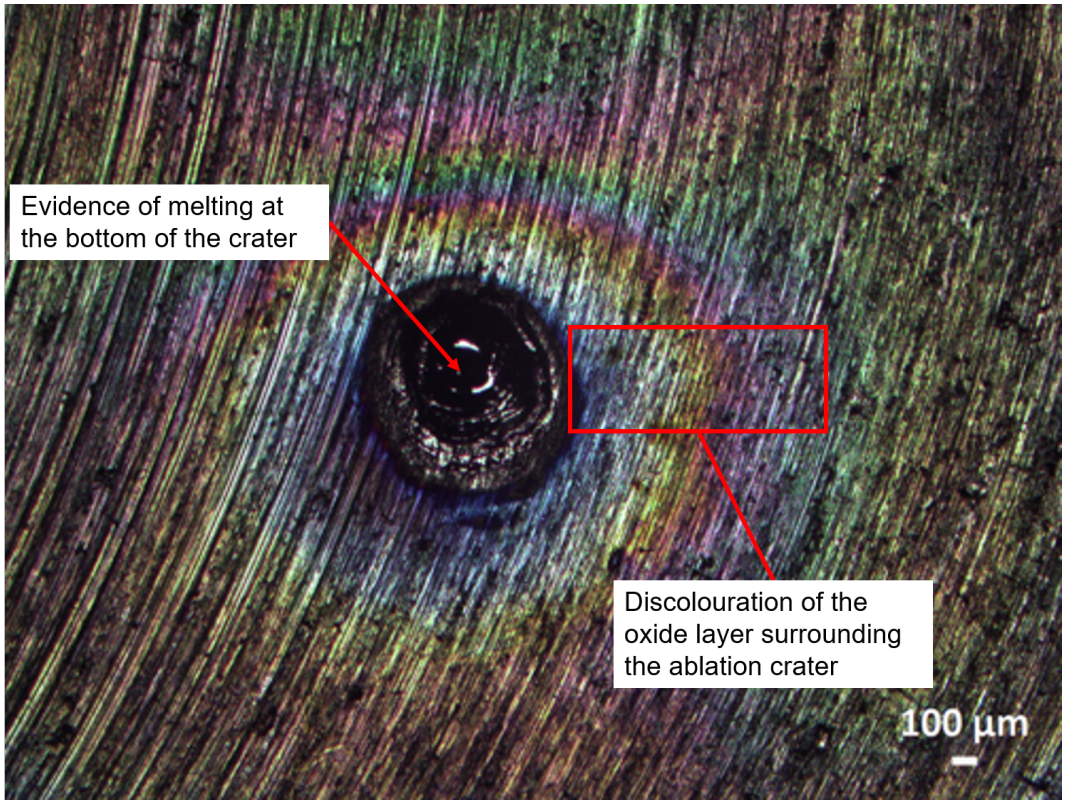

Figure 4.1: Optical micrograph of an ablation crater from the nanosecond laser described in Section 3.1. The ablation crater shown here is the result of 155 pulses.

The ablation crater formed with this laser was much larger than the one created with the picosecond laser as the larger pulse energy allowed for a larger spot size while still achieving significant ablation (i.e. the incident fluence was larger). This effect also implies that any measurement made with the nanosecond LIBS setup would be more representative of the average material composition of the entire sample. This is specific to cases like measurement of H/D content in Zr-2.5%Nb where the material system of interest is heterogeneous; that is the distribution of hydrides is heterogeneous. By ablating a larger volume, the likelihood of a single measurement

having a H/D content closer to the true average of the entire sample is higher; the limiting case being measurement of the entire sample at once.

Additional studies of the material effects were conducted using an Alicona Infinite Focus G5 3D Surface Measurement System interferometer to further study the ablation characteristics. This instrument allowed for a 3-dimensional reconstruction of the crater shape and depth profile. Figure 4.2 and Figure 4.3 show the results of measurements from this instrument.

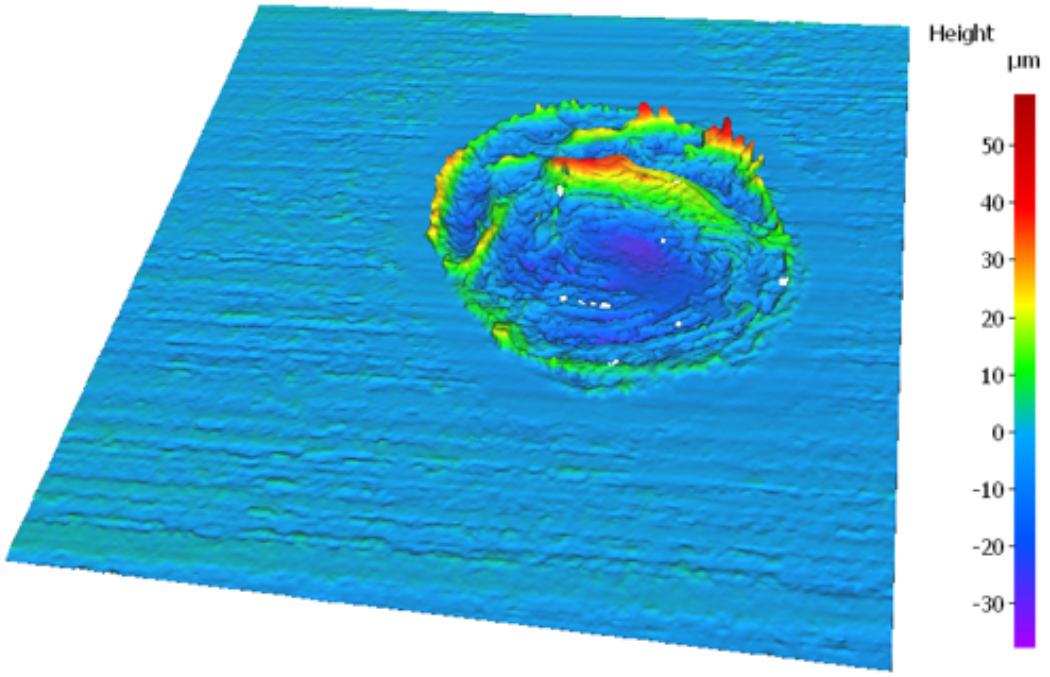

Figure 4.2: 3-dimensional colour map profile measurement of an ablation crater formed by the nanosecond laser described in Section 3.1. The ablation crater shown here is the result of 155 pulses.

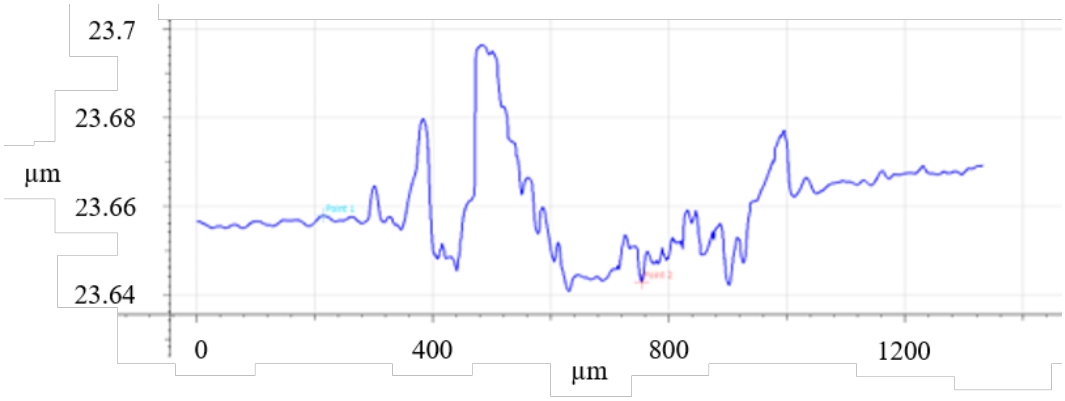

Figure 4.3: Optical profilometry measurement of an ablation crater formed by the nanosecond laser described in Section 3.1. The ablation crater shown here is the result of 155 pulses.

Looking at the profile in Figure 4.3, the ablation rate of the nanosecond laser on Zr-2.5%Nb can be found to be approximately 100 nm/pulse. The total volume ablated is also approximately 1000× larger than the volume ablated with the picosecond laser. This difference is attributed to the much larger energy deposition given by the nanosecond laser. Additionally, traditional features associated with nanosecond ablation can be easily seen in this profile view. The main feature indicative of nanosecond ablation present here is the corona surrounding the ablation crater. This feature forms from the re-deposition of molten material away from the center of the crater subsequent solidification and a surface tension effect. As the material cools, the variation in surface tension causes material to be pulled from the center of the crater to the cooler edges, leading to material build up.

4.1.2 Picosecond Ablation

In the picosecond regime, a scenario exists where $\tau_l > \tau_p > \tau_e$; this means that the laser is interacting with the material for a longer duration that it takes for the electrons to cool, however, the lattice does not have time to significantly heat from electron-phonon interactions [44]. In picosecond laser interactions, the majority of the heating is therefore coming from the laser interacting with the electrons and transfer of energy between the electrons and the lattice is limited.

Due to the faster interaction time of picosecond ablation as opposed to nanosecond or longer pulses, very little lattice heating and melting occurs. Rather, the mechanism governing picosecond ablation is commonly referred to as "phase separation" [48, 49]. The process begins with electrons absorbing the incident radiation in the early phase. This process rapidly heats the material which can create a superheated liquid, a liquid where the temperature exceeds the boiling point. Near the critical temperature, the thermodynamic properties of the material are unstable and density fluctuations leads to bubble nucleation in the material [48]. These bubbles will continue to grow and eventually lead to the explosive ejection of material because of the pressure build up in the material [48, 49, 50]. This hot, ejected material can then result in plasma formation. The plasma consists of electrons, atoms, and ions of the target material. In the early, hotter stages of the plasma, more ions are present, however, as the plasma cools, electrons have sufficiently low energy such that they

may recombine with ions in the plasma, forming neutral atoms.

It is also possible to calculate the ablation threshold of Zr, that is the lowest fluence which would cause the material to ablate. Equation 1.1 was used to calculate the ablation threshold of Zr, which was found to be 0.224 J/cm^2. Unfortunately, it was not possible to calculate the ablation threshold of Zr-2.5$\%$Nb as certain optical parameters of the material are not known which would be needed for the calculation.

The end result of picosecond ablation is a fairly clean cut into the material with a conical shape. Figure 4.4 shows a side view of the ablation profile into Zr-2.5%Nb following 10000 pulses at a repetition rate of 10 Hz. The laser was aimed perpendicular to the surface of the sample and focused with a 40 mm focal length lens. With this lens, the spot size of the sample was found to be 45 μm, giving a fluence of approximately 10 J/cm^2. Throughout the test, the lens to surface distance was modulated to maintain the largest plasma as plasma size was one of the primary concerns for each experiment.

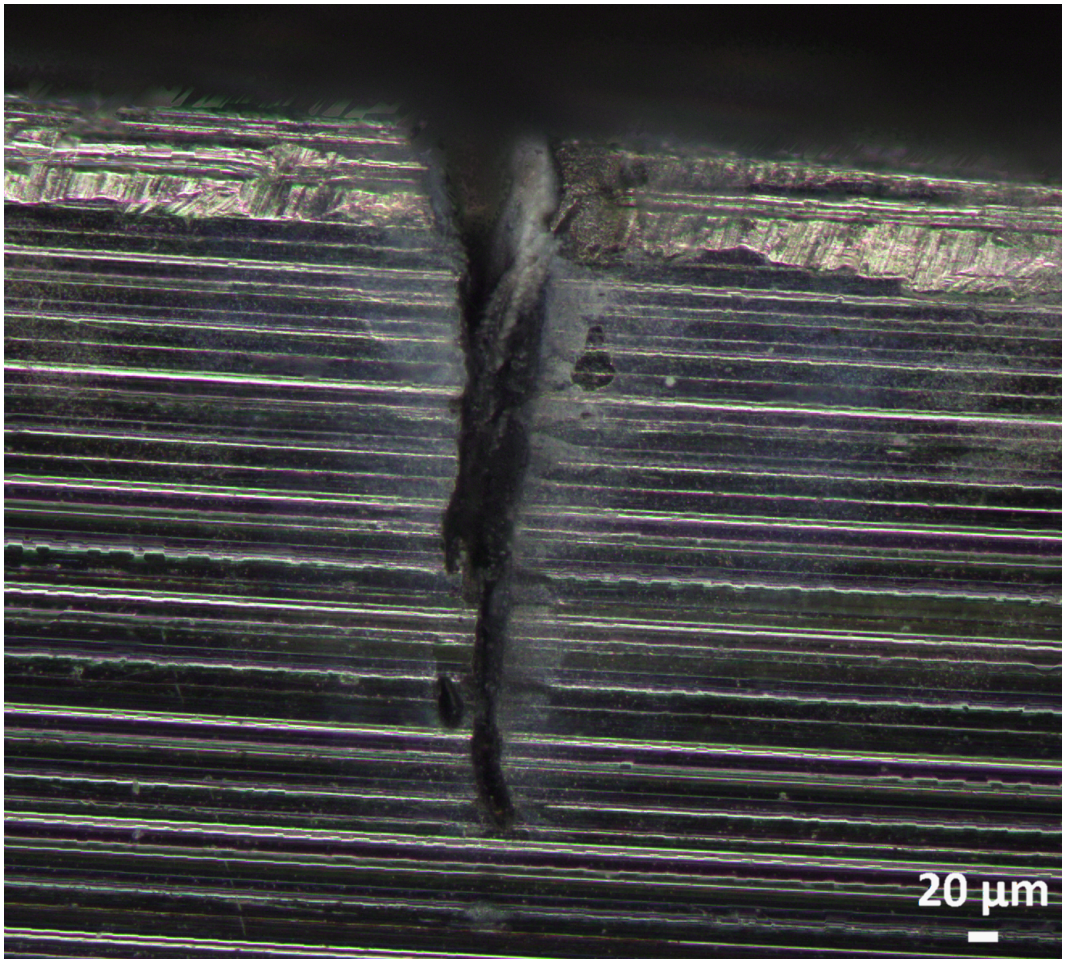

Figure 4.4: Optical micrograph of the side of an ablation crater created from 10000 pulses at 10 Hz from the picosecond laser described in Section 3.2. It is recognized that this crater shape is not ideal for use in a reactor environment. Future work will explore methods for improving the crater morphology.

The conical shape of the ablation crater would result in self-focusing of the laser pulse into the crater, furthering the propagation of the conical profile. The self-focusing effect arises from the laser reflecting off the inner walls of the cavity at oblique angles. These reflections guides the light towards the narrowed bottom of the cavity. Leitz et al. showed similar results when drilling through metal sample

with a picosecond laser [51]. They further show that after drilling through the entire sample the profile will eventually achieve a roughly cylindrical shape as the laser reflections in the cavity and plasma interactions continue to widen the channel [51].

The surface of the material shows a roughly circular feature inside of an elliptical feature as seen in Figure 4.5 and 4.6. Upon further inspection, it can be seen that the ablation crater follows a conical profile, which is discussed later. The formation of the elliptical structure is believed to appear due to the presence of Zirconium Oxide (ZrO_2) on the surface of the material. ZrO_2 is a ceramic material, as opposed to a metal like the rest of the Zr-2.5%Nb. Ceramics are known to suffer from flaking during laser ablation, which can lead to non-circular ablation craters [52, 53].

Beyond the elliptical feature, surface discolouration can be seen around the ablation crater in Figure 4.5. This effect has been seen in other materials, such as glasses [54] and zinc [55]. The exact cause of this effect is not known, however, it is likely due to interaction of the material with low fluences of laser light [55]. Additionally, this feature is similar to heating that is seen during welding and other high-temperature processes. As the laser used in this experimentation has a Gaussian profile, the light extends well beyond the actual ablation crater, which could have led to the discolouration around the crater.

In Figure 4.6 the multi-colour discolouration is no longer present. Mustafa et al. saw a similar behaviour with increasing numbers of pulses [55]. The postulated

explanation is that as the number of pulses on a given spot increases, the amount of material redeposited around the crater also increases. This redeposited material then masks the discolouration effect [55].

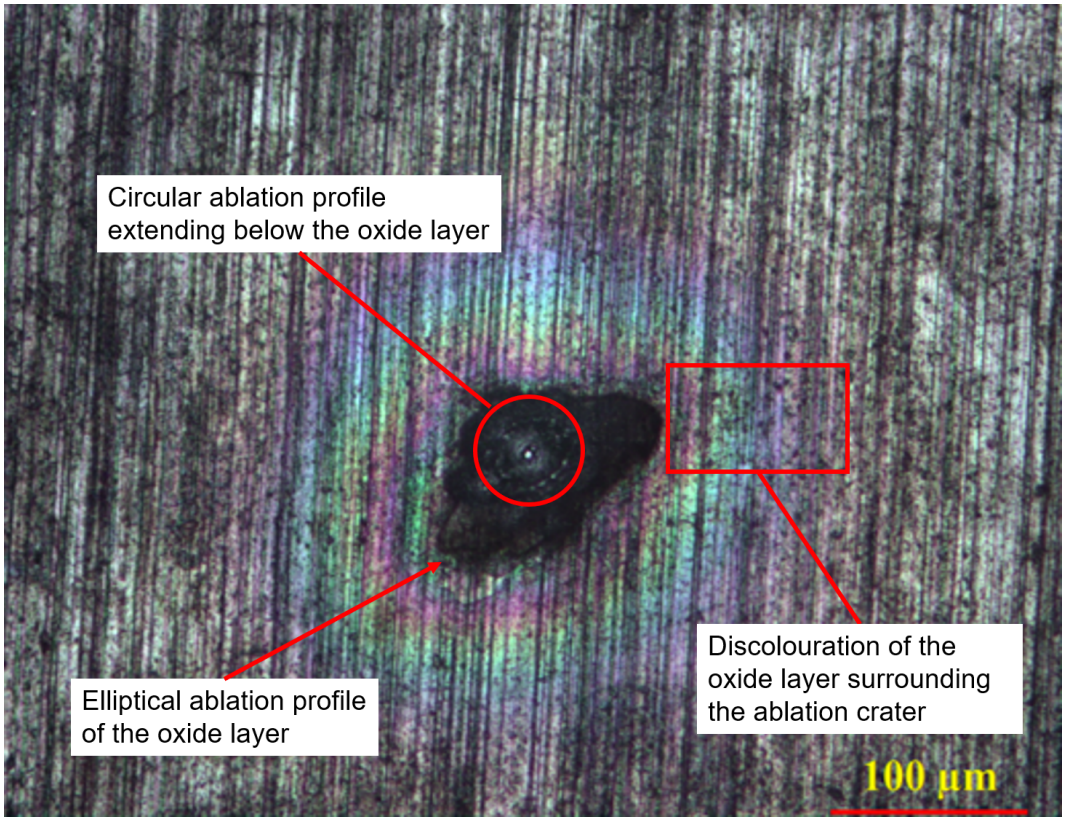

Figure 4.5: Optical micrograph of the top of an ablation crater created from 100 pulses at 2 Hz from the picosecond laser described in Section 3.2. Discolouration of the surface surrounding the ablation crater can be seen.

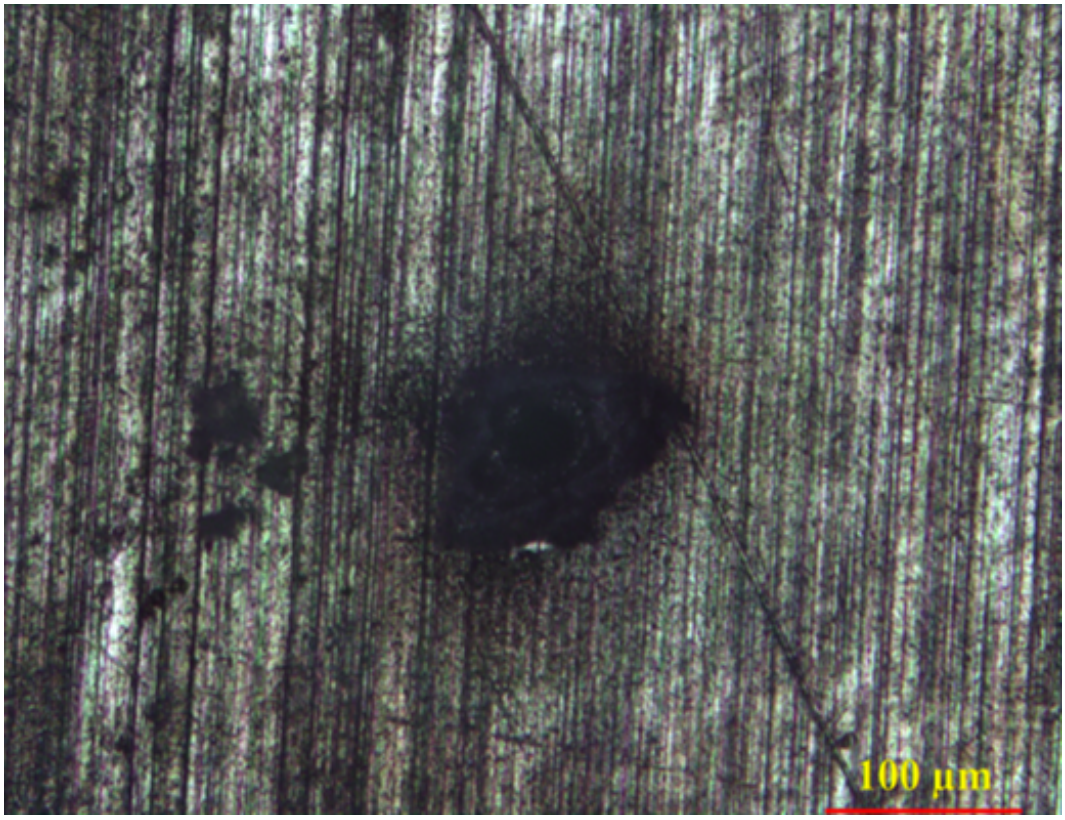

Figure 4.6: Optical micrograph of the top of an ablation crater created from 1000 pulses at 2 Hz from the picosecond laser described in Section 3.2. It can be seen that the discolouration present in Figure 4.5 is almost entirely absent.

Compared the nanosecond laser, this laser yielded smaller ablation diameter at approximately 45 µm. This small diameter implies the converse of the nanosecond laser in terms of number of measurement sites. Having a smaller ablated diameter (and volume) means that a single measurement would have a smaller chance of measuring a H/D concentration that matches the true concentration of the sample. With such a small ablated volume, it is likely that measurements would alternate from overestimating to underestimating the H/D concentration in the sample.

Additional studies were done using an Alicona Infinite Focus G5 3D Surface Measurement System to further study the ablation characteristics. This instrument allowed for a 3-dimensional reconstruction of the crater shape and depth profile. Figure 4.7 and Figure 4.8 show the results of measurements from this instrument.

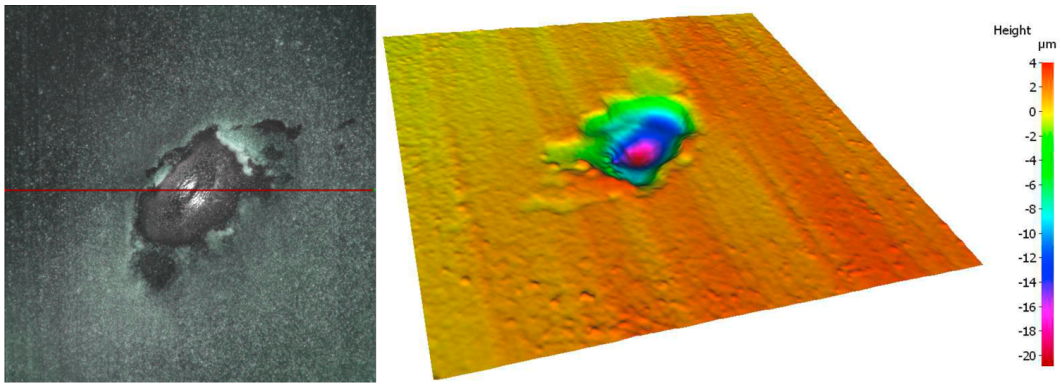

Figure 4.7: 3-dimensional colour map profile measurement of an ablation crater formed by the picosecond laser described in Section 3.2 operating at 2 Hz. The imaged ablation crater was the result of 500 pulses.

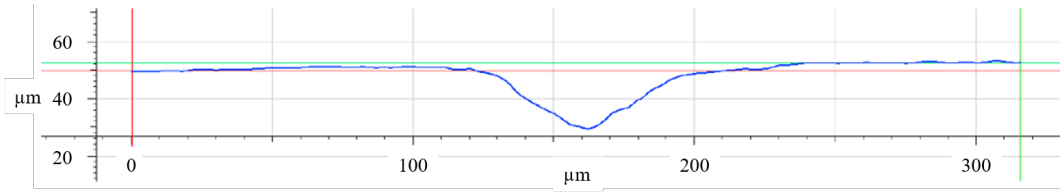

Figure 4.8: Optical profilometry measurement of an ablation crater formed by the picosecond laser described in Section 3.2 operating at 2 Hz. The imaged ablation crater was the result of 500 pulses. The red line in Figure 4.7 shows the location of the profile measurement.

Use of this instrument allowed for a determination of an ablation rate of 64 nm/pulse, with a volumetric ablation rate of approximately 102 μm^3. Laser ablation of Zr and its alloys has not been studied intensively, however, the results can be compared to

other metals. Zinc has a similar ablation threshold to that of Zr, with a value of 0.21 J/cm^2 [55]. Mustafa et al. Found the volumetric ablation rate of Zinc to be approximately 195 μm^3 with a fluence of 10 J/cm^2, using a similar pulse duration picosecond laser to that used here [55]. This rate is almost twice the rate found here for Zr-2.5%Nb. This difference could arise from the unknown properties of Zr-2.5%Nb, specifically the heat of vaporization and the optical properties, which could make the ablation threshold of Zr-2.5%Nb than the calculated threshold of pure Zr.

Further studies were done on a crater with more pulses and it was found that the ablation rate for this test was 55 nm/pulse. The difference in ablation rate follows similar trends seen in Zinc where the threshold fluence of the material increased with increasing numbers of pulses on the same location [55]. The results of the high pulse test are shown in Figure 4.9 and Figure 4.10.

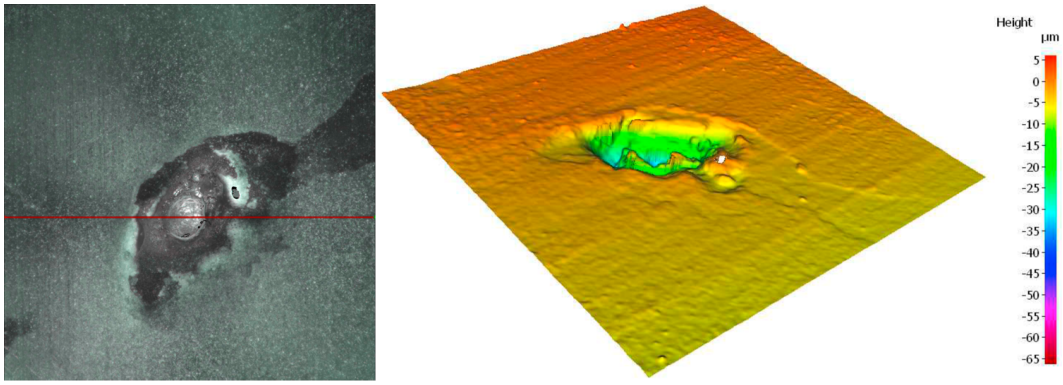

Figure 4.9: 3-dimensional colour map profile measurement of an ablation crater formed by the picosecond laser described in Section 3.2 operating at 2 Hz. The imaged ablation crater was the result of 1000 pulses.

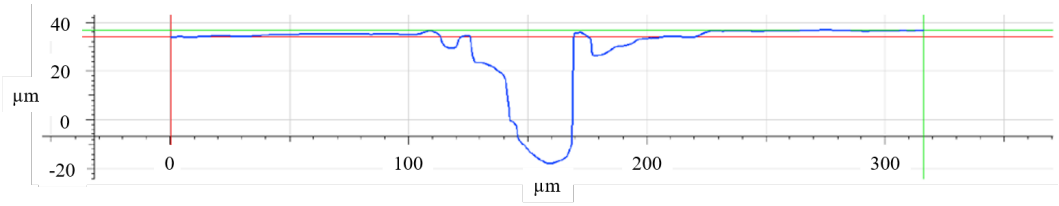

Figure 4.10: Optical profilometry measurement of an ablation crater formed by the picosecond laser described in Section 3.2 operating at 2 Hz. The imaged ablation crater was the result of 1000 pulses. The red line in Figure 4.9 shows the location of the profile measurement.

The ablation rate is quite low for both of these tests, however, it would allow for a high-fidelity 3-dimensional reconstruction of the elemental structure of the material in future works. Conversely, if a higher ablation rate is needed, a laser of higher power could be used which could then have its power lowered by use of neutral density filters if a high-fidelity study was desired.

4.2 Representative Sampling

The benefit of current scrape methods for measuring H and D concentrations is that the method collects large samples from several locations along the pressure tube's inner surface. Due to the somewhat randomly dispersed and variable-sized hydrides, methods such as scrape provide a sample with a large number of hydrides across a large volume, and hence a good average of the volumetric concentration of hydrides since the samples make up a statistically significant portion of the whole pressure tube [56]. A single sample produced from scrape methods have areas on the centimeter scale and extend hundreds of microns below the surface of the

pressure tube.

Conversely, LIBS measurement sites have diameters on the order of tens to hundreds of micrometers and ablation depths of tens to hundreds of nanometers (for a single pulse). This implies the need to consider multiple measurement locations in order to obtain a suitably large number of hydrides so as to estimate the volumetric average hydride concentration. Recognizing this issue, a program was written in MATLAB to analyze Scanning Electron Microscope (SEM) images of hydrides in Zr-2.5%Nb in order to make an estimation of how many ablation sites would be needed to make a measurement which would be representative of the entire sample. It should be noted that images used showcased only a small section of a pressure tube and were thus assumed to be representative of a normal section of a pressure tube during operation. Also, only certain H_{eff} SEM images were available. An example of the hydride images used for the program input is shown in Figure 4.11, obtained from [57].

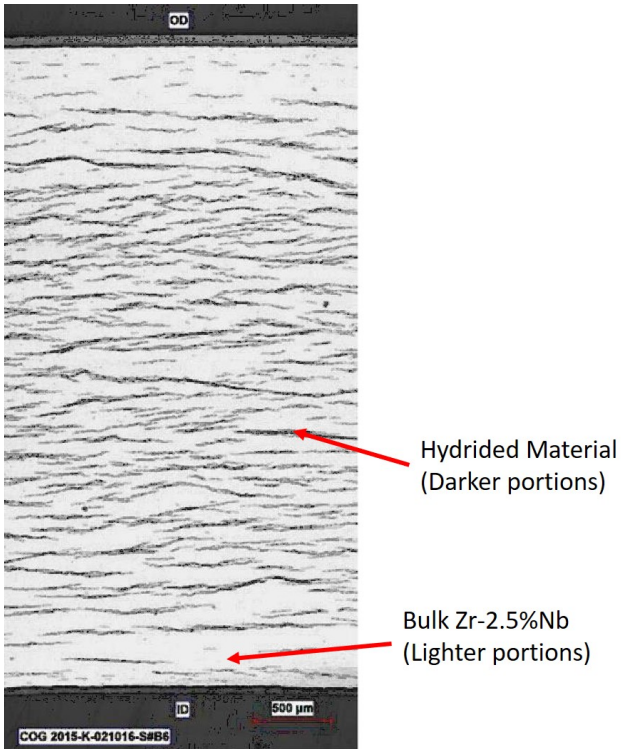

Figure 4.11: SEM image of a hydrided sample of Zr-2.5%Nb to a level of 157 ppm using the process described in Section 3.4. Figure adapted from [57].

The program first converts the images to a binary format where the hydrides show up as white spots on the image and the metal is black. An average pixel value for the image is then taken, which is used as a proxy for the average hydride content of the imaged section. The user then inputs the LIBS measurement values, such as the ablation diameter, the ablation rate (depth per pulse), and the measurement pulse. The input values are converted to pixel dimensions as the pixel size is calibrated to known dimensions in the micrograph, such as a scale bar. From these input values an ablation profile is generated which can be visualized as a rectangular section which would be cropped from the initial image. The program then simulates

the removal of the material from the pulse and extracts the percentage of hydrided material removed when compared to the total volume removed in that pulse. This yields a virtual signal where a value of 1.0 indicates the entire volume was hydrided material and a value of 0 indicates that there was no hydrided material present in the removed volume.

Since a LIBS measurement may be initiated at any location along the inner radius of the pressure tube, a random starting location is selected along the inner surface of the pressure tube image (i.e. the location where the measurement would be taken from in a real measurement) and checked to ensure that the ablation diameter would not exceed the dimensions of the image. If the location would result in a portion of the interrogation site being off of the image, the opposite side of the image is used for that exceeding area. This ensures that each sample taken encompasses the same area in the image. While randomly sampling an area is not how a real LIBS measurement would be done (rather a systematic scan would be preferable) this randomization was done as an attempt to mimic the heterogeneous distribution of hydrides in the alloy. Due to limitations on the available data, this was deemed to be an acceptable approach.

After selecting a location, an average pixel measurement is then taken within that volume and counted as the measurement in that location. Subsequent sample volumes are then taken from random initial positions on the inner surface of the pres-

sure tube and the average of these measurements is tracked. Measurements will continue until either the user defined maximum number of ablation sites is reached or the difference between the measured average and the overall average of the image drops below the user defined threshold. Figure 4.12 shows a flow diagram of what 2 measurements made by this program would look like.

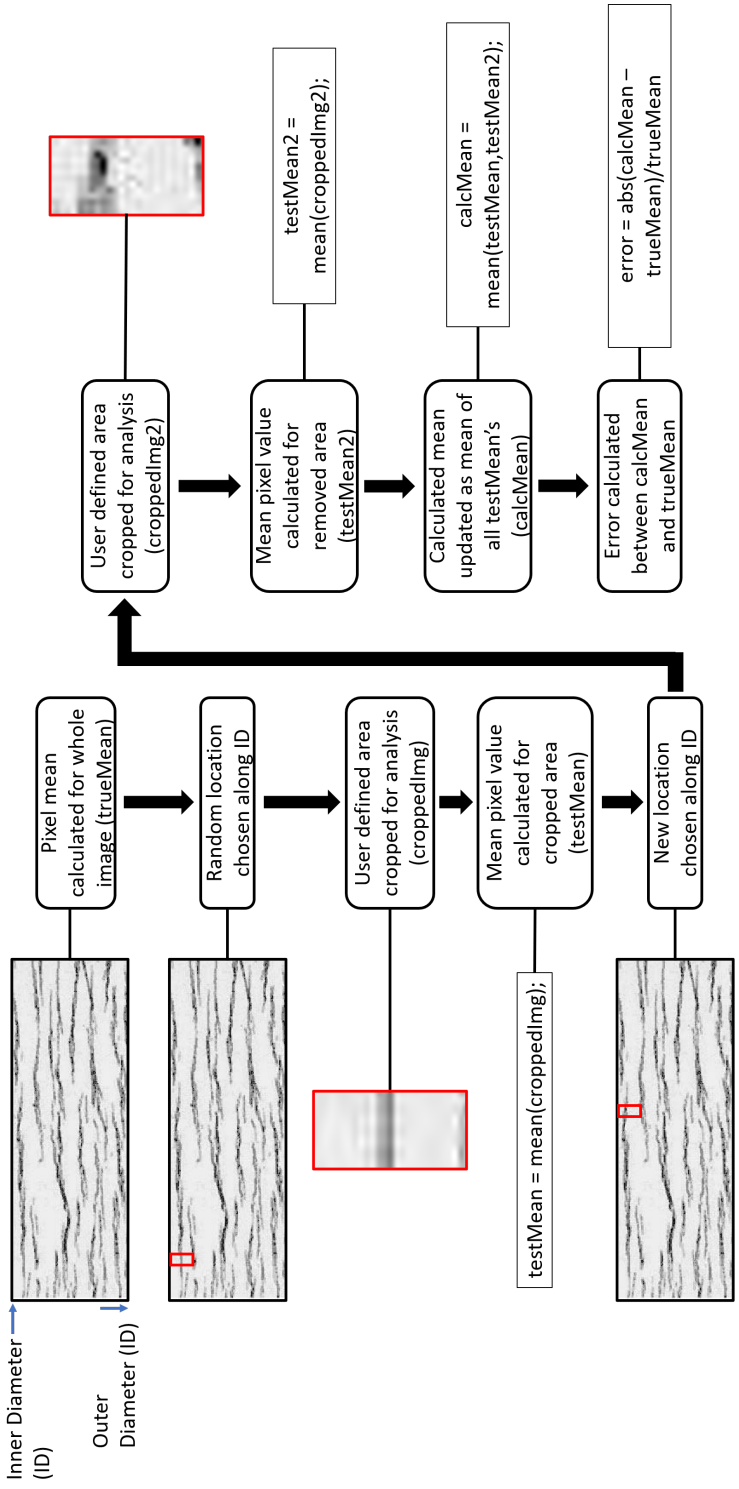

Figure 4.12: Flow chart depicting the representative sampling code. This process would be repeated either until a target difference threshold is met or until a user defined number of measurements has been made. The hydride image presented here has been adapted from [57].

Scrape methods often quote their associated errors in terms of percent error within a confidence interval (e.g. 5% error at 95% confidence). Based on the results of the sampling algorithm outlined above, one can assess the number of pulses and sites needed to be sampled with LIBS in order to achieve a comparable volumetric hydride concentration confidence interval. It was found that samples which contained a higher concentration of hydrides, indicative of pressure tubes which have been in service for longer, the number of LIBS measurement sites needed to meet a certain error threshold was lower. This result can be understood easily as the hydride population becomes more uniform and the spacing between hydrides decreases as the hydrogen concentration increases. Additionally, the error drops off rapidly as the number of measurement sites increases to 200, then continues to decrease, however, at a more gradual rate. These features can be seen in Figure 4.13 and Figure 4.14 which correspond to program runs at a 95% confidence interval and a 98% confidence interval, respectively.

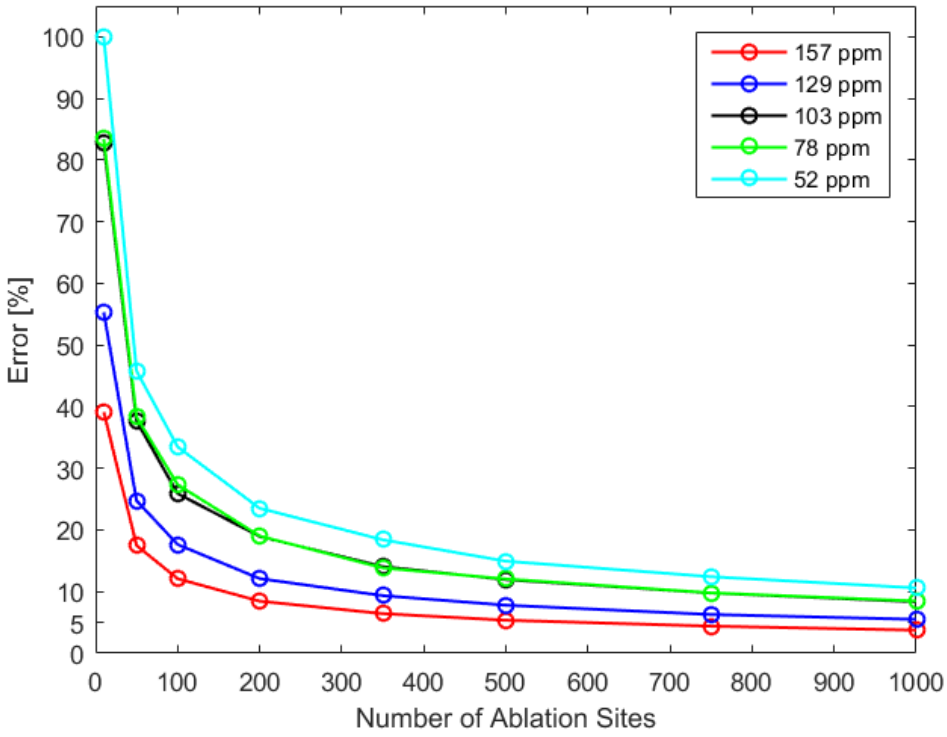

Figure 4.13: Results of the MATLAB program estimating the error associated with varying numbers of measurement sites within a 95% confidence interval. Please note that the hydrogen concentrations were based on the images that were available in literature.

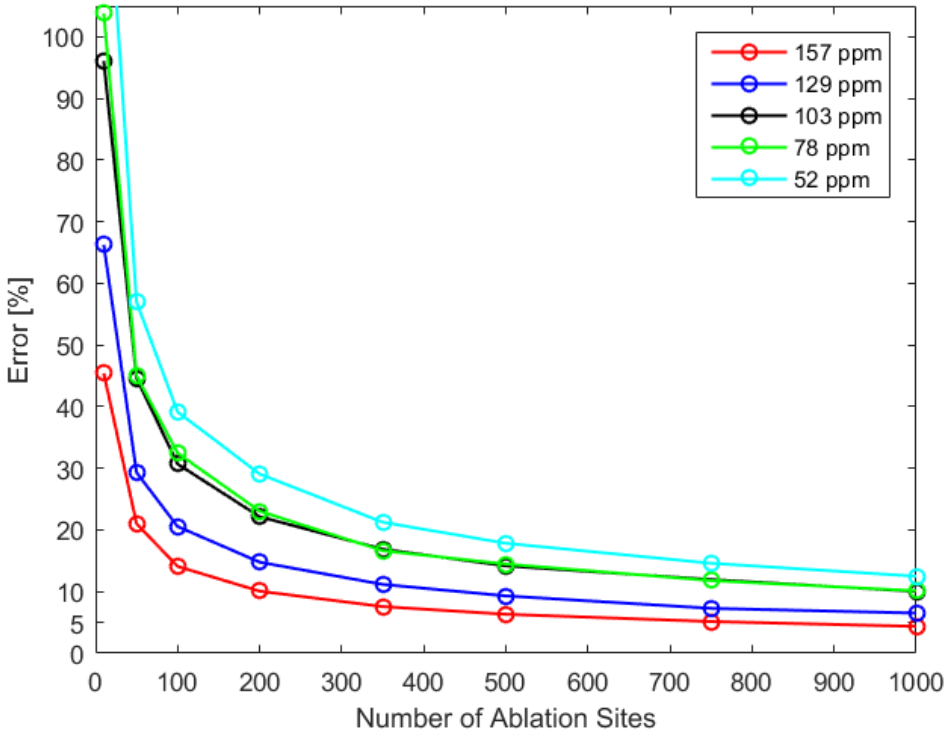

Figure 4.14: Results of the MATLAB program estimating the error associated with varying numbers of measurement sites within a 98% confidence interval. Please note that the hydrogen concentrations were based on the images that were available in literature.

Increasing the ablated diameter to a size representative of the nanosecond LIBS setup used, it can be seen that the number of measurement sites needed to reach a desired error benchmark is reduced. This is because the larger ablated volume is more representative of the entire sample. These results are shown at a 95% confidence and 98% confidence in Figure 4.15 and Figure 4.16, respectively.

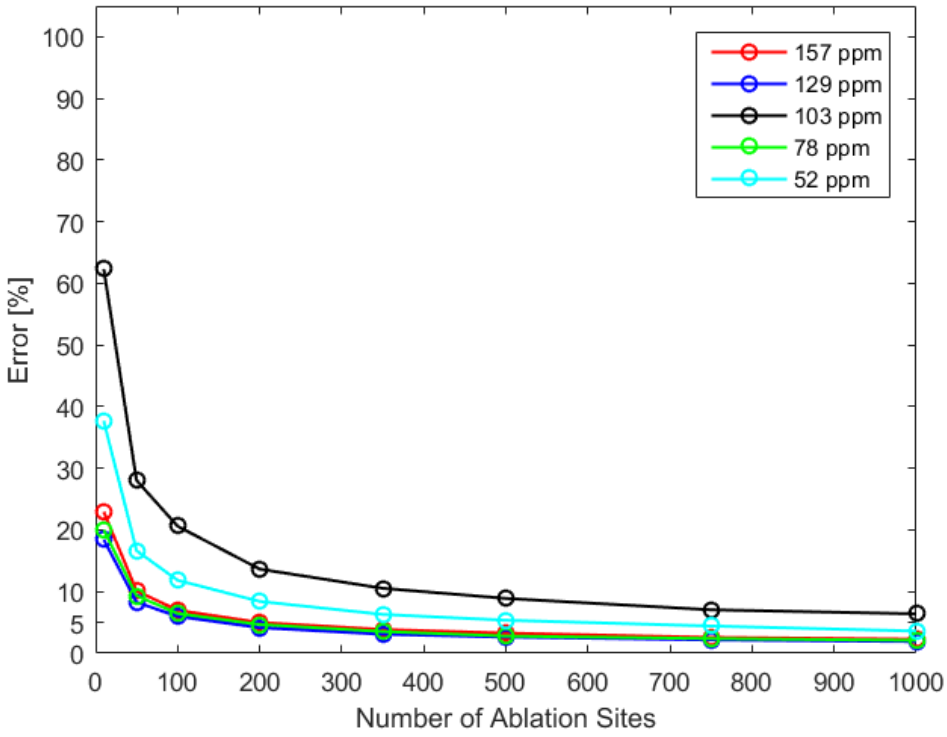

Figure 4.15: Results of the MATLAB program estimating the error associated with varying numbers of measurement sites within a 95% confidence interval using a 600 µm ablation diameter. Please note that the hydrogen concentrations were based on the images that were available in literature.

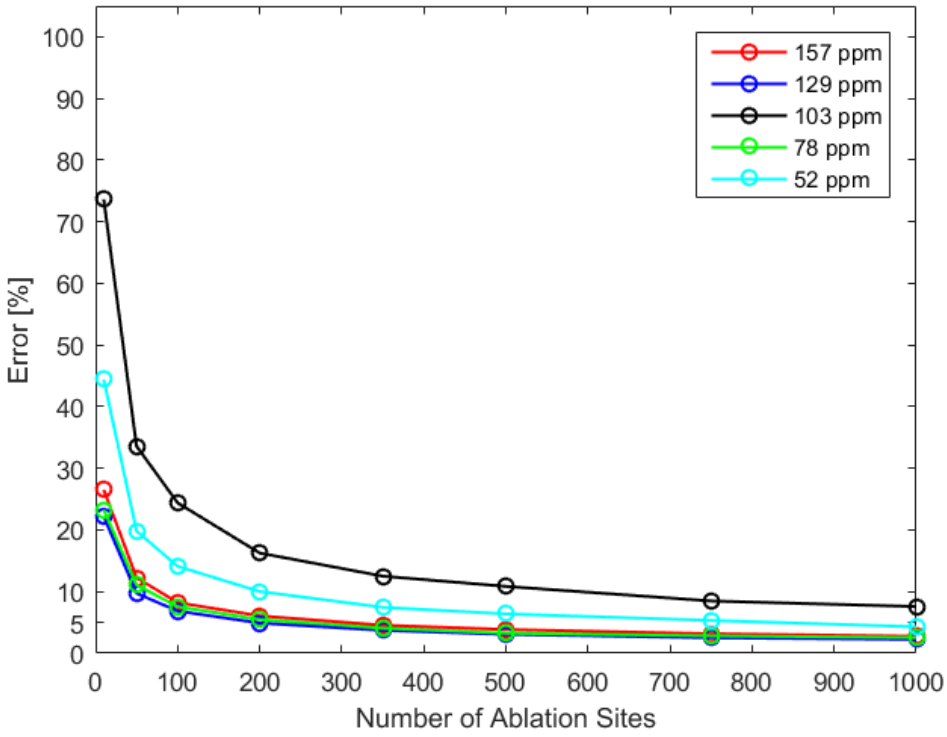

Figure 4.16: Results of the MATLAB program estimating the error associated with varying numbers of measurement sites within a 98% confidence interval using a 600 µm ablation diameter. Please note that the hydrogen concentrations were based on the images that were available in literature.

The errors associated with scrape methods and their accompanying mass spectroscopy are around 5% at a 95% confidence [7]. To match these metrics, LIBS based inspection methods would require greater than 1000 measurement sites, drilled to a depth of 150 µm, if taken with the experimental setup described in Section 3.2 due to the small ablation diameter. Larger laser energies with larger ablation volumes would require significantly less pulses and sample sites to achieve a similar accuracy. This postulate is supported by the results shown in Figures 4.13 - 4.16.

Since only a limited number of micrographs were available, the simulations above should be redone if more data becomes available, especially considering that the results can be sensitive to hydride morphology and density. Furthermore, in subsequent investigations, if the laser system changes, the simulation should be conducted again. Changing the laser energy or focusing optics will change the ablation crater dimensions. Having a laser with a higher pulse energy would allow for a larger crater diameter which would lead to fewer measurement sites being needed to obtain the same error at the same level of confidence.

4.3 LIBS Results

4.3.1 Nanosecond LIBS

Using the experimental setup described in Section 3.1, LIBS experiments were performed on pristine (as manufactured) and artificially deuterided Zr-2.5%Nb samples with 90 ppm of D. To remove surface contamination, all new interrogation sites on the samples were first subjected to 5 cleaning pulses. The primary purpose for this cleaning was to remove surface moisture as its presence would mask the signal from hydride emission if they were present near the surface.

As a primary test, a steel sample was investigated to see if the system had any bias at the wavelengths of interest. It can be seen in Figure 4.17 that no signal from H-α can be seen. The measurement was made in a He flow environment with a gate

delay of 1 µs and a gate width of 10 µs.

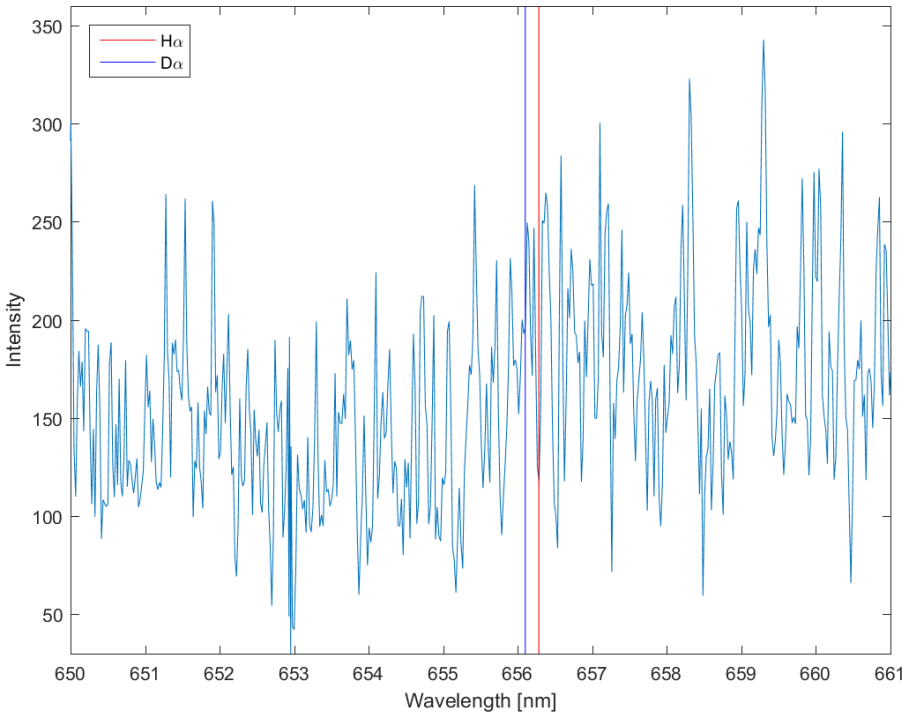

Figure 4.17: Emission around H-α on a steel sample after cleaning pulses. The blue vertical line indicates the expected location of the D-α emission line and the red vertical line indicates the expected location of the H-α emission line.

Despite Figure 4.17 simply exhibiting noise, confirmation that the system was capturing plasma emission can be confirmed by looking at a different wavelength range. Figure 4.18 shows a different wavelengths range where clear peaks can be seen.

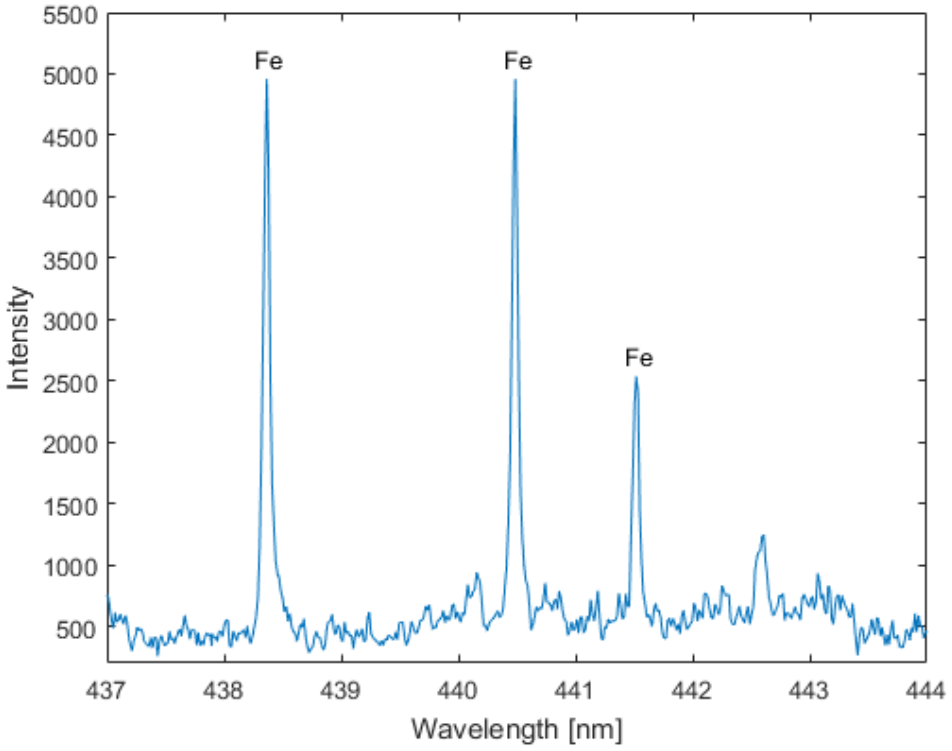

Figure 4.18: Iron (Fe) emission peaks from the same spectrum as Figure 4.17. This confirms that the system was capturing plasma emission.

Additionally, to confirm that the system's wavelength accuracy was sufficient, that is that it would not exceed the separation between H-α and D-α lines, a measurement of a tungsten-deuterium (WD) lamp was taken. In Figure 4.19 it can be seen that the spectrometer measured wavelengths very faithfully. The blue line on the figure lies along the D-α emission line, whereas the red line lies along the H-α line. The discontinuity existing in the spectrum around 653 nm is the result of the order structure of the Échelle grating.

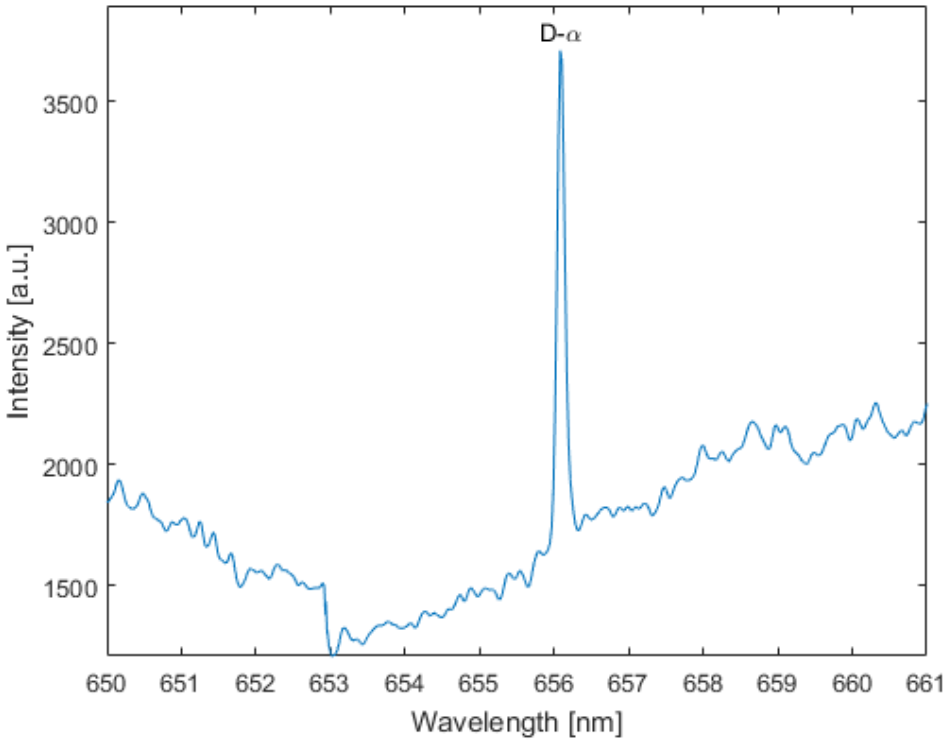

Figure 4.19: Emission of a tungsten-deuterium lamp captured by the LTB Aryelle spectrometer.

To confirm the system's ability to measure H-α emission, a damp tissue was placed on the surface of the steel sample. The ablation of the steel excited some of the water from the tissue, causing it to break into its constituent elements and emit. Thus, it is possible to observe a significant H-α signal in Figure 4.20.

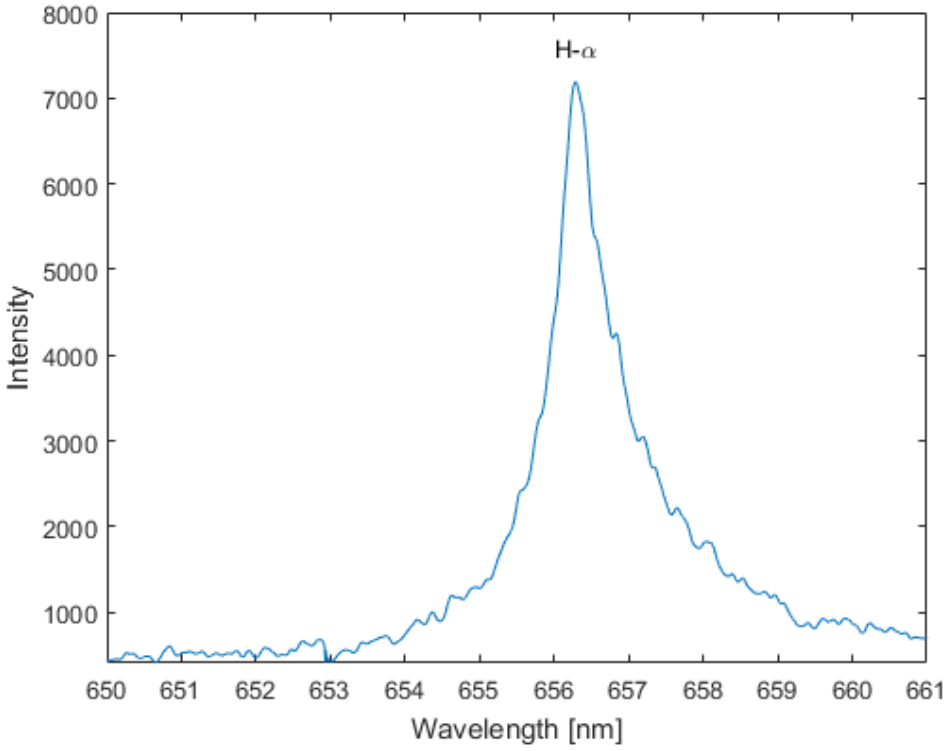

Figure 4.20: Emission around H-α on a steel sample covered with a damp tissue. No other emission lines are seen in this range as expected from Figure 4.17.

After confirming the performance of the system, various backing gases were tested to see their effect on the LIBS plasma. Using common detection parameters of a gate delay of 4 µs and a gate width of 10 µs, a sample of Zr-2.5%Nb artificially deuterided with 90 ppm of D was tested in air, Ar, and He. All of these environments were at atmospheric pressure and, in the case of Ar and He, the chamber was purged for at least 5 minutes before testing in an attempt to flush out atmospheric contaminants. Figure 4.21, Figure 4.22, and Figure 4.23 show the H-α emission line in air, Ar, and He, respectively.

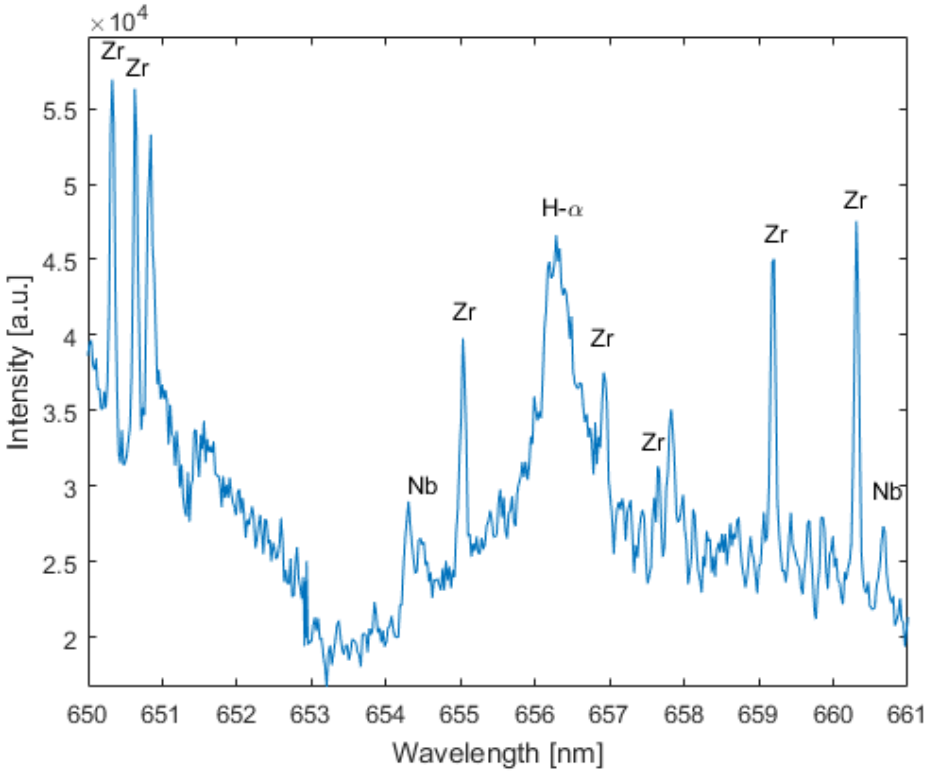

Figure 4.21: Emission from H-α in an artificially deuterided sample of Zr-2.5%Nb with 90 ppm D in air. The unlabelled emission peak at 650.9 nm was persistent for all tests conducted in an air environment. This peak's source is currently unknown and is discussed further in Appendix B.

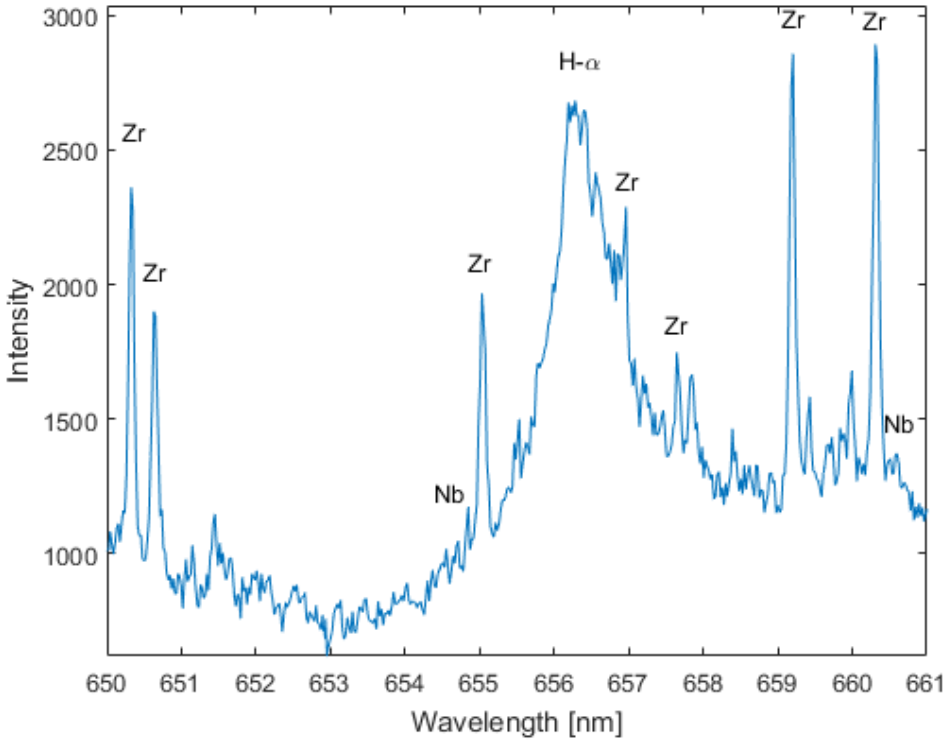

Figure 4.22: Emission from H-α in an artificially deuterided sample of Zr-2.5%Nb with 90 ppm D in an Ar flow environment at atmospheric pressure.

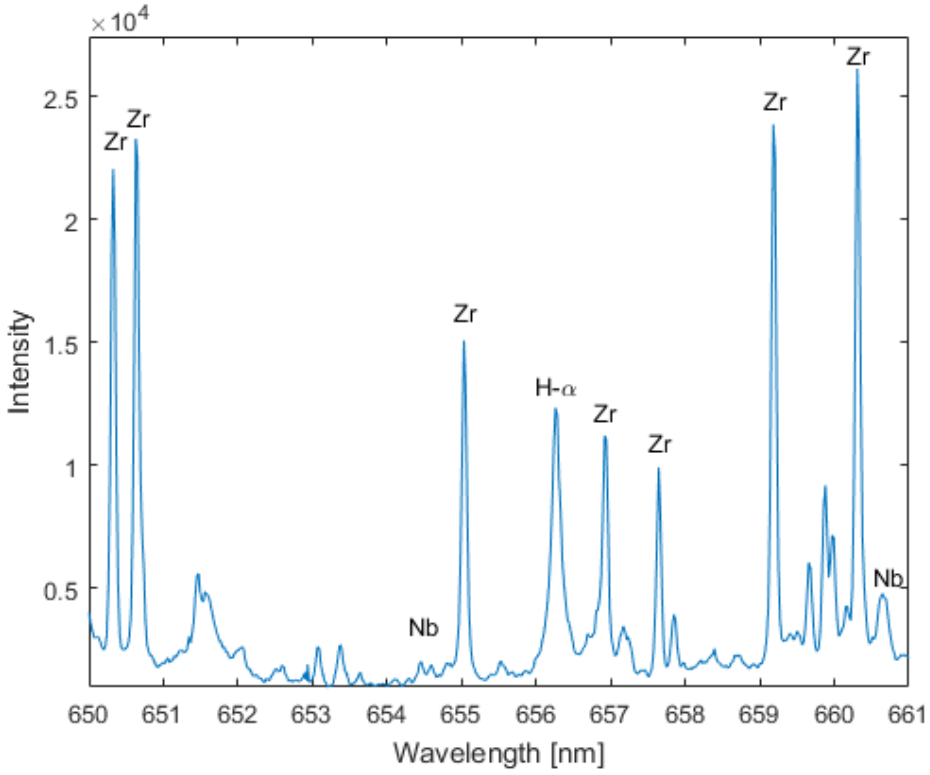

Figure 4.23: Emission from H-α in an artificially deuterided sample of Zr-2.5%Nb with 90 ppm D in a He flow environment at atmospheric pressure.

One of the most prominent differences between the above spectra is the width of the emission lines. It can be seen in Table 4.1 that He results in the narrowest emission lines. This result suggests that for discrimination of closely emitting species and atmospheric pressures, He gas should be used. Unfortunately, the experimental setup did not contain a vacuum chamber, therefore low-pressure gas environments could not be tested.

A final test was conducted on a sample of deuterided Zr-2.5%Nb in which a hole was drilled deep into the sample, by the laser, before the LIBS testing was con-

Backing Gas	H-α FWHM [nm]	Zr 655.05 nm FWHM [nm]
Air	0.39	0.09
Ar	0.42	0.1
He	0.14	0.08

Table 4.1: Linewidths (measured as FWHM) for emission profiles of interest in different gas environments

ducted. These tests were conducted in an Ar flow environment in an attempt to amplify any emission from D as much as possible. Despite these measures, a clear signal from D-α emission could not be seen, however, a persistent H-α signal was seen. This H-α signal subsided as measurements were made on the same location (i.e. deeper into the sample). Figure 4.24 shows a measurement made earlier in the experiment and Figure 4.25 shows a measurement made deeper into the sample.

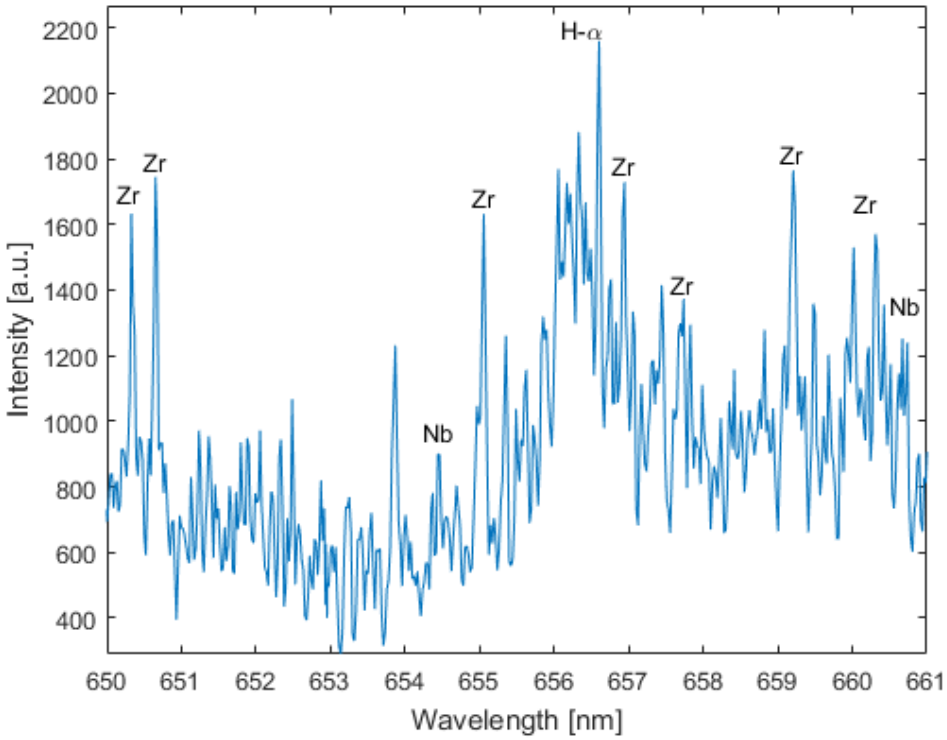

Figure 4.24: Spectrum captured from a LIBS measurement in a pre-drilled hole on a deuterided Zr-2.5%Nb samples with 90 ppm D.

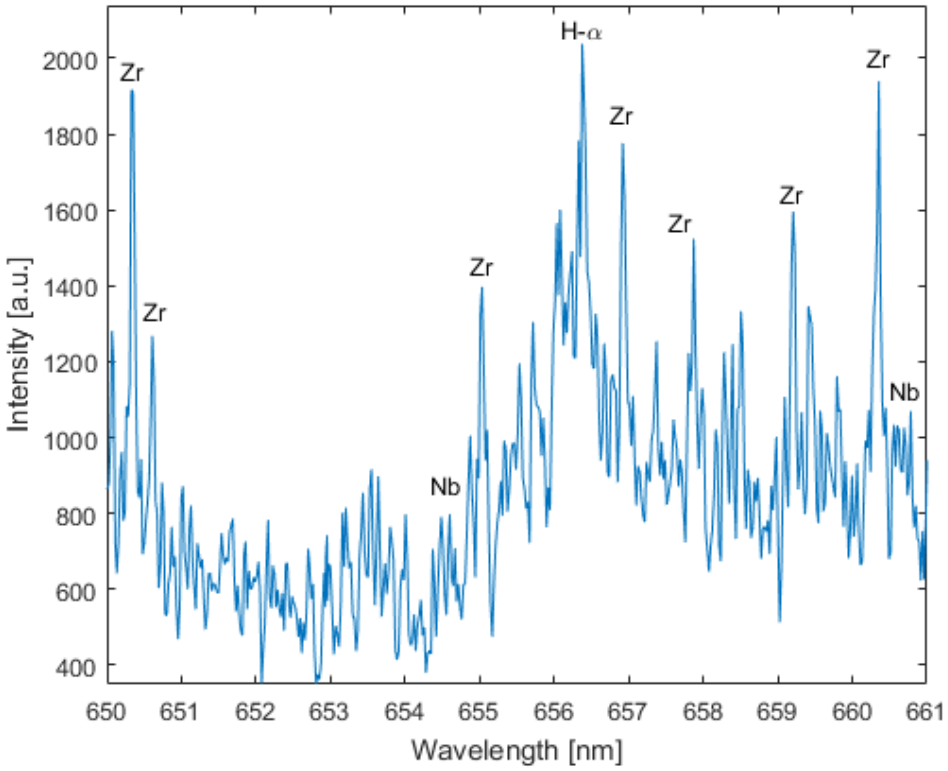

Figure 4.25: Spectrum captured from a LIBS measurement in the same pre-drilled hole as Figure 4.24. This measurement was made deeper in the hole, however.

The intensity of the H-α emission can be seen to fall off between the two spectra. A possible explanation to this result is sample contamination. If H somehow was able to interact with the sample, it would be expected that higher concentrations would exist closer to the surface and tail off deeper into the sample; assuming the sample was not annealed after this exposure. Additionally, hydrided material could have been present in the cleaning pulses, drilling, or first measurements which then redeposited into the measurement site. Chamber contamination is unlikely, as in the spectrum taken on steel in Figure 4.17, no H-α signal can be seen. The true source

of the H-α emission signal in these spectra remain anomalous at this point.

A final check was performed to smooth out some of the noise by averaging the single pulse spectra collected during this experiment. Those results are shown in Figure 4.26 where 10 sequential measurements are averaged and in Figure 4.27 where 50 sequential measurements are averaged.

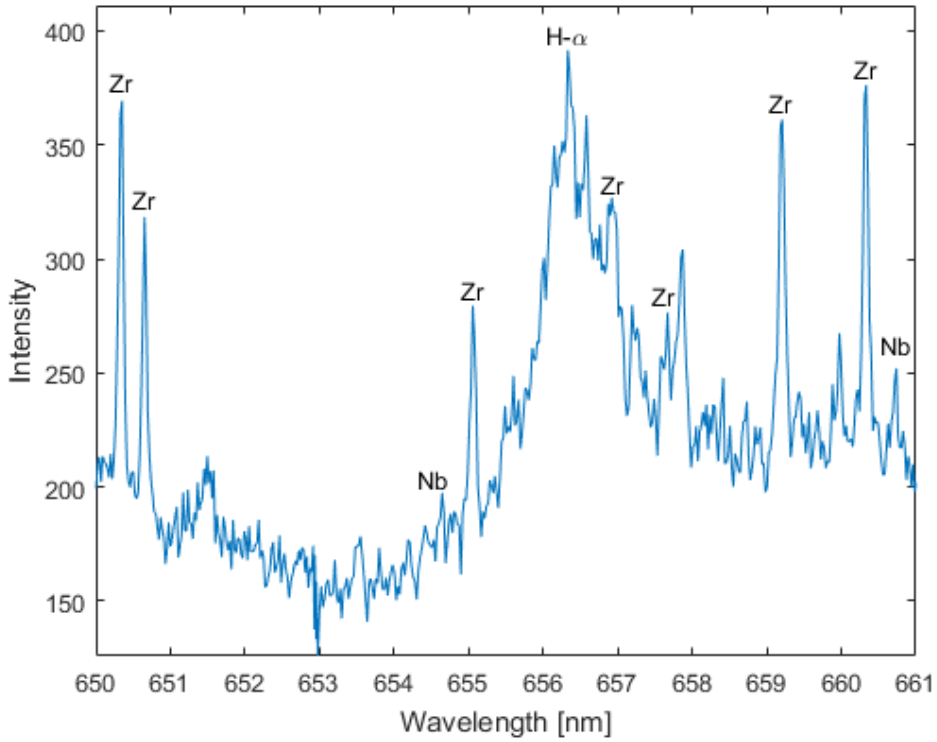

Figure 4.26: Averaged spectrum from 10 sequential measurements made on the same location of a deuterided Zr-2.5%Nb samples with 90 ppm D. The measurement site was pre-drilled with the laser to a significant depth before performing these measurements.

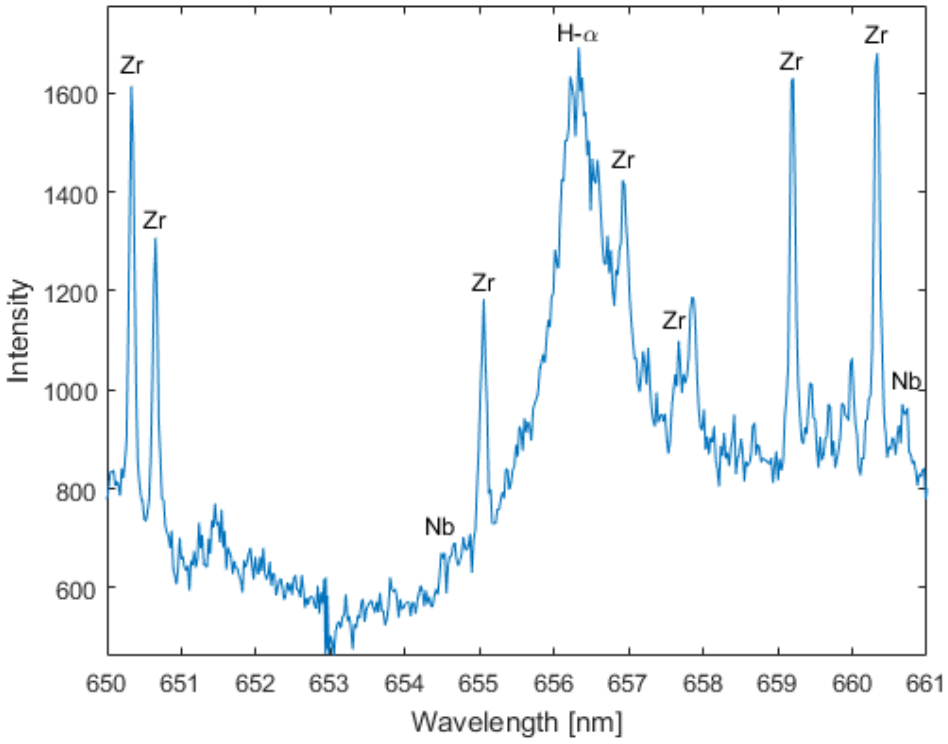

Figure 4.27: Averaged spectrum from 10 sequential measurements made on the same location of a deuterided Zr-2.5%Nb samples with 90 ppm D. This average was made from the same measurement location as the measurements shown in Figure 4.26.

Despite the inability to detect D emission from the samples, a hopeful result was found with regards to the sensitivity or Limit of Detection (LOD) for this LIBS system. A CANDU operating utility provided mass spectroscopy results of a typical pressure tube sample, similar to the pristine sample tested here, which measured all of the known contaminants within the alloy material. Of all of the potential species which exist, only uranium and boron were not successfully measured in the LIBS spectra. Table 4.2 contains a list of the expected species in the pressure tube sample

and the most dominant emission line that was visible within the spectra. Spectral emission lines were obtained from NIST [58]. The emission lines chosen for presentation were based on a clear definition of the emission peak and a relatively clear environment (i.e. as few nearby emission peaks from competing species).

Element	Measured Concentration [ppm]	Observed Emission Line [nm]
Al	31	237.312
B	0.2	N/A
C	67	600.113
Cd	0.2	340.365
Co	10	338.817
Cr	100	449.686
Cu	25	620.413
Fe	442	519.154
Hf	39	281.894
Mg	10	284.828
Mn	25	421.184
Mo	25	519.144
Ni	35	337.464
Pb	25	357.273
Si	25	298.765
Sn	25	365.578
Ta	59	269.830
Ti	25	395.821
U	1	N/A
V	25	419.156
W	25	414.907

Table 4.2: Contaminant species present in Zr-2.5%Nb pressure tube material as measured by mass spectroscopy and LIBS. Note that an emission wavelength of N/A means that species was not measurable with LIBS.

The most encouraging measurement from the results shown in Table 4.2 is the signature of Cd in the spectra. The concentration, 0.2 ppm, is well below the minimum expected detection limit for a future LIBS system for investigating the emission of

H and D from Zr-2.5%Nb. It should be noted that the emission properties of Cd and H and D are different, therefore it is expected that the LOD for the two species would be different. Figure 4.28 shows the persistent emission line from Cd which was present in many of the spectra captured.

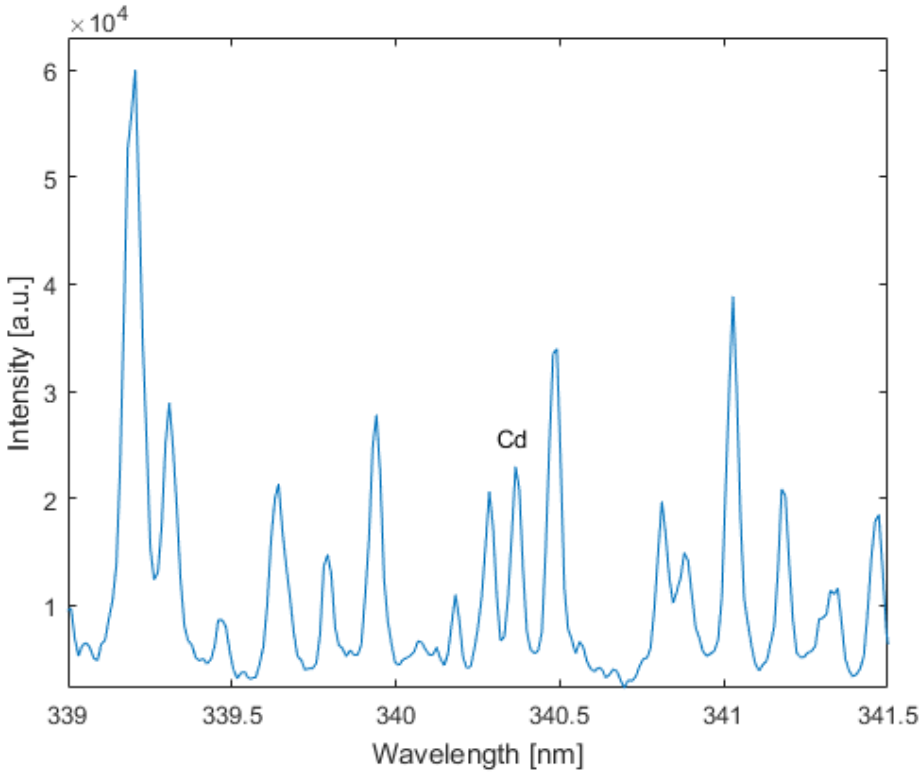

Figure 4.28: Part of the emission spectrum from a Zr-2.5%Nb sample around the 340.365 nm emission line of Cd. The red line superimposed on the image highlights the emission line reported by NIST in [58].

While the nanosecond LIBS system was incapable of measuring emission from the D of ZrD, the ability to measure parts per billion (ppb) levels of Cd is encouraging. However, this result raises questions as to why ppm levels of D could not be seen in the spectra. The lack of D emission may have been due to the lack of a vacuum

environment. As will be shown in Section 4.3.2, distinct H and D emission could only be seen when the measurement was performed in a vacuum environment. Such testing was outside of the scope for this thesis, but can be explored in subsequent works.

4.3.2 Picosecond LIBS

For picosecond LIBS, a preliminary setup at atmospheric pressure and a final vacuum-based system were studied. The optical setup was consistent for both systems and was comprised of a 100 mm focal length best-form lens (Thorlabs LBF254-100-C) focusing the laser onto the surface of the sample. Plasma emission was captured with a 600 μm core optical fibre delivering the light directly into the Princeton Instruments Isoplane SCT320 spectrometer. The spectrometer was setup with a 10 μm slit width and a 1800 grooves/mm diffraction grating, giving a resolution of 35.1 pm.

For ease of setup, preliminary experiments were conducted on samples in ambient air conditions. It was found that this environment does not allow for the observation of H-α or D-α emission from samples. Samples with no additional hydriding/deuteriding, artificially deuterided samples, and zirconium foils with extremely high concentrations of deuterium were all tested in atmosphere with no detection of H or D emission. Figure 4.29 shows a typical spectrum captured in atmosphere.

This spectrum is the result of averaging 50 individual spectra captured at a 500 ns gate delay and a 500 ns gate width on an artificially deuterided Zr-2.5%Nb sample with a D content of 90 ppm.

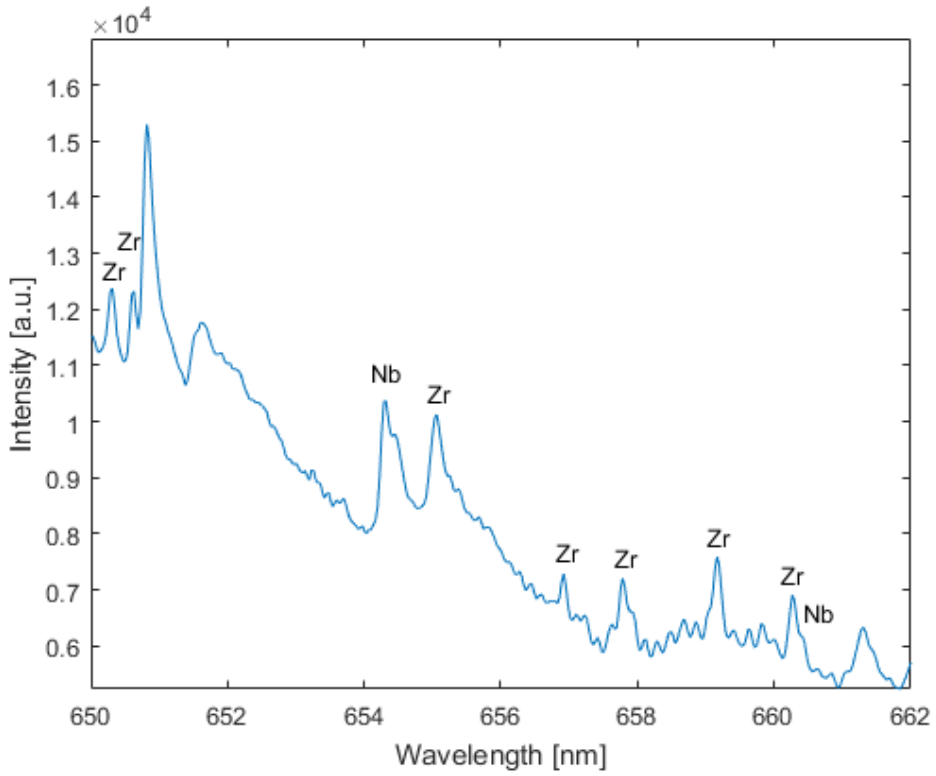

Figure 4.29: Spectrum captured from an artificially deuterided Zr-2.5%Nb sample with 90 ppm D in air. Despite the high level of artificial deuteriding, no signal from D can be seen in this spectrum.

After confirming the inability to perform the desired measurements in atmosphere, the sample and capture optics were moved into the vacuum chamber described in Section 3.3. It was found that good measurements could be made at pressures below 1 Torr with little improvement beyond that pressure. As such, the chamber pressure was held at 700 mTorr during testing to give a sufficient buffer for pressure increases

during testing.

It should be stated that due to limited equipment availability and limited access inside the vacuum chamber, the peak intensity varied between samples as it was difficult to maintain the exact collection fibre location. Due to the pump-down procedure, it was time consuming recognize the intensity discrepancy, reopen the chamber, realign the optics, then repeat the pump-down procedure multiple times. This resulted in the SNR varying between samples, however, it was deemed to be acceptable in each of the tests conducted and if it was not, the chamber was opened and the optics realigned.

Using a Zr-2.5%Nb sample with no additional hydriding as a benchmark, it was clear that there was no D-α emission, as expected. However, H-α emission could be seen from the sample. Emission from H can be expected for two reasons; firstly, it is known that Zr-2.5%Nb has approximately 5 - 10 ppm H_{eff}, in the form of ZrH, from the manufacturing process, and secondly, contamination of the sample likely occurred due to exposure to ambient environments. Additionally, interaction with skin was limited, however, handling by uncovered skin could have resulted in the transfer of oils to the sample. This result is shown in Figure 4.30 as the average of 50 spectra. The gate delay and gate width were both set to 500 ns.

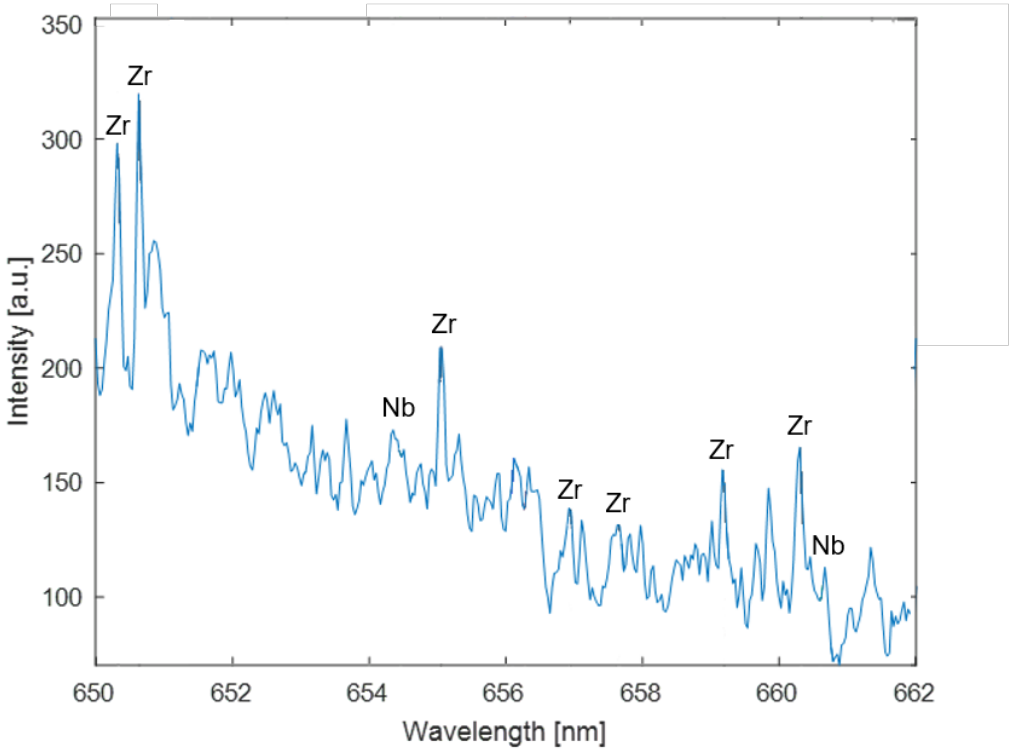

Figure 4.30: Part of the emission spectrum from a pristine Zr-2.5%Nb sample near the H-α emission line. No significant H or D signal can be seen, however, all other Zr and Nb lines in the region can be seen.

A sample with 90 ppm D artificially introduced by the process described in Section 3.4 was then tested. Prior to testing this sample, 1.5 mm of material were removed from the surface to ensure that spectra would be taken from the bulk of the material. From various metallographs, it is clear that the distribution of deuterides/hydrides becomes more consistent in the bulk of the material.

During the measurements, each individual spectrum was analyzed since it is expected that some ablation plasmas would contain hydrides while others may not

due to the heterogeneity of the hydride distribution in the alloy. Depending on the pulse and spectrum considered, peaks were clearly identified at 656.1 nm, indicative of D-α emission. As expected, other spectra would show no significant D-α signal due to the heterogeneity of ZrD dispersed throughout the sample. Figure 4.31 shows an example spectra of a single pulse hitting a deuteride in the bulk of the material. In contrast, Figure 4.32 shows an example spectra of a single pulse hitting only Zr-2.5%Nb. The gate delay and gate width were both set to 500 ns for these measurements.

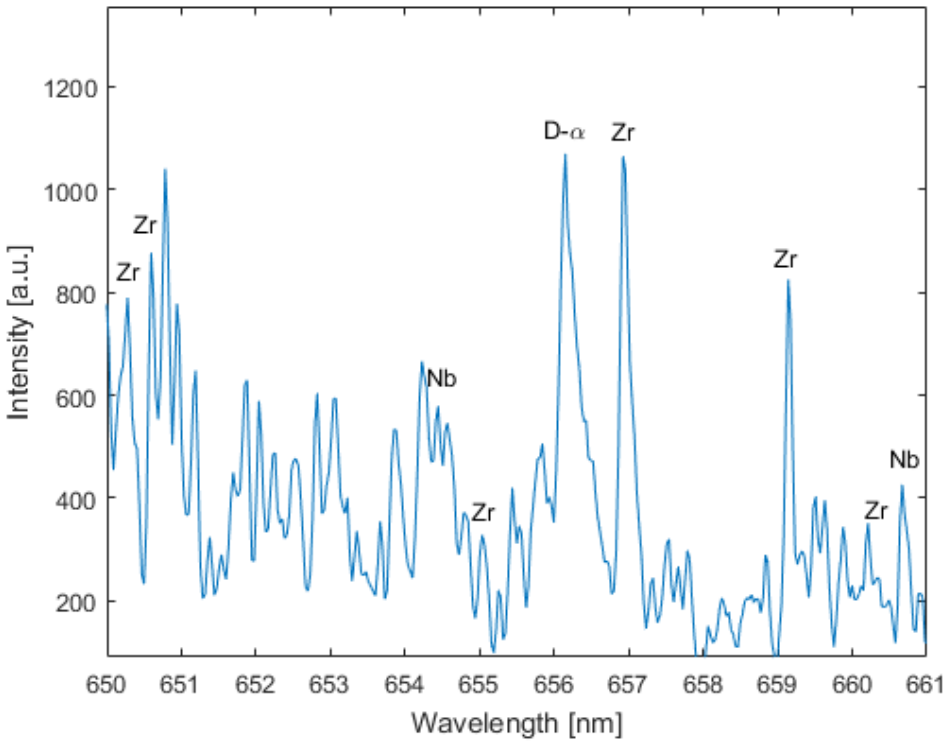

Figure 4.31: Part of the emission spectrum from a 90 ppm deuterided Zr-2.5%Nb sample near the H-α emission line. From this single pulse spectrum, D-α emission can be seen.

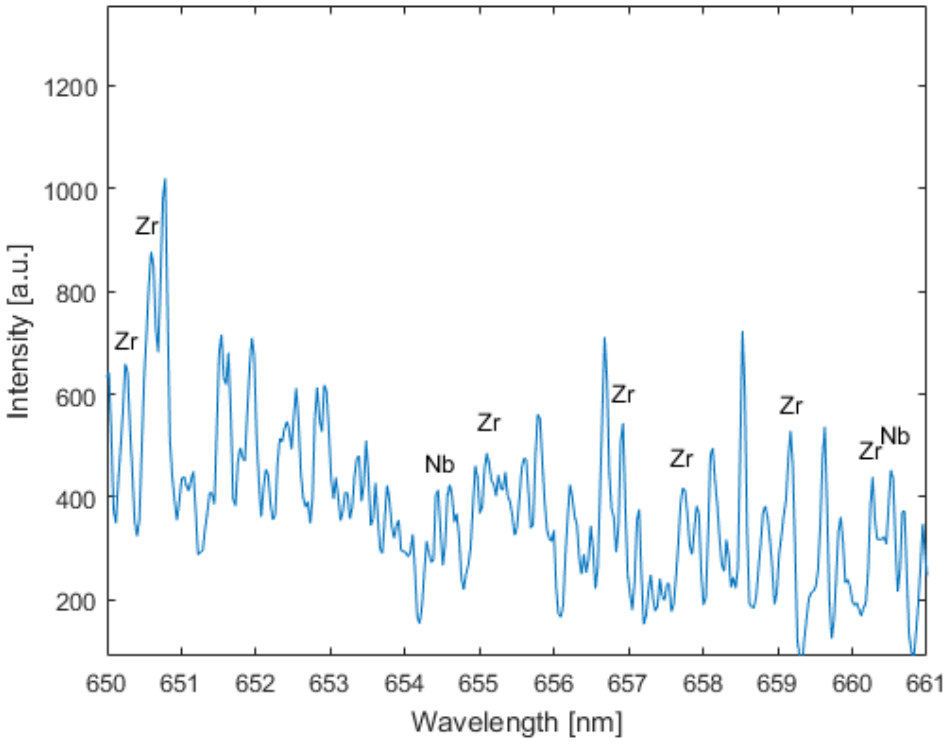

Figure 4.32: Part of the emission spectrum from a 90 ppm deuterided Zr-2.5%Nb sample near the H-α emission line. From this single pulse spectrum, no significant D-α emission can be seen indicating that ZrD was not hit in this spectrum.

To obtain a better understanding of the larger-scale distribution of deuterium throughout the sample, averaging was performed over sets of 50 individual spectra. For these averaging measurements, spectra were all captured from the sample location on the sample such that the average would be indicative of a single hole drilled into the sample. Figure 4.33 and Figure 4.34 show the results of averaging 10 and 50 spectra, respectively. The gate delay and gate width were both set to 500 ns for capture of the individual spectra.

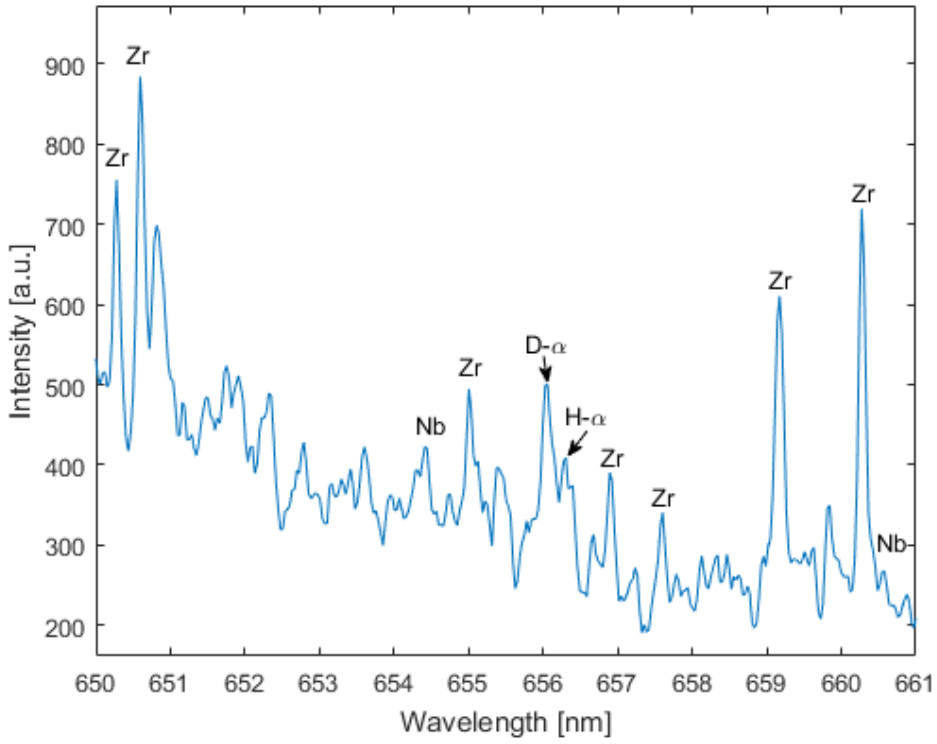

Figure 4.33: Part of the emission spectrum from the average of 10 spectra from a 90 ppm deuterided Zr-2.5%Nb sample near the H-α emission line. Both emission from D and H can be seen in the broad, double peak.

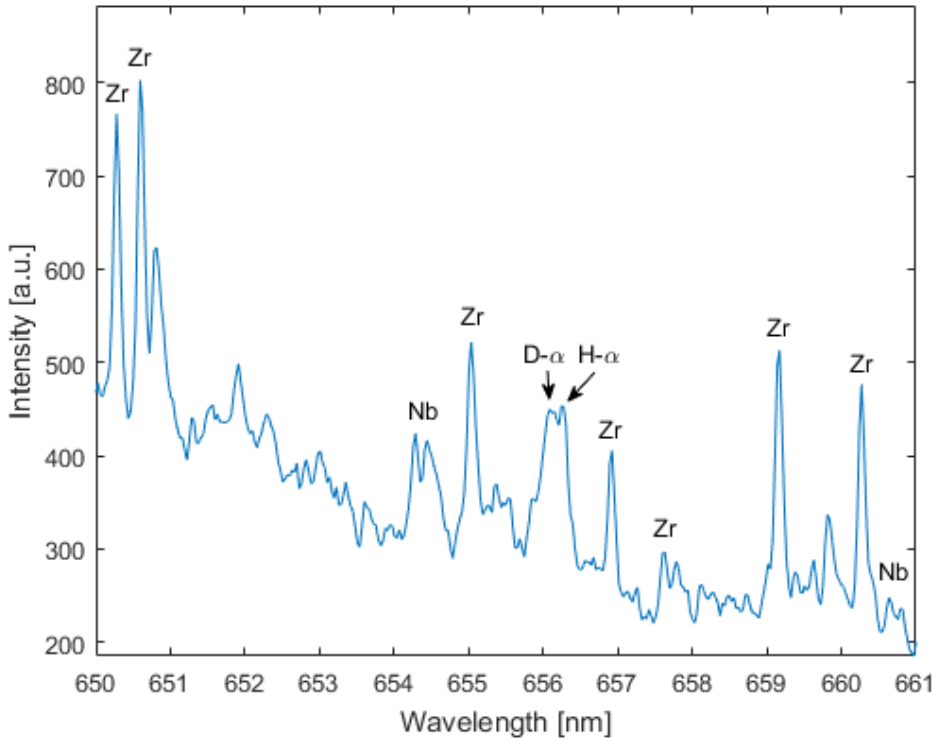

Figure 4.34: Part of the emission spectrum from the average of 50 spectra from a 90 ppm deuterided Zr-2.5%Nb sample near the H-α emission line. Both emission from D and H can be seen in the broad, double peak.

These results show that it is possible to measure realistic concentrations of deuterium in Zr-2.5%Nb samples. Furthermore, it shows that it is possible to measure deuterium in the bulk of materials rather than surface concentrations as discussed in Chapter 2: Literature Review. These results suggest that LIBS may be developed as a tool for nuclear fuel channel inspections, however, there is still significant work to be completed before implementation.

During the course of the picosecond LIBS experimentation, it was found that there

was a fairly significant dependence of the emission intensity of the location of the focusing and collection optics. The optical setup was not ideal and resulted in the need to reject spectra if they did not exhibit clear emission lines. This setup required that the optics, more often the collection optics, needed to be readjusted frequently, meaning that comparison between different sets of spectra was difficult. A more robust optical setup would be ideal for future experimentation, as discussed in Chapter 6: Future Work, and would be necessary for an accurate comparison of emission intensities and H/D concentrations between samples.

One of the issues which needs to be explored further is the intensity of the H-α and D-α emission peaks. According to [58], the emission properties of H and D are very similar which implies that in the deuterided Zr-2.5$\%$Nb samples, the D-α peak should have been significantly higher that the H-α peak. Further investigations into this discrepancy should be pursued. Additional work required before deployment of a LIBS inspection tool can occur is discussed in Chapter 6: Future Work.

5 CONCLUSIONS

5.1 LIBS

It has been shown that low concentrations of H and D present in Zr-2.5%Nb in the form of ZrH and ZrD can be detected simultaneously using LIBS, however, detection required careful alignment of collection optics, a high-resolution, gated spectrometer, and a vacuum environment. It has furthermore been shown that it is possible to see the emission signature from H and D from the bulk of the material, rather than surface concentrations. These results support the further development of a LIBS-based fuel channel inspection tool for in situ measurements of the H and D concentrations in CANDU pressure tubes.

A relatively low-powered picosecond pulsed laser was used in the LIBS setup delivering 160 μJ at 1064 nm in an 8 ps pulse. The plasma emission was captured by optical fibres which guided the light into a Princeton Instruments Isoplane SCT 320 spectrometer with an 1800 grooves/mm diffraction grating and a 10 μm entrance slit. The ablation and plasma generation took place in a vacuum chamber with an air environment at 700 mTorr. It was found that detection of D emission was not possible in an atmospheric environment, however, D-α emission was seen in the

vacuum environment.

A Monte Carlo algorithm was also developed to determine the number of LIBS measurement sites that would be needed in order to make a measurement that would be representative of the entire area of interest during an inspection. Since the H and D are not homogeneously spread throughout the alloy, multiple measurements would be needed to accurately understand the entire environment. It was found that several hundred measurement sites would be needed, based on the metallographs which were available for study. Due to the speed of LIBS measurements, this result is not discouraging to the ability of a LIBS-based measurement tool for in situ H_{eff} measurements in a CANDU reactor.

5.2 Ablation

As expected, it was found that nanosecond laser ablation of Zr-2.5%Nb underwent similar ablation mechanisms as other metals. Evidence of thermal ablation was seen using 3-D profilometry and optical microscopy. Namely, evidence of melting and the formation of a corona were easily seen on multiple samples and under various ablation conditions. Furthermore, the ablation rate of Zr-2.5%Nb was found to be approximately 100 nm/pulse when subjected to a 10 ns, 100 mJ pulse at 1064 nm with an ablation diameter of 623 μm.

When subjected to picosecond ablation, the ablation was seen to be largely non-thermal. Slight evidence of melting could be seen at the bottom of ablation craters,

however, no corona formation was present. Additionally, the ablation crater was found to make a conical shape, consistent with studies of other metals. Finally, the ablation rate of Zr-2.5%Nb was found to be approximately 64 nm/pulse when subjected to an 8 ps, 160 μJ pulse at 1064 nm with an ablation diameter of 40 μm.

5.3 Continuing Issues

Certain anomalies still exist at the end of this experimentation and could be the subject of further investigation. Firstly, the inability of the nanosecond LIBS system to measure emission from D is puzzling. Re-testing this system on different days using different samples could not resolve the issue. However, as discussed, it may simply be the need for vacuum environment in order to measure D-α emission. H emission was detected consistently with this system, however, the persistent signal remains confusing in tests where one would expect strong D emission.

Another possible solution to these issues could have been the gating parameters used. In the nanosecond LIBS setup, gate delays of 1, 4, and 7 μs with a gate width of 10 μs were used. However, it was found that in the picosecond LIBS setup that a 500 ns gate delay and 500 ns gate width were needed in order to make a consistent measurement of the D-α emission line. These systems have fundamental differences in their ablation and plasma properties, however, the vast difference in parameters suggests that the nanosecond LIBS gating parameters may not have been ideal for the detection of D.

In summation, LIBS has been proven to be capable of measuring relatively low concentrations of D embedded in Zr-2.5%Nb. This result supports the continued development of a LIBS inspection tool for use in the nuclear industry. However, there are several more tests which should be conducted. These further tests are discussed in the following chapter, Chapter 6: Future Work.

6 FUTURE WORK

Before deploying this technology in a nuclear reactor, further steps must be taken to ensure the system's ability to perform the required measurements.

6.1 LIBS

A further complement of LIBS studies should be conducted on a wide range of samples with varying H and D concentrations which would be within the expected operational concentrations. From this sample set, a calibration curve could be defined which would allow for a series of measurements to provide an estimate of the H and D concentration of any given Zr-2.5%Nb sample. Further work would also be needed in developing an in situ calibration method. Potential options include designing a system capable of measuring the electron temperature and density so that a CF-LIBS system could be employed, carrying a sample of known concentration to the measurement location and capturing a reference spectrum from this sample before testing the pressure tube, or comparing to a reference sample before and after performing the in situ inspection.

Additional work should also be conducted into confirming the estimates of the program written to determine the number of interrogation sites needed to obtain a rep-

resentative measurement of the entire pressure tube. This program was discussed in Section 4.2. It is possible that re-deposition of ablated material may influence the measured concentrations of various species which would change the number of required interrogation sites to make an accurate measurement. This effect may also change the required measurement depth of the system.

Furthermore, if the equipment becomes available, testing using more advanced LIBS techniques should be explored. Li et al. compiled various methods for LIBS signal enhancement mechanisms [59]. It is likely that a double-pulsed LIBS (DP-LIBS) setup will enhance signal emission and may result in a larger distinction between the emission lines of H-α and D-α. If it fails to enhance the distinction between the emission lines, it may simply help to accentuate the signal strength coming from low-concentration samples.

In addition to DP-LIBS, using a different lens system may help to improve the representative sampling of the system. For example, Cremers and his colleagues have shown that using a cylindrical lens to focus the laser into a line rather than a point can help to increase the sampling area and ease the process of sampling a large area [60, 61]. Such a method would help to increase the chance of a single pulse hitting a hydride and may help to decrease the number of measurement sites needed to reach a desired error threshold.

Another interesting concept which has not been explored, or at least not published,

in the field would be incorporating an integrating sphere into the collection optics of a LIBS experiment. These devices are designed to capture diffuse emission and focus it onto a single point for capture with an optical fibre. Assuming the sphere had an input port through which the incident laser could be focused onto the target sample, the diffuse plasma emission generated from a LIBS experiment could be captured more effectively using the integrating sphere. This method would also help to limit the imaging angle bias which sometimes impacts measurement results. However, with such a device care would be needed to avoid coating the inside with material ejected from the interrogation site which may reduce the reflectance of the sphere.

Development of an ideal vacuum chamber for LIBS experimentation should be pursued. Elements such as the ability to flood the chamber with various backing gases would help to identify the idyllic conditions for the discrimination of emission from H and D. The incorporation of a load-lock system and heating system would also help to eliminate atmospheric contamination in the chamber, ensuring that every peak of the emission spectrum could be identified.

Within the vacuum chamber, an automated stage would help to conduct more accurate studies to confirm the estimates of the representative sampling software. Such a stage would allow for a user defined path which could automate the lens-to-sample distance to ensure the ideal focal point location in the sample. Additionally, it

would allow for a test path to be setup to perform LIBS within a defined region with a higher degree of positional accuracy than could be obtained by a manual stage.

Finally, future experiments should examine the ability of using Laser Ablation Molecular Isotopic Spectroscopy (LAMIS) for helping to distinguish between H and D [62]. At the time of this experimentation, there were not any catalogued molecular spectra that could have been of use. Future work using buffer gases may be able to form molecules with released H and D from the material which would help with their identification.

6.2 Optical Elements

If this method were to be used for in situ measurements of the concentrations of H and D, the incident laser light and collected emission would need to be transmitted by optical fibres. However, the sending fibre would need to be able to carry extremely high energy which would exceed the fluence limit of most conventional optical fibres. An investigation into different fibre compositions and core sizes would need to be completed or an exploration into the use of silver-coated hollow-core optical fibres could be conducted.

Specific to the operational environment of a nuclear reactor, an investigation into the effects of various types of radiation on the components of this system must be conducted. It could be assumed that the laser, spectrometer, and control electronics

for this system would be kept sufficiently far away from the reactor core as to not receive a large radiation dose. Certain components, however, would not be able to benefit from this lower dose environment. Specifically, optical elements, such as mirrors and lenses, and optical fibres would need to be studied.

Some studies into the transmittivity of various optical materials, for example BK-7, silver-coated glass, etc., have been supported by the European Space Agency (ESA) [63, 64, 65]. These results could serve as a starting point for these investigations, but the specific radiation environment of nuclear reactors, especially CANDU reactors during outages, must be considered. Furthermore, investigations into the transmission properties of various optical fibres have been completed [66, 67, 68], however, the same concerns as the studies completed with optical materials still exist. If a hollow-core optical fibre is selected for the transmitting fibre, an additional study will be required into its behaviour after being irradiated.

The lengths of optical fibres which are expected for this application will also require considerations for the gating parameters of the LIBS equipment. Dispersion would be expected in optical fibres of significant length and this may influence the optimal gate delay and gate widths; the optical fibres would need to be about 40 m in length. A rough estimation using Equation 6.1, shows that a 1064 nm pulse travelling along a 600 μm core diameter optical fibre from Thorlabs (FT600EMT) will experience approximately 7.8 ns of modal dispersion over a 40 m length. Furthermore, disper-

sion may change the ablation mechanism if it is significant enough, although this could be mitigated by selecting a laser system with a suitably short pulse duration. Finally, the length of the fibres would elicit the need to consider the transmission time of the laser to the interrogation site and the transmission time of the emitted light to the spectrometer.

$$\Delta\tau_{modal} = \frac{L(n_1 - n_2)}{c}\left(1 - \frac{\pi}{\frac{2\pi a}{\lambda}\sqrt{n_1^2 - n_2^2}}\right) \tag{6.1}$$

Where $\Delta\tau_{modal}$ is the temporal dispersion of the pulse, L is the length of the optical fibre, n_1 and n_2 are the refractive indices of the core and cladding, respectively, c is the speed of light, λ is the central wavelength being transmitted, and a is the radius of the optical fibre core.

6.3 Recommendations

Considering the above discussion and the results of this thesis a recommended system for continuing this experimentation would include a DP-LIBS system comprised of picosecond pulsed lasers, with the primary laser capable of delivering several tens to a hundred millijoules of energy per pulse. Several orientations of the secondary pulse should be experimented with as previous works have shown that the direction of the secondary pulse has an effect on the emission parameters [59]. For delivering the pulses to the sample, hollow core fibres should be used. The purpose being twofold: firstly, this will avoid the issue of dispersion along the

fibre, and, secondly, will help to eliminate transmission losses along the fibre.

A spectrometer with similar capabilities to the Princeton Instruments Isoplane SCT 320 should be employed. It would be ideal to use a spectrometer with a higher resolution to help with the distinction of H-α and D-α emission lines, however, such systems should be tested beforehand. Lower resolution systems should not be considered as the pixel spacing around the emission lines of interest may result in too much blending between the emission lines.

Finally, for the measurement environment, the experimentation presented in this research showed clearly that using He as a buffer gas resulted in the narrowest emission lines of the gases tested. Additionally, it was found that a vacuum environment allowed for the simultaneous observation of H-α and D-α emission lines. Therefore, it is recommended that a vacuum chamber capable of being back-filled with a buffer gas is used for further experimentation. In addition to back-filling capabilities, having a load-lock system will limit the amount of atmospheric contamination when swapping samples.

Using a system with these capabilities will enhance the ability to identify the presence of D in Zr-2.5$\%$Nb and should also allow for measurement of the concentration D. This will allow for the creation of a calibration curve, testing of required LIBS site sizes, and D signal variability in individual samples. These steps will further the development of a LIBS-based inspection tool for use in nuclear reactors.

Appendices

A DEUTERIDED ZIRCONIUM FOIL

A brief experiment was conducted using the ion implantation equipment available at the University of Toronto. Zirconium foil samples (Alfa Aesar, 25 μm thick, 99.8% purity (metal basis)) with high surface concentrations of deuterium were produced by bombardment with a deuterium ion (D+) beam. One sample was produced with a 1010 eV/D+ beam, while the other was produced with a 750 eV/D+ The fluence at the surface of the sample was found to be 5.68×10^{23} m^{-2}.

Unfortunately, the system used to create these samples has not been calibrated for use with Zr foil as it typically is used to produce tungsten samples. Therefore the exact deuterium concentration implanted was unknown. However, based on the implantation parameters, the surface concentration was expected to be between 1-5% atomic, with an appreciable percentage extending at least 1 μm into the foil [69].

The intention of these samples was to create samples in which the D-α emission line would be abundantly clear while still seeing emission from the nearby Zr lines. This would give an idea of the signal that could be expected by hitting ZrD in a LIBS measurement. No clear D signal could be seen from this sample and at this time the

reason is not known. Future studies should revisit similar samples as a benchmark for heavily deuterided Zr.

B UNIDENTIFIED EMISSION LINE

A persistent emission line was seen at 650.9 nm in LIBS measurements conducted on Zr and Zr-2.5%Nb samples in air environments. This peak cannot be attributed to any known contaminant species or atmospheric element in the measurement environment based on NIST's database [58]. This peak was seen at atmospheric pressures and vacuum pressures. Figure B.1 shows the feature in an atmospheric environment during nanosecond LIBS, Figure B.2 shows the feature in an atmospheric environment during picosecond LIBS, and Figure B.3 shows the feature in a vacuum environment during picosecond LIBS.

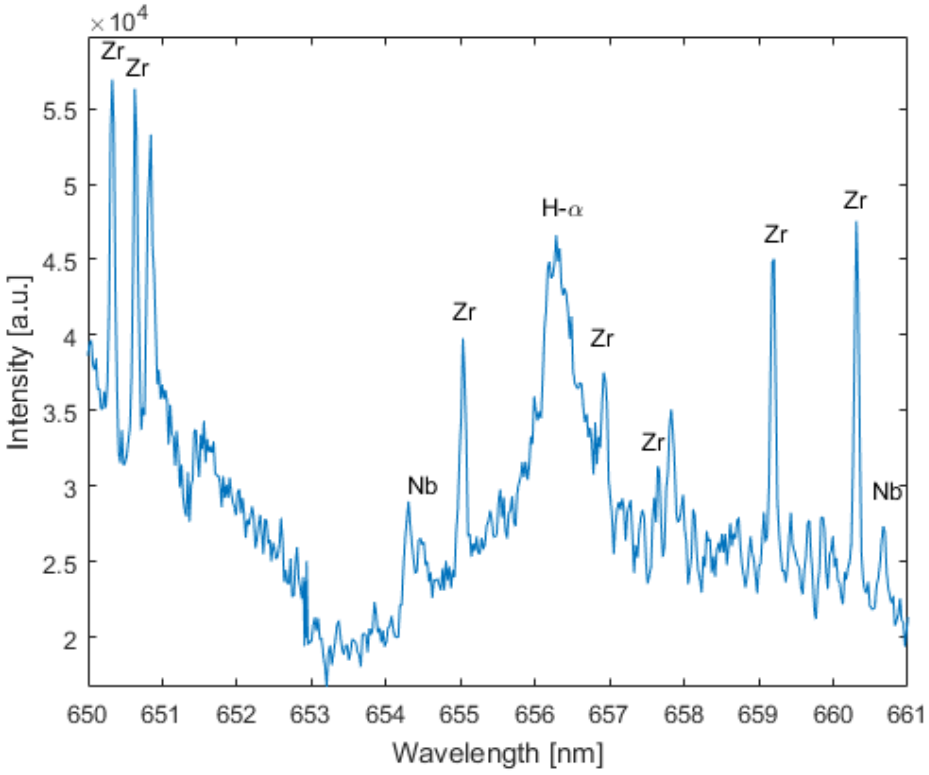

Figure B.1: Spectrum of an artificially deuterided sample of Zr-2.5%Nb with 90 ppm D in air. Note the unknown emission line at 650.9 nm.

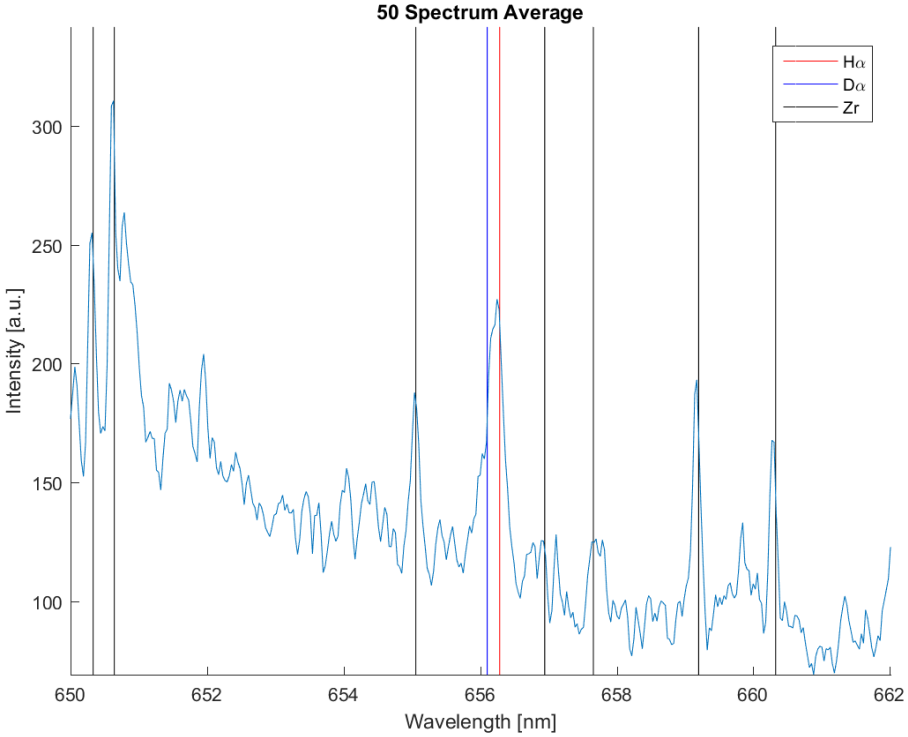

Figure B.2: Emission from H-α in an artificially deuterided Zr foil in air. Note the unidentified emission line at 650.9 nm.

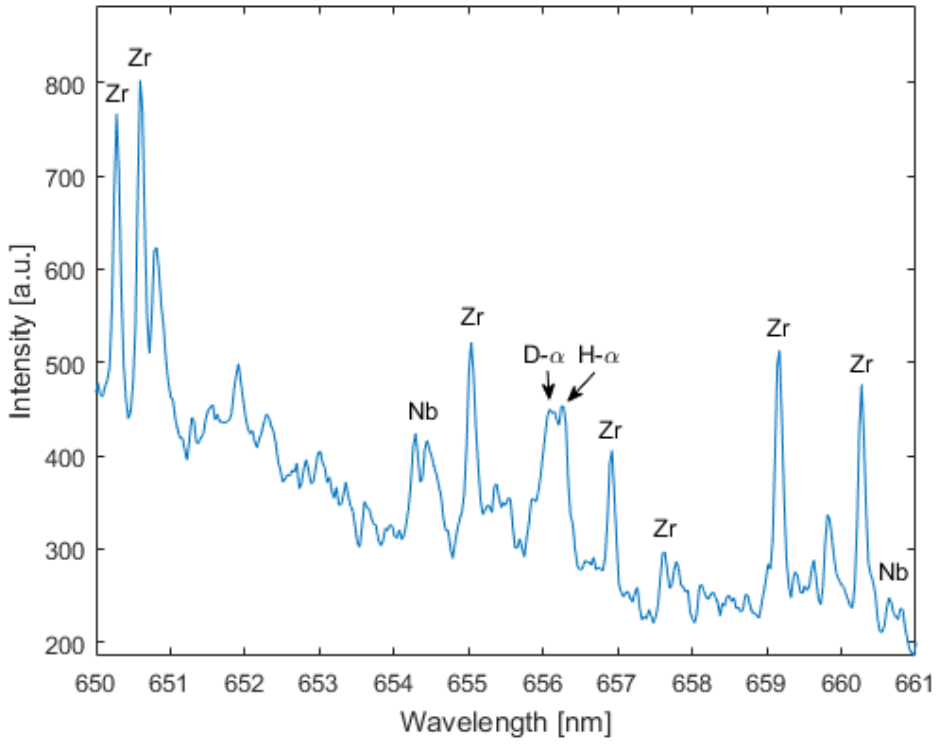

Figure B.3: Part of the emission spectrum from the average of 50 spectra from and artificially deuterided sample of Zr-2.5%Nb. Note the unidentified emission line at 650.9 nm.

Unfortunately, the source of this emission line was not known. Interestingly, it was not present in measurements made in He and Ar. This suggests that the peak is arising from some interaction of the plasma with air. Figure B.4 and Figure B.5 show the LIBS spectra measured in Ar and He, respectively, at atmospheric pressure during nanosecond LIBS.

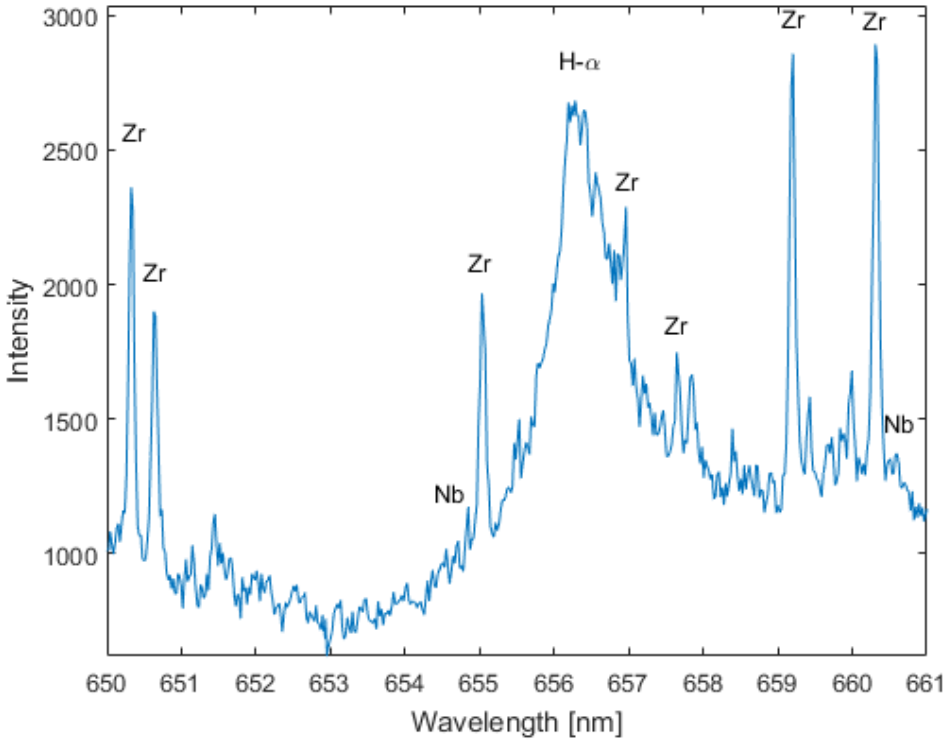

Figure B.4: Emission from H-α in an artificially deuterided sample of Zr-2.5%Nb with 90 ppm D in an Ar flow environment at atmospheric pressure. Note the lack of an emission line at 650.9 nm.

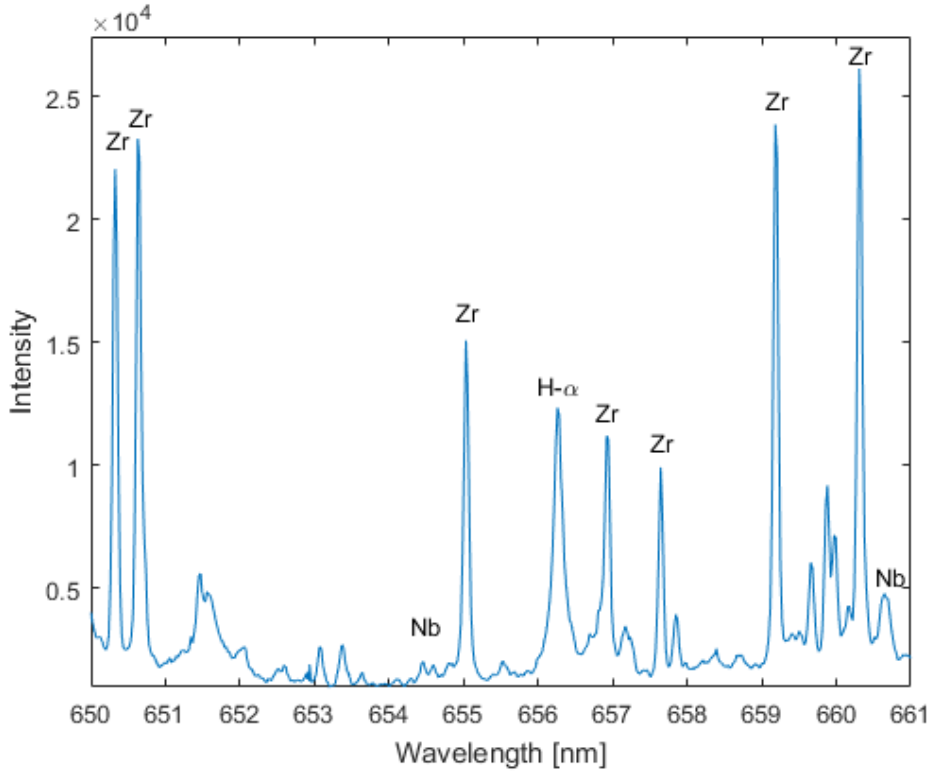

Figure B.5: Emission from H-α in an artificially deuterided sample of Zr-2.5%Nb with 90 ppm D in a He flow environment at atmospheric pressure. Note the lack of an emission line at 650.9 nm.

Further study should be conducted into the origin of this emission line. It is possible that the peak is the result of an interaction between Zr and some atmospheric element, such as Nitrogen (N) or Oxygen (O), however, these molecular emission profiles are not readily available.

REFERENCES

[1] H. G. Rickover, L. D. Geiger, and B. Lustman, "History of the development of zirconium alloys for use in nuclear reactors," Energy Research and Development Administration, Washington, D.C. (USA). Div. of Naval Reactors, Tech. Rep. TID-26740, Mar. 1975. DOI: 10.2172/4240391.

[2] R. Krishnan and M. K. Asundi, "Zirconium alloys in nuclear technology," *Proceedings of the Indian Academy of Sciences Section C: Engineering Sciences*, vol. 4, no. 1, pp. 41–56, Apr. 1981, ISSN: 0973-7677. DOI: 10.1007/BF02843474.

[3] G. J. Field, J. T. Dunn, and B. A. Cheadle, "Analysis of the pressure tube failure at Pickering NGS 'A' unit 2," Atomic Energy of Canada Ltd., Tech. Rep. AECL–8335, 1984.

[4] W. J. Garland, Ed., *The Essential CANDU, A Textbook on the CANDU Nuclear Power Plant Technology*. University Network of Excellence in Nuclear Engineering (UNENE), ISBN: 0-9730040.

[5] D. O. Northwood and U. Kosasih, "Hydrides and delayed hydrogen cracking in zirconium and its alloys," *International Metals Reviews*, vol. 28, no. 1, pp. 92–121, Jan. 1983, ISSN: 0308-4590. DOI: 10.1179/imtr.1983.28.1.92.

[6] G. A. McRae, C. E. Coleman, and B. W. Leitch, "The first step for delayed hydride cracking in zirconium alloys," *Journal of Nuclear Materials*, vol. 396, no. 1, pp. 130–143, Jan. 2010, ISSN: 0022-3115. DOI: 10.1016/j.jnucmat.2009.08.019.

[7] G. A Bickel, L. W Green, M. W. D James, T. G Lamarche, P. K Leeson, and H Michel, "The determination of hydrogen and deuterium in Zr–2.5Nb material by hot vacuum extraction mass spectrometry," *Journal of Nuclear Materials*, vol. 306, no. 1, pp. 21–29, Nov. 2002, ISSN: 0022-3115. DOI: 10.1016/S0022-3115(02)01230-8.

[8] L Popescu, N Van Den Brekel, A Wallace, L Micuda, and B. Power, "Tss tool measurements in candu reactors–results and issues," in *Seventh CNS International Conference on CANDU Maintenance, Toronto Canada*, 2005.

[9] A Wallace, K Tashiro, A Hamilton, T Gough, S Burany, K Kim, and M Park, "Deployment of the terminal solid solubility (TSS) tool for hydrogen equivalent concentration measurement in Wolsong Unit 2," 2011.

[10] M. Rubel, P. Wienhold, and D. Hildebrandt, "Fuel accumulation in co-deposited layers on plasma facing components," *Journal of Nuclear Materials*, 14th Int. Conf. on Plasma-Surface Interactions in Controlled Fusion D evices, vol. 290-293, pp. 473–477, Mar. 2001, ISSN: 0022-3115. DOI: 10.1016/S0022-3115(00)00583-3.

[11] J. Byskov-Nielsen, J.-M. Savolainen, M. S. Christensen, and P. Balling, "Ultrashort pulse laser ablation of metals: Threshold fluence, incubation coefficient and ablation rates," *Applied Physics A*, vol. 101, no. 1, pp. 97–101, Oct. 2010, ISSN: 1432-0630. DOI: 10.1007/s00339-010-5766-1.

[12] J. J. Chang and B. E. Warner, "Laser-plasma interaction during visible-laser ablation of methods," *Applied Physics Letters*, vol. 69, no. 4, pp. 473–475, Jul. 1996, Publisher: American Institute of Physics, ISSN: 0003-6951. DOI: 10.1063/1.118144.

[13] D. W. Hahn and N. Omenetto, "Laser-Induced Breakdown Spectroscopy (LIBS), Part I: Review of Basic Diagnostics and Plasma–Particle Interactions: Still-Challenging Issues Within the Analytical Plasma Community," *Applied Spectroscopy*, vol. 64, no. 12, 335A–366A, Dec. 2010, Publisher: Society for Applied Spectroscopy.

[14] D. A. Cremers and L. J. Radziemski, *Handbook of Laser-Induced Breakdown Spectroscopy, 2nd Edition | Wiley*, Mar. 2013.

[15] R. Noll, "Laser-Induced Breakdown Spectroscopy," in *Laser-Induced Breakdown Spectroscopy: Fundamentals and Applications*, R. Noll, Ed., Berlin, Heidelberg: Springer, 2012, pp. 7–15, ISBN: 978-3-642-20668-9. DOI: 10.1007/978-3-642-20668-9_2.

[16] S. Musazzi and U. Perini, "Laser-induced breakdown spectroscopy," *Springer Series in Optical Sciences*, vol. 182, 2014.

[17] E. Tognoni, G. Cristoforetti, S. Legnaioli, and V. Palleschi, "Calibration-Free Laser-Induced Breakdown Spectroscopy: State of the art," *Spectrochimica Acta Part B: Atomic Spectroscopy*, vol. 65, no. 1, pp. 1–14, Jan. 2010, ISSN: 0584-8547. DOI: 10.1016/j.sab.2009.11.006.

[18] M. Ramli, K.-i. Fukumoto, H. Niki, S. N. Abdulmadjid, N. Idris, T. Maruyama, K. Kagawa, M. O. Tjia, M. Pardede, K. H. Kurniawan, R. Hedwig, Z. S. Lie, T. J. Lie, and D. P. Kurniawan, "Quantitative hydrogen analysis of zircaloy-4 in laser-induced breakdown spectroscopy with ambient helium gas," *Applied Optics*, vol. 46, no. 34, pp. 8298–8304, Dec. 2007, ISSN: 2155-3165. DOI: 10.1364/AO.46.008298.

[19] R. Hedwig, Z. S. Lie, K. H. Kurniawan, A. N. Chumakov, K. Kagawa, and M. O. Tjia, "Toward quantitative deuterium analysis with laser-induced breakdown spectroscopy using atmospheric-pressure helium gas," *Journal of Applied Physics*, vol. 107, no. 2, p. 023 301, Jan. 2010, ISSN: 0021-8979. DOI: 10.1063/1.3282801.

[20] M. Pardede, T. J. Lie, J. Iqbal, M. Bilal, R. Hedwig, M. Ramli, A. Khumaeni, W. S. Budi, N. Idris, S. N. Abdulmadjid, A. M. Marpaung, I. Karnadi, I. Tanra, Z. S. Lie, H. Suyanto, D. P. Kurniawan, K. H. Kurniawan, K. Kagawa, and M. O. Tjia, "H–D Analysis Employing Energy Transfer from Metastable Excited-State He in Double-Pulse LIBS with Low-Pressure He Gas," *Analytical Chemistry*, vol. 91, no. 2, pp. 1571–1577, Jan. 2019, ISSN: 0003-2700, 1520-6882. DOI: 10.1021/acs.analchem.8b04834.

[21] S. Almaviva, L. Caneve, F. Colao, and G. Maddaluno, "Deuterium detection and quantification by laser-induced breakdown spectroscopy and calibration-free analysis in ITER relevant samples," *Fusion Engineering and Design*, SI:SOFT-30, vol. 146, pp. 2087–2091, Sep. 2019, ISSN: 0920-3796. DOI: 10.1016/j.fusengdes.2019.03.109.

[22] S. Almaviva, L. Caneve, F. Colao, G. Maddaluno, N. Krawczyk, A. Czarnecka, P. Gasior, M. Kubkowska, and M. Lepek, "Measurements of deuterium retention and surface elemental composition with double pulse laser induced breakdown spectroscopy," *Physica Scripta*, vol. T167, p. 014 043, Feb. 2016, ISSN: 0031-8949, 1402-4896. DOI: 10.1088/0031-8949/T167/1/014043.

[23] C. E. Ells, "Hydride precipitates in zirconium alloys (A review)," *Journal of Nuclear Materials*, vol. 28, no. 2, pp. 129–151, 1968.

[24] S. Y. Lim, S. Kim, and G.-G. Lee, "Hydride precipitation behavior with hydrogen concentration and homogenization temperature in zr-2.5% nb pressure tube material," *Korean Journal of Metals and Materials*, vol. 57, no. 4, pp. 203–213, 2019.

[25] C. E. Coleman and D. Hardie, "The hydrogen embrittlement of α-zirconium—A review," *Journal of the Less Common Metals*, vol. 11, no. 3, pp. 168–185, Sep. 1966, ISSN: 0022-5088. DOI: 10.1016/0022-5088(66)90003-8.

[26] L. A. Simpson and C. D. Cann, "Fracture toughness of zirconium hydride and its influence on the crack resistance of zirconium alloys," *Journal of Nuclear Materials*, vol. 87, no. 2, pp. 303–316, Dec. 1979, ISSN: 0022-3115. DOI: 10.1016/0022-3115(79)90567-1.

[27] S Yamanaka, K Yoshioka, M Uno, M Katsura, H Anada, T Matsuda, and S Kobayashi, "Thermal and mechanical properties of zirconium hydride," *Journal of Alloys and Compounds*, vol. 293-295, pp. 23–29, Dec. 1999, ISSN: 0925-8388. DOI: 10.1016/S0925-8388(99)00389-8.

[28] A. Botto, B. Campanella, S. Legnaioli, M. Lezzerini, G. Lorenzetti, S. Pagnotta, F. Poggialini, and V. Palleschi, "Applications of laser-induced breakdown spectroscopy in cultural heritage and archaeology: A critical review," *Journal of Analytical Atomic Spectrometry*, vol. 34, no. 1, pp. 81–103, 2019, Publisher: Royal Society of Chemistry. DOI: 10.1039/C8JA00319J.

[29] J. L. Gottfried, F. C. De Lucia, C. A. Munson, and A. W. Miziolek, "Laser-induced breakdown spectroscopy for detection of explosives residues: A review of recent advances, challenges, and future prospects," *Analytical and Bioanalytical Chemistry*, vol. 395, no. 2, pp. 283–300, Sep. 2009, ISSN: 1618-2650. DOI: 10.1007/s00216-009-2802-0.

[30] S. J. Rehse, J. Diedrich, and S. Palchaudhuri, "Identification and discrimination of Pseudomonas aeruginosa bacteria grown in blood and bile by laser-induced breakdown spectroscopy," *Spectrochimica Acta Part B: Atomic Spectroscopy*, vol. 62, no. 10, pp. 1169–1176, Oct. 2007, ISSN: 0584-8547. DOI: 10.1016/j.sab.2007.07.008.

[31] R. C. Wiens, S. Maurice, B. Barraclough, M. Saccoccio, W. C. Barkley, J. F. Bell, S. Bender, J. Bernardin, D. Blaney, J. Blank, *et al.*, "The chemcam instrument suite on the mars science laboratory (msl) rover: Body unit and combined system tests," *Space science reviews*, vol. 170, no. 1-4, pp. 167–227, 2012.

[32] K. Song, Y.-I. Lee, and J. Sneddon, "Applications of Laser-Induced Breakdown Spectrometry," *Applied Spectroscopy Reviews*, vol. 32, no. 3, pp. 183–235, Aug. 1997, ISSN: 0570-4928. DOI: 10.1080/05704929708003314.

[33] C. A. Smith, M. A. Martinez, D. K. Veirs, and D. A. Cremers, "Pu-239/pu-240 isotope ratios determined using high resolution emission spectroscopy in a laser-induced plasma," *Spectrochimica Acta Part B: Atomic Spectroscopy*, vol. 57, no. 5, pp. 929–937, 2002.

[34] G Maddaluno, S Almaviva, L Caneve, F Colao, V Lazic, L Laguardia, P Gasior, M Kubkowska, *et al.*, "Detection by libs of the deuterium retained in the ftu toroidal limiter," *Nuclear Materials and Energy*, vol. 18, pp. 208–211, 2019.

[35] S Almaviva, L Caneve, F Colao, and G Maddaluno, "Fusion related research with laser-induced-breakdown-spectroscopy on metallic samples at the ENEA-Frascati laboratory.," *Physica Scripta*, vol. 91, no. 4, p. 044 003, Apr. 2016, ISSN: 0031-8949, 1402-4896. DOI: 10.1088/0031-8949/91/4/044003.

[36] F Colao, S Almaviva, L Caneve, G Maddaluno, T Fornal, P Gasior, M Kubkowska, and M Rosinski, "Libs experiments for quantitative detection of retained fuel," *Nuclear Materials and Energy*, vol. 12, pp. 133–138, 2017.

[37] P. Paris, J. Butikova, M Laan, A Hakola, I Jogi, J Likonen, E. Grigore, and C. Ruset, "Comparison of libs results on iter-relevant samples obtained by nanosecond and picosecond lasers," *Nuclear Materials and Energy*, vol. 18, pp. 1–5, 2019.

[38] L. Guo, Z. Zhu, J. Li, Y Tang, S. Tang, Z. Hao, X. Li, Y. Lu, and X. Zeng, "Determination of boron with molecular emission using laser-induced breakdown spectroscopy combined with laser-induced radical fluorescence," *Optics express*, vol. 26, no. 3, pp. 2634–2642, 2018.

[39] F. L. Palmieri, R. I. Ledesma, J. G. Dennie, T. J. Kramer, Y. Lin, J. W. Hopkins, C. J. Wohl, and J. W. Connell, "Optimized surface treatment of aerospace composites using a picosecond laser," *Composites Part B: Engineering*, vol. 175, p. 107 155, Oct. 2019, ISSN: 13598368. DOI: 10.1016/j.compositesb.2019.107155.

[40] *Isoplane® SCT 320 User's Manual*, version 2, Princeton Instruments, Aug. 18, 2014, 90 pp.

[41] *Pi-max® 4 Camera System*, version 10, Princeton Instruments, Mar. 19, 2019, 318 pp.

[42] W. Pietsch, A. Petit, and A. Briand, "Isotope ratio determination of uranium by optical emission spectroscopy on a laser-produced plasma - basic investigations and analytical results," *Spectrochimica Acta Part B: Atomic Spectroscopy*, vol. 53, no. 5, pp. 751–761, May 1998, ISSN: 0584-8547. DOI: 10.1016/S0584-8547(97)00123-7.

[43] Z. L. Pan, I. G. Ritchie, and M. P. Puls, "The terminal solid solubility of hydrogen and deuterium in Zr-2.5Nb alloys," *Journal of Nuclear Materials*, vol. 228, no. 2, pp. 227–237, Mar. 1996, ISSN: 0022-3115. DOI: 10.1016/S0022-3115(95)00217-0.

[44] B. N. Chichkov, C. Momma, S. Nolte, F. Von Alvensleben, and A. Tünnermann, "Femtosecond, picosecond and nanosecond laser ablation of solids," *Applied physics A*, vol. 63, no. 2, pp. 109–115, 1996.

[45] S. I. Anisimov and B. Rethfeld, "Theory of ultrashort laser pulse interaction with a metal," in *Nonresonant Laser-Matter Interaction (NLMI-9)*, vol. 3093, International Society for Optics and Photonics, Apr. 1997, pp. 192–203. DOI: 10.1117/12.271674.

[46] S. Nolte, C. Momma, H. Jacobs, A. Tünnermann, B. N. Chichkov, B. Wellegehausen, and H. Welling, "Ablation of metals by ultrashort laser pulses," *JOSA B*, vol. 14, no. 10, pp. 2716–2722, Oct. 1997, Publisher: Optical Society of America, ISSN: 1520-8540. DOI: 10.1364/JOSAB.14.002716.

[47] T. Itina, *Laser Ablation: From Fundamentals to Applications*. BoD – Books on Demand, Dec. 2017, Google-Books-ID: lBCQDwAAQBAJ, ISBN: 978-953-51-3699-6.

[48] W. J. Keller, N. Shen, A. M. Rubenchik, S. Ly, R. Negres, R. N. Raman, J.-H. Yoo, G. Guss, J. S. Stolken, M. J. Matthews, *et al.*, "Physics of picosecond pulse laser ablation," *Journal of Applied Physics*, vol. 125, no. 8, p. 085 103, 2019.

[49] F. Vidal, T. W. Johnston, S. Laville, O. Barthélemy, M. Chaker, B. Le Drogoff, J. Margot, and M. Sabsabi, "Critical-Point Phase Separation in Laser Ablation of Conductors," *Physical Review Letters*, vol. 86, no. 12, pp. 2573–2576, Mar. 2001, Publisher: American Physical Society. DOI: 10.1103/PhysRevLett.86.2573.

[50] N. Bulgakova and A. Bulgakov, "Pulsed laser ablation of solids: Transition from normal vaporization to phase explosion," *Applied Physics A*, vol. 73, no. 2, pp. 199–208, Aug. 2001, ISSN: 1432-0630. DOI: 10.1007/s003390000686.

[51] K.-H. Leitz, B. Redlingshöfer, Y. Reg, A. Otto, and M. Schmidt, "Metal ablation with short and ultrashort laser pulses," *Physics Procedia*, vol. 12, pp. 230–238, 2011.

[52] T. V Kononenko, S. V Garnov, S. M Klimentov, V. I Konov, E. N Loubnin, F Dausinger, A Raiber, and C Taut, "Laser ablation of metals and ceramics in picosecond–nanosecond pulsewidth in the presence of different ambient atmospheres," *Applied Surface Science*, vol. 109-110, pp. 48–51, Feb. 1997, ISSN: 0169-4332. DOI: 10.1016/S0169-4332(96)00905-1.

[53] S. H. Kim, I.-B. Sohn, and S. Jeong, "Ablation characteristics of aluminum oxide and nitride ceramics during femtosecond laser micromachining," *Applied Surface Science*, vol. 255, no. 24, pp. 9717–9720, Sep. 2009, ISSN: 01694332. DOI: 10.1016/j.apsusc.2009.04.058.

[54] Y. Liu, Y. Brelet, Z. He, L. Yu, S. Mitryukovskiy, A. Houard, B. Forestier, A. Couairon, and A. Mysyrowicz, "Ciliary White Light: Optical Aspect of Ultrashort Laser Ablation on Transparent Dielectrics," *Physical Review Letters*, vol. 110, no. 9, p. 097 601, Mar. 2013, Publisher: American Physical Society. DOI: 10.1103/PhysRevLett.110.097601.

[55] H. Mustafa, R. Pohl, T. C. Bor, B. Pathiraj, D. T. A. Matthews, and G. R. B. E. Römer, "Picosecond-pulsed laser ablation of zinc: Crater morphology and comparison of methods to determine ablation threshold," *Optics Express*, vol. 26, no. 14, pp. 18 664–18 683, Jul. 2018, Publisher: Optical Society of America, ISSN: 1094-4087. DOI: 10.1364/OE.26.018664.

[56] D Kazimer, P Zulow, A Kratt, S Berube, A Hamilton, and K. Maynard, "Bruce power circumferential wet scrape tool system," 2011.

[57] C. Liu, L. Gutkin, and D. Scarth, "Quantitative Characterization of Hydride Spacing for Cohesive-Zone Modelling of Fracture Toughness in Zr-2.5Nb Pressure Tubes," American Society of Mechanical Engineers Digital Collection, Dec. 2016. DOI: 10.1115/PVP2016-63073.

[58] J. E. Sansonetti and W. C. Martin, "Handbook of Basic Atomic Spectroscopic Data," *Journal of Physical and Chemical Reference Data*, vol. 34, no. 4,

pp. 1559–2259, Sep. 2005, Publisher: American Institute of Physics, ISSN: 0047-2689. DOI: 10.1063/1.1800011.

[59] Y. Li, D. Tian, Y. Ding, G. Yang, K. Liu, C. Wang, and X. Han, "A review of laser-induced breakdown spectroscopy signal enhancement," *Applied Spectroscopy Reviews*, vol. 53, no. 1, pp. 1–35, 2018.

[60] A. S. Eppler, D. A. Cremers, D. D. Hickmott, M. J. Ferris, and A. C. Koskelo, "Matrix effects in the detection of pb and ba in soils using laser-induced breakdown spectroscopy," *Applied Spectroscopy*, vol. 50, no. 9, pp. 1175–1181, 1996.

[61] R. A. Multari, D. A. Cremers, A. Nelson, Z. Karimi, S. Young, C. Fisher, and R. Duncan, "The use of laser-based diagnostics for the rapid identification of infectious agents in human blood," *Journal of applied microbiology*, vol. 126, no. 5, pp. 1606–1617, 2019.

[62] A. A. Bol'shakov, X. Mao, J. J. González, and R. E. Russo, "Laser ablation molecular isotopic spectrometry (lamis): Current state of the art," *Journal of Analytical Atomic Spectrometry*, vol. 31, no. 1, pp. 119–134, 2016.

[63] M. Fruit, A. I. Gusarov, D. B. Doyle, and G. J. Ulbrich, "Radiation impact on spaceborne optics: The dose coefficients approach," in *Photonics for Space and Radiation Environments*, vol. 3872, International Society for Optics and Photonics, Dec. 1999, pp. 60–71. DOI: 10.1117/12.373286.

[64] D. B. Doyle, T. M. Dewandre, D. Claessens, E. D. Cock, L. Vautmans, O. Dupont, and A. I. Gusarov, "Radiation qualification and testing of a large number of optical glasses used in the ESA Fluid Science Laboratory onboard the Columbus Orbital Facility of the International Space Station," in *Photonics for Space Environments VIII*, vol. 4823, International Society for Optics and Photonics, Nov. 2002, pp. 124–131. DOI: 10.1117/12.452227.

[65] A. Gusarov, D. Doyle, L. Glebov, and F. Berghmans, "Comparison of radiation-induced transmission degradation of borosilicate crown optical glass from four different manufacturers," in *Photonics for Space Environments X*, vol. 5897, International Society for Optics and Photonics, Aug. 2005, p. 58970I. DOI: 10.1117/12.619199.

[66] D. Sporea, A. Sporea, and C. Oproiu, "Comparative study on the degradation of UV optical fibers subjected to electron beam and gamma ray irradiation,"

Optical Fiber Technology, vol. 19, no. 6, Part A, pp. 652–657, Dec. 2013, ISSN: 1068-5200. DOI: 10.1016/j.yofte.2013.10.005.

[67] *LDEF Materials Results for Spacecraft Applications*. National Aeronautics, Space Administration, Office of Management, Scientific, and Technical Information Program, 1994, Google-Books-ID: ZKgfAQAAIAAJ.

[68] E. J. Friebele, M. E. Gingerich, and D. L. Griscom, "Survivability of optical fibers in space," in *Optical Materials Reliability and Testing: Benign and Adverse Environments*, vol. 1791, International Society for Optics and Photonics, Feb. 1993, pp. 177–188. DOI: 10.1117/12.141177.

[69] A. A. Haasz and J. W. Davis, "Synergistic chemical erosion of graphite due to simultaneous bombardment by H+ and other low-Z ions using a dual-beam accelerator," *Nuclear Instruments and Methods in Physics Research Section B: Beam Interactions with Materials and Atoms*, vol. 83, no. 1, pp. 117–124, Oct. 1993, ISSN: 0168-583X. DOI: 10.1016/0168-583X(93)95915-R.